



**POLITECNICO
DI TORINO**

Dipartimento di Ingegneria
dell'Ambiente, del Territorio
e delle Infrastrutture

**UNIVERSIDAD
POLITÉCNICA DE MADRID**



ESCUELA TÉCNICA SUPERIOR
DE INGENIEROS DE MINAS Y ENERGÍA



Master degree in Environmental and Land Engineering

**An example of a 3D Discrete Fracture
Network Model in a Karst Aquifer
(Sierra de las Nieves, Betic Cordillera, Spain)**

Thesis supervisors:

De Maio Marina (POLITO)

Paredes Bartolome Carlos (UPM)

De la Vega Panizo Rogelio (UPM)

Candidate:

Jacopo Valeriano

July 2018

To Luisa

Acknowledgements/Ringraziamenti

(ENG) First of all I would like to thank my family, especially, my parents Anna and Giovanni, who have always supported me in all my decisions and have been by my side, accompanying and guiding me on this path undertaken for the past three years, which has led me to complete a master's degree in Environment and Land Engineering at The Politecnico di Torino.

I would especially like to thank Carlos Paredes Bartolome and Rogelio de la Vega Panizo of the Universidad Politecnica de Madrid, as they have followed me in this very long year, which has led me to the completion of the thesis work that will be presented in this document.

To the uncles, Massimo and grandmothers Annita and Checca who have filled me with preserved and amantean foods for moments of "famine" away from home.

To my life partner Irina who supported and endured me throughout the whole thesis process and finally, to all my friends. A special word of thanks goes to the "Marina", a house filled with exceptional people with whom I have shared a lot and I hope to continue doing so in the future.

Finalt, I would like to thank the Politecnico di Torino which has encouraged all the experiences abroad, including an Erasmus and thesis in Madrid and an internship in Barcelona, which have helped me to grow both at an educational and personal level.

Thank you all so much.

(IT) I primi ringraziamenti per questi ultimi tre anni che mi hanno portato al conseguimento della laurea magistrale in Ingegneria per l'Ambiente e il Territorio presso il Politecnico di Torino vanno alla mia famiglia, in particolare ai miei genitori Anna e Giovanni, che da sempre mi hanno appoggiato in tutte le mie decisioni e sono stati sempre al mio fianco accompagnandomi e guidandomi in questo percorso intrapreso.

Vorrei ringraziare in particolare Carlos Paredes Bartolome e Rogelio de la Vega Panizo dell'Universidad Politecnica de Madrid per come mi hanno seguito in questo lunghissimo anno che mi ha portato alla realizzazione del lavoro di tesi che verrà presentato in questo documento.

Agli zii, Massimo e alle nonne Annita e Checca che mi hanno riempito di conserve e cibi amanteani per i momenti di "carestia" lontano da casa.

Alla mia compagna di vita Irina che mi ha supportato e sopportato in tutto il processo della tesi ed infine a tutti gli amici, italiani e non. Un particolare pensiero alla "Marina", casa composta da persone eccezionali con le quali ho condiviso molto e spero di continuare a fare nel futuro.

Un ultimo ringraziamento va al Politecnico di Torino che ha incentivato tutte le esperienze all'estero, tra cui Erasmus e tesi a Madrid e tirocinio a Barcellona, che mi hanno fatto crescere sia a livello educativo che personale.

Grazie a tutti di cuore.

.

Index

Abstract	iv
1. Introduction	1
2. Study Area.....	4
2.1. Introduction	4
2.2. Delimitation of the Study Area	5
2.3. Weather	5
2.4. Orography.....	6
2.5. Geology	6
2.6. Vegetation	9
3. Data Used for the 3D Model Creation (Lineaments)	10
3.1. Tectonic Origin of Families	20
4. Statistical Analysis of the Lineaments	22
4.1 Introduction	22
4.2. Family 1.....	26
4.2.1. Generation model	27
4.2.2. Global fracture intensity P_{32}	27
4.2.3. Fracture orientation	28
4.2.4. Fracture size	28
4.2.5. Termination probability.....	29
4.3. Family 2.....	30
4.3.1. Generation model	31
4.3.2. Global fracture intensity P_{32}	31
4.3.3. Fracture orientation	31
4.3.4. Fracture size	32
4.3.5. Termination probability.....	32
4.4. Family 3.....	33
4.4.1. Generation model	34
4.4.2. Global fracture intensity P_{32}	34
4.4.3. Fracture orientation	35
4.4.4. Fracture size	35
4.4.5. Termination probability.....	36
4.5. Family 4.....	37
4.5.1. Generation model	38
4.5.2. Global fracture intensity P_{32}	39
4.5.3. Fracture orientation	39

4.5.4. Fracture size	40
4.5.5. Termination probability.....	40
4.6. Family 5.....	41
4.6.1. Generation model	42
4.6.2. Global fracture intensity P_{32}	42
4.6.3. Fracture orientation	42
4.6.4. Fracture size	43
4.6.5. Termination probability.....	43
4.7. Summary of the parameters to be included in the model.....	44
5. 3D Discrete Fracture Model Creation	45
5.1. Simplified Model.....	45
5.2. 3D Discrete Fracture Model.....	50
5.2.1. Volume	50
5.2.2. Family 1.....	52
5.2.3. Family 2.....	53
5.2.4. Family 3.....	54
5.2.5. Family 4.....	55
5.2.6. Family 5.....	56
5.2.7. Completed Fracture Model.....	57
6. Model Validation.....	58
6.1. P_{21}	59
6.2. Visual Comparison.....	60
6.2.1. Family 1.....	60
6.2.2. Family 2.....	61
6.2.3. Family 3.....	62
6.2.4. Family 4.....	63
6.2.5. Family 5.....	64
6.2.6. Total Fracture Model.....	65
6.3. Comparison Length Histograms.....	67
6.3.1. Family 1.....	67
6.3.2. Family 2.....	68
6.3.3. Family 3.....	69
6.3.4. Family 4.....	70
6.3.5. Family 5.....	71
6.2.6. All Families	72
6.4. Stereonet (stereographic projection) and Rose Diagram.....	73
6.4.1. Family 1.....	73

6.4.2. Family 2.....	74
6.4.3. Family 3.....	75
6.4.4. Family 4.....	76
6.4.5. Family 5.....	77
6.4.6. Total Simulated Fracture Model	78
7. Caves and springs for hydrogeological validation	80
8. Qualitative Analysis of Fracture Clusters	82
9. Pathway Analysis (3D Discrete Fracture Network Model)	85
10. Critical Stress Analysis	92
11. Conclusions	95
References	97

Abstract

The influence of geological structure on the endokarst and on the exokarst can be studied through the relationship between the discontinuities (faults, joints, fractures and foliations) and the speleological study of the underground caves. The present thesis, proposes a methodology that can be applied to all those geological areas where these types of formations are present.

The study area that has been taken into consideration is the karst of the Sierra de las Nieves park, in the province of Malaga (Spain), an example of high relief karst, the biggest in the south of the Iberian Peninsula. The main objective of this work is the implementation of a 3D Discrete Fracture Network Model, with the support of the FracMan software, which can allow to characterize, determine, and quantify the conditions that cause the field of paleoefforts and current efforts in the development of the karst.

Information of superficial discontinuities were used, which allowed the realization of the 3D Model through the analysis of statistical data about length, distribution and intensity, which was subsequently validated both at a statistical and hydrogeological level. Thanks to the results obtained, the knowledge of the karst system increases positively, considering that speleological research is a slow and expensive process. This will allow to improve the conceptual models that give a new approach to the treatment of diversity and the problem that emerges in the management of water and hydrogeological resources.

With regard to the environmental aspect, the karst systems, in particular the cavities and galleries networks that can host the endokarst and exokarst formations, forming biospeleological reserves, are a natural and cultural heritage for the society that must be preserved.

The proposed study addresses key aspects for the socio-economic development of countries that have to cope with necessities related to the management of water resources. This work aims to examine, according to the relationship between the spatial arrangement of the karst and the tectonic system, the spatial position of a certain number of water resources that can directly or indirectly influence the quality of life of the population. This indirect form of study translates into a better understanding of the karstic systems, known as very complex.

Keywords: Karst, Sierra de las Nieves, 3D Fracture Modelling, Discrete Fracture Networks

1. Introduction

This work deals with the structural composition of the carbonaceous aquifer of the Sierra de las Nieves (Malaga), which offers a spectacular example of a high relief karst that can undoubtedly be considered as a "natural karst laboratory".

Geomorphology is the discipline that studies and describes the forms of the earth's surface. In the case of the karstic massifs, there is a wide variety of characteristic morphologies, some typical of the surface relief (the exokarst) and others exclusive to the particular underground world of this type of terrain (the endokarst).

The karstic geomorphology of the Sierra de las Nieves is spectacular. The karstic landscape that can be seen on the surface, when walking on the ground, offers important contrasts from one area to another, for various reasons. First of all, being a high relief karst implies the existence of a very steep topography, with large differences in altitude and steep slopes. On the other hand, although the local stratigraphic series is mostly made up of carbonate rocks (limestones and dolomites), there are marked lithological, structural and mechanical differences in the different outcrops. Finally, there are also significant differences in the type and density of the vegetation and the development of the soil. These characteristics condition the final geoforms that are observed today and that have been forming from the remote past by interaction between atmospheric phenomena and the surface of the land.

A small but very significant part of the Sierra de las Nieves surface (around 5%) is made up of closed depressions, the most characteristic forms of the exotic landscape, together with the fields of limestone pavement. Dolines, uvalas and poljes affect the Llanos de la Nava and the high plateau of the Sierra around Torrecilla peak, the highest level of the park with 1919 meters above sea level.

In the high parts of the sierra and on the fractured rock and without vegetation there are the entries of many chasms, while in the flat areas, dolines are formed, sometimes filling with detrital sediments, whose thickness is very variable, being able to reach tens of meters. The study of these elements through geophysical techniques and surveys and their subsequent analysis, is of great interest for the knowledge of the climatic and environmental evolution of the sierra in the last millennia.

Sometimes dolines can be united, forming uvalas, or aligned along an elongated depression or old valley. Others may be captured by transforming into an open depression, with exoreic drainage.

This whole set of depressions fulfils its function, from the hydrogeological point of view, as a collector of precipitation into the karstic subsoil, concentrating on the endokarstic networks, where after overcoming the unsaturated area of the massif, they reach the water zones or permanently flooded, that is, saturated with water.

But not all the surface of the exokarst is equally permeable. There are also very little permeable areas, due to the structural condition of the rock, for example in areas close to large fractures in which a granular material has been generated, which offers very characteristic micro reliefs and generates sand. In sharp contrast there are also areas with significant soil and vegetation development, which cover the carbonate rock, making the perception of karstic forms subtler.

The Sierra de las Nieves is a real paradise for cavers. It is the most important karstic massif of the southern half of the Iberian Peninsula. In the last forty years, numerous karstic cavities have been located and explored: caves, of predominantly horizontal development and chasms, of

mainly vertical tendency. But what makes especially remarkable the Sierra de las Nieves is the presence of huge endokarstic networks, which form complex three-dimensional lattices and reach depths that exceed a thousand meters. These are the so-called super caves (super cuevas). Sima GESM, Sima del Aire or Sima Prestá are some of these exceptional cavities, in which gigantic vertical wells alternate, with narrow meanders of tortuous routes, and large horizontal galleries, testimonies of ancient water tables. Most likely, these large chasms are part of a common system, which drains the Sierra's somatic plateau (the so-called Torrecilla Block) towards the source of the Río Grande, where the birth of Zarzalones is located, submerged batifreatic cavity of more than 1500 meters long, the longest known so far in this environment.

The main source of water in the Sierra de las Nieve aquifer is rain and, to a much lesser extent, snow. The rain that reaches the surface of the land can infiltrate the soil or the epikarst or it can drain forming surface runoff. The water that infiltrates can return to the atmosphere due to evapotranspiration or it can start a downward movement (percolating) through the unsaturated zone of the aquifer and eventually it can reach the piezometric level and later exit to the outside through a spring (saturated zone). This process is called aquifer recharge and it is well known that in karst terrain, unlike detrital lands, the value of the load is high. As an average value it can be considered that 50% of the annual rainfall infiltrates as recharge, although this value depends on each karst system and also has a special variability.

Rainfall in the Sierra de las Nieves is estimated by statistical methods from the few rainfall stations available and using the digital elevation model as a secondary variable. This technique allows us to take advantage of the information provided by the topography since there is usually a positive correlation between altitude and rainfall, so that it normally rains more in areas that are at higher altitudes.

The network of karstic conduits is the element that introduces the greatest anisotropy and heterogeneity in the hydrogeological behaviour of the karst. However, speleological information is still very limited in relation to the dimensions of the system, although extremely valuable, and therefore, the idea that is proposed is to generate possible versions of reality, that is, complete the karst network by simulation and do this in the most rigorous way from the statistical point of view as well as hydrogeological and geomorphological. For this purpose, a system of alpine-type or high-relief karst channels has been chosen, and in particular the subterranean karst system of the Sierra de las Nieves.

The results of the research on hydrodynamics carried out in the late seventies by Pr. A. Mangin, later confirmed by hydrogeochemistry, hydrogeothermy and biospeleology, established a scheme or conceptual model of the structural constitution of the karst system in the following parts are distinguished (Figure 1.1):

- The non-karstic implivium, constituted by the impermeable basin whose surface runoff is drained by the karstic aquifer.
- The infiltration zone with two types of circulation: a rapid one through discontinuities or significant cavities, sometimes true vertical drains and, another, slow type of percolation and biphasic character through minor discontinuities. In addition, in the most superficial part of this zone is located the epikarstic aquifer, which constitutes a subsystem of reserves not negligible. This aquifer performs the functions of exchange or evapotranspiration because it constitutes a limit or boundary with the external environment.
- The saturated zone constituted by two types of structures: drains of very transmissive ducts and the adjoining systems, of great capacities forming the reserves of the system and located laterally.

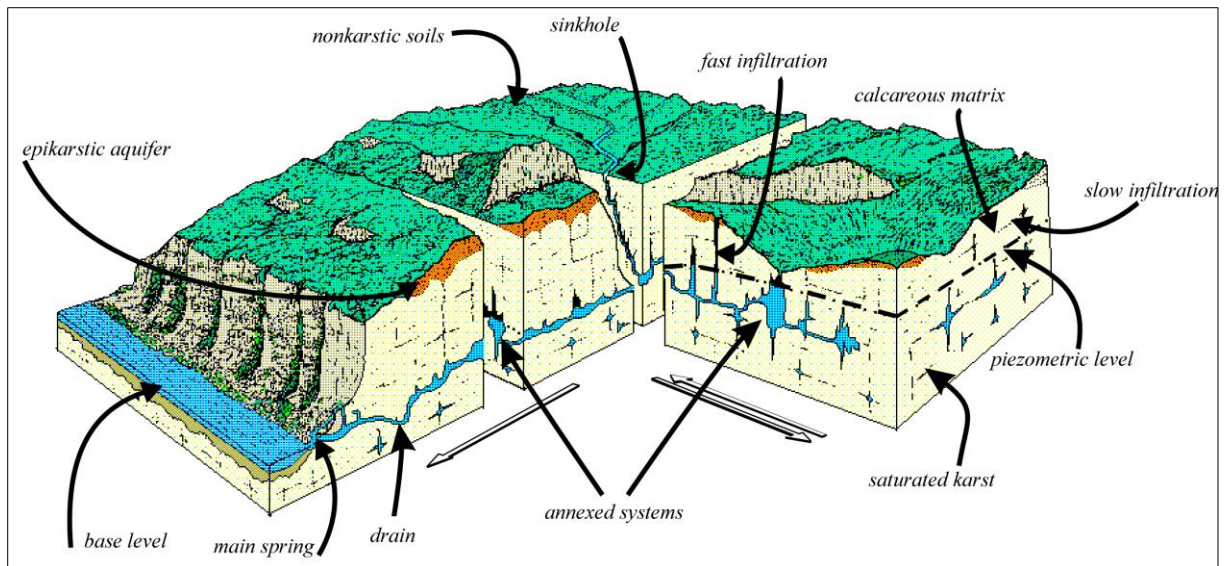


Figure 1. 1. Conceptual model of the structural approach of the karstic aquifer (according to Pr. A. Mangin).

The development of a greater or lesser organization in these structures is a function of the potential for karstification. This has been defined from the consideration of the conditions that preside over the genesis of a karst, which are specified in the following factors, among others: CO₂-water potential, geodynamic context, topographic characteristics, geological macrostructure. Undoubtedly it is a complex concept that requires a deepening that clarifies the interaction between the different factors and their definition.

This work has the need to establish a relationship between the complexity of its spatial distribution and its hydrodynamic behaviour. These ideas have their maximum expression in the functional hydrogeological approach of the karst that situates the nexus between conceptual and quantitative models in fractal modelling (Paredes, 1995, Paredes et al, 2002) and in the concepts of the theory of dynamic systems space temporary

The exhaustive analysis of the data on the properties of permeability and of the storage coefficient in calcareous regions reveals certain general rules about the evolution and behaviour of the karst, which are common to all systems (Mijatovic, 1996). Namely:

- The existence of a permeability due to a structural weakness marked in the rock that may or may not coincide with a discontinuity (fracture, fault, joint, foliation, etc.) of the rock mass, depending on the orientation of the rock with respect to the stress ellipsoid tectonic, essential condition of the beginning of all karstic erosion. According to the disposition and orientation of these planes of weakness, this erosion involves a karstification of extension that can be regional or local, depending on the tectonically privileged zones, among other variables.
- The decrease of karst erosion as a function of depth, the result of three factors such as the permeability of the planes of weakness available, the speed of the underground flow and the corrosive action of groundwater.
- The increase in the intensity of the karstification in the environment of the privileged drainage zones, the permeability of the planes of weakness, and the flow velocity are strongly correlated.
- The development of a vertical hydrodynamic zoning zone where the interfaces between the saturated and unsaturated zone are located approximately.

2. Study Area

2.1. Introduction

The present work is developed in the protected area of “Parque Natural Sierra de las Nieves”. It was declared a biosphere reserve by UNESCO in the 1995 and is one of the most important natural parks in Andalusia. The Sierra de las Nieves is located in the western central zone of the province of Malaga, to the east of the city of Ronda.



Figure 2.1. 1. Location of Sierra de las Nieves in the Iberian Peninsula.

The park occupies an area of 93,000 hectares, where eleven municipalities, with a population of close to 60,000 inhabitants, are located.

This area has important cultural and geological values although it is known, fundamentally, for its botanical wealth, the result of its privileged situation between the Mediterranean Sea and the Atlantic Ocean. The emblematic tree of the natural park is the pinsapo (*abies pinsapo*), a remnant of the extensive coniferous forests that existed in this area during the cold periods of the quaternary.

2.4. Orography

The orography is very rugged, with average altitudes of 1100 meters. Sierra de las Nieves is the highest massif of the study area, with peaks such as Alcazaba (1712 m), Enamorados (1789 m) and Torrecilla (1919m). The last peak is the highest point of the province of Malaga. The deepest gap in the south of the Iberian Peninsula is also located in this mountain range, the G.E.S.M. (Underground Exploration Group of Malaga), with -1.101 meters explored so far (Sociedad Excursionista de Málaga, 1990).

2.5. Geology

The geological study area is located in the western area of the Betic Cordillera. (Figure 2.5.1)

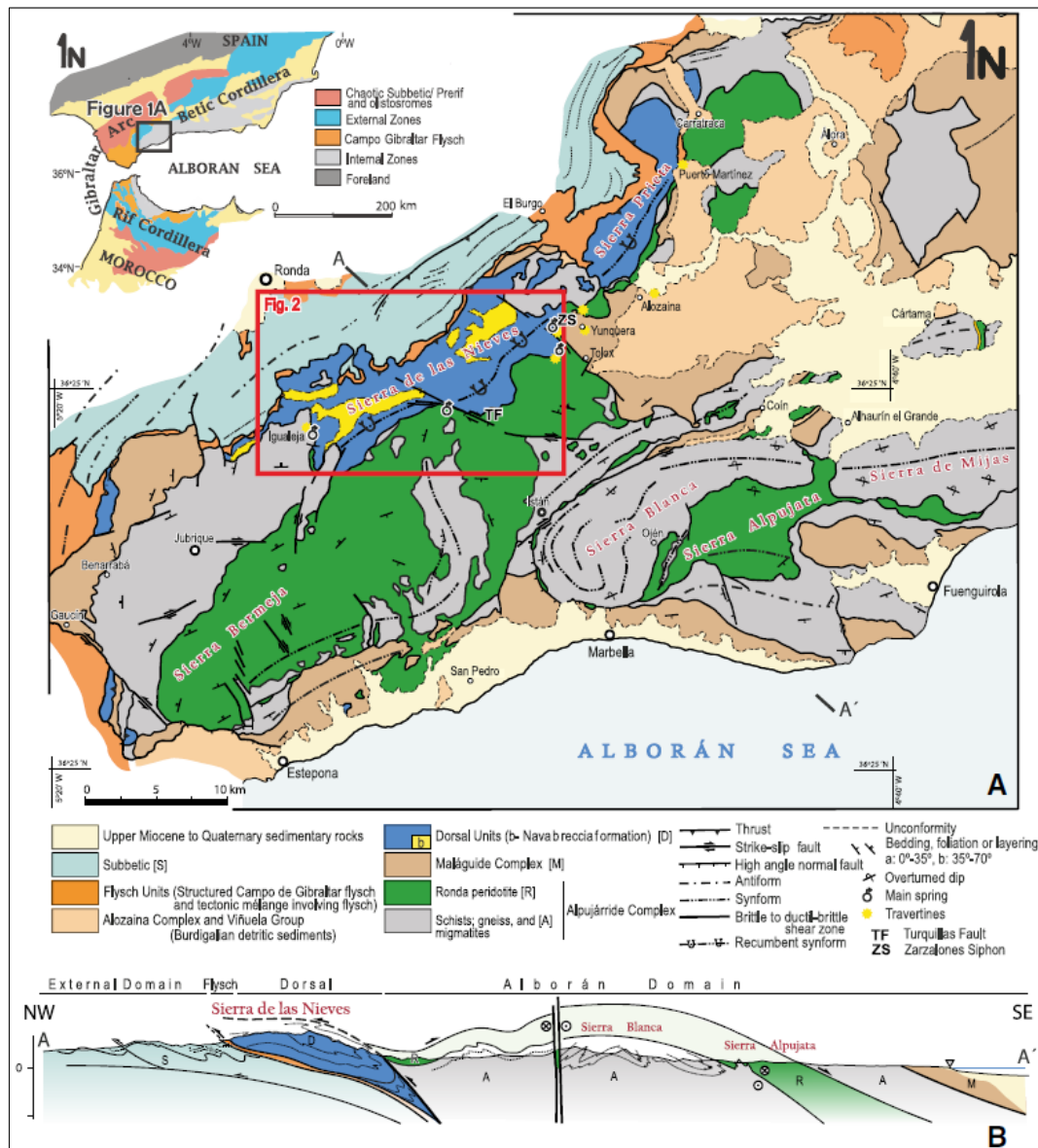


Figure 2.5. 1. Geological map and cross-section of the western part of the Betic Cordillera showing the location and the tectonic structure of the Sierra de las Nieves. (A. Pedrera et al., 2015)

In the Betic Cordillera, four main domains can be distinguished (Figure 2.5.2):

- External Zone
- Internal Zone
- Campo de Gibraltar Complex
- Neogenic basins or post orogenic materials.

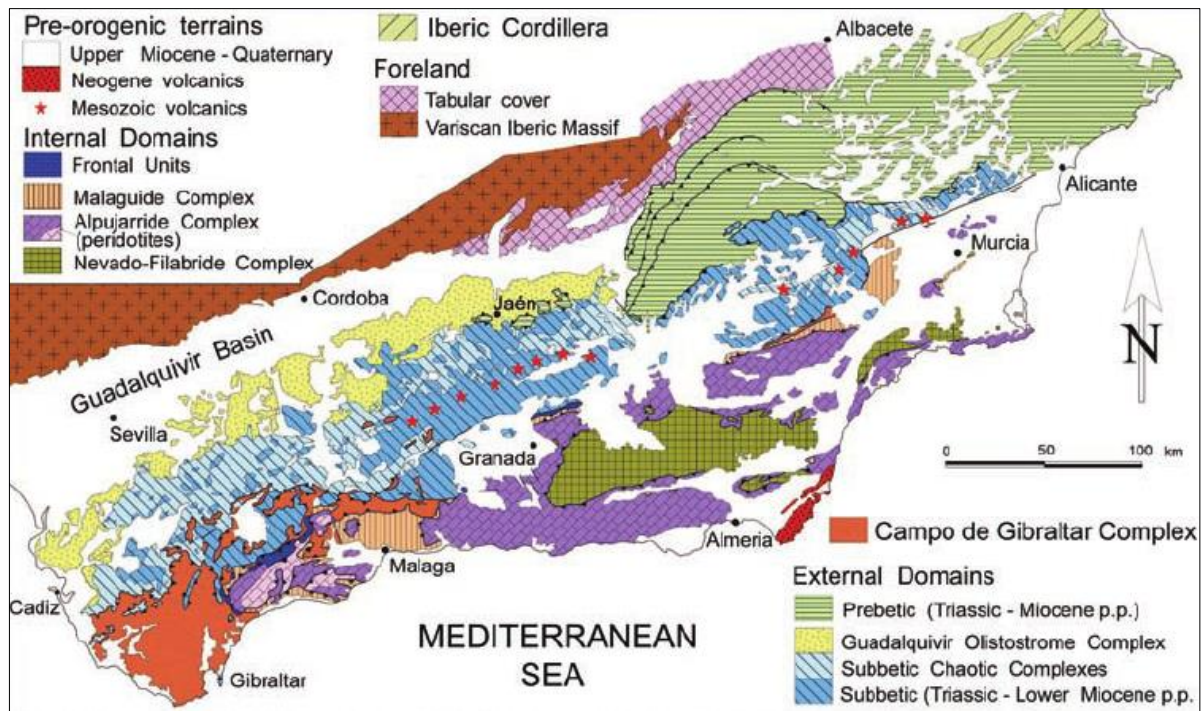


Figure 2.5. 2. Geological map of Betic Cordillera (Perrore et al., 2006).

- The External Zone corresponds to the area that constituted the southern continental margin of the Iberian plate during the Mesozoic and part of the Cenozoic periods. In this zone two domains are distinguished: the Prebetic (External and Internal), which corresponds to the area closest to the continent, and the Subbetic (External, Internal and Middle), corresponding to a more internal or southern part. In the western sector of the Betic Cordillera, occupying a position equivalent to the Internal Subbetic but with somewhat different stratigraphic characteristics, some authors differentiate the Penibetic domain (Martín Algarra and vera, 1982; Company et al., González-Donoso et al., 1983; Martín Algarra, 1987).
- The Internal Zone corresponds to paleogeographic domains foreign to the Iberian plate. It is divided into three tectonically superimposed complexes that are, from bottom to top: Nevado-Filábride, Apujárride y Maláguide. The two lower complexes are formed mainly by sedimentary rocks. The terms Dorsal and Rondaide are used to define the set of tectonic units that appear in front of the Internal Zone, in the western sector of the Cordillera.
- The Campo de Gibraltar Complex comprises several tectonic units constituted by sedimentary rocks in flysch facies, deposited in paleogeographic domains located between the External Zone, the Intenal Zone and the North African continental border.

- Neogenic basins, such as those of Ronda and Malaga, located on the northern and southern edges of the studied area, are formed on the External Zone and on the Internal Zone, respectively. The materials that fill them were deposited, fundamentally, after the main phase of folding that affected the Cordillera, as a consequence of the collision between the External Zone and the Internal Zone during the Lower-Middle Miocene.

The Sierra de las Nieves mountain range is located in an area where there is a contact between the Internal Zone and the External Zone of the Betic Cordillera. This contact constitutes a geological accident of great importance, inasmuch as both sides one of the same zone radically change the stratigraphy and the tectonic of the various units involved.

The carbonated sequence is folded forming a synclinal lying with verges towards the northwest and are affected by several families of faults (Liñan-Baena, 2005), that will be studied within this work. These families have the direction N130E, N35E and N90E. Several faults with direction N130E have delimited blocks raised and sunk as a tectonic horst, although the most important blocks are a sunken block in the western part and a raised block (Figure 2.5.3), with respect to the previous one, being in the latter where the large karstic ducts have been dislodged. Of lesser importance is a fourth family of N65E direction fractures that coincides with the direction of the syncline axis.

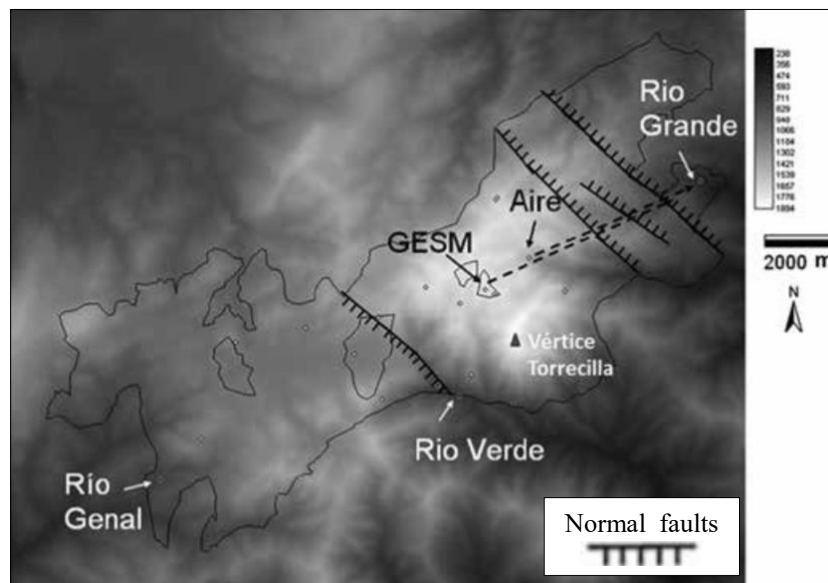


Figure 2.5. 3. Greater normal faults in the study area.

The karst system of Sierra de las Nieves has two blocks: one block that is located between the karst springs of Genal and Verde, and an uplifted block (with respect to the previous one) located between the karst springs of Verde and Grande. The network of large karst conduits is located mainly in the uplifted block. The dashed lines in the Figure 2.5.3 indicate the hydraulix connectivity between del G.E.S.M. pothole and Grande spring. The thin black line represents the border of the aquifer. (E. Pardo-Igúzquida, *El sistema kárstico de la Sierra de las Nieves (Málaga, España). Un ejemplo de un karst mediterráneo de relieve alto*, 2016).

2.6. Vegetation

The vegetation of the study area is very varied, mainly due to the geological complexity and the composition of the relief. In terms of soils, the main units built (Classification according to the Food and Agriculture Organization of the United Nations (FAO) in the plan of natural resources management in Sierra de las Nieves natural park) present are the leptosols, located on limestone and dolomites, and Cambisols, on loamy limestone. The vegetation series are arranged in the order of the geological materials (Cabezudo Artero, 1998). On the siliceous soils, the dominant vegetation series are the cork oaks with some indications of oak groves. On the limestone soils, in thermal and dry basal areas, dominate the junipers with Aleppo pines. In mid mountain there are holm oaks and *Abies pinsapo*. In the high mountain area, the deciduous forest of gall oaks and maples is characteristic. Finally, in the high summits of the mountain are dominated by the enebro-sabinar (Cabezudo Artero, 1998).



Figure 2.6. 1. Personal visit to Sierra de las Nieves (April 2018).

3. Data Used for the 3D Model Creation (Lineaments)

Superficial information of joints, fractures and faults from different geological maps were used for the realization of the 3D Discrete Fracture Model. The following maps were used:

- Geological map modified by Martín Algarra, 1987 (Cristina Liñan Baena, 2005. *Hidrogeología de acuíferos carbonatados en la unidad Yunquera-Nieves (Málaga)*). Instituto Geológico y Minero de España. Page 20). Figure 3.1.a.
- Map of lineaments, 1996 (Juan José Durán Valseo, PhD thesis, *Los sistemas Kársticos de la provincia de Málaga y su evolución: contribución al conocimiento paleoclimático del cuaternario en el mediterráneo occidental*, Madrid 1996, Page 66). Figure 3.2.a.
- Simplified geological map of the Sierra de las Nieves over a digital elevation model where the main faults, cave entries, and springs are indicated. (Pedrera, A. and al. *Structural control on karstic conduits in a collisional orogen (Sierra de las Nieves, Betic Cordillera, S Spain)*. *Geomorphology* 238: 15-26). Figure 3.3.a.
- MAGNA50 (Geological map of Spain at scale 1:50.000). Combination of geological maps 1051 Ronda (upper portion; A. del Olmo Sanz et al. 1981. Instituto Tecnológico GeoMinero de España) and 1065 Marbella (lower portion, E. Piles Mateo and al. 1972. Instituto Tecnológico GeoMinero de España) downloaded from the site www.igme.es. Figura 3.4.a.

All images were georeferenced with different types of transformation to obtain the lowest possible error. Once the rasters in question were georeferenced, all the joints, fractures and faults, in general terms lineaments, were manually drawn. These are presented in maps 3.1.b, 3.2.b, 3.3.b and 3.4.b.

To arrange and filter the information obtained, to reduce possible repetitions of information and probable errors due to georeferencing, map Figure 3.5.a, a representation of the previous maps, was synthesized overlapping the PNOA image (Figure 3.5.b). This verifies through the topography the possible correlations with faults and joints.

The PNOA images (National Plan of Aerial Orthophotography) are high resolution images (0.5 x 0.5 m), ECW or TIFF format with the TWF file of georeferencing. The geodetic reference system is ETRS89 in the Iberian Peninsula and REGCAN95 in the Canary Islands. The image corresponds to a photogrammetric flight with a scale of 1:30.000 using the reference system EPSG 25830.

The result of this synthesis is shown in Figure 3.6.

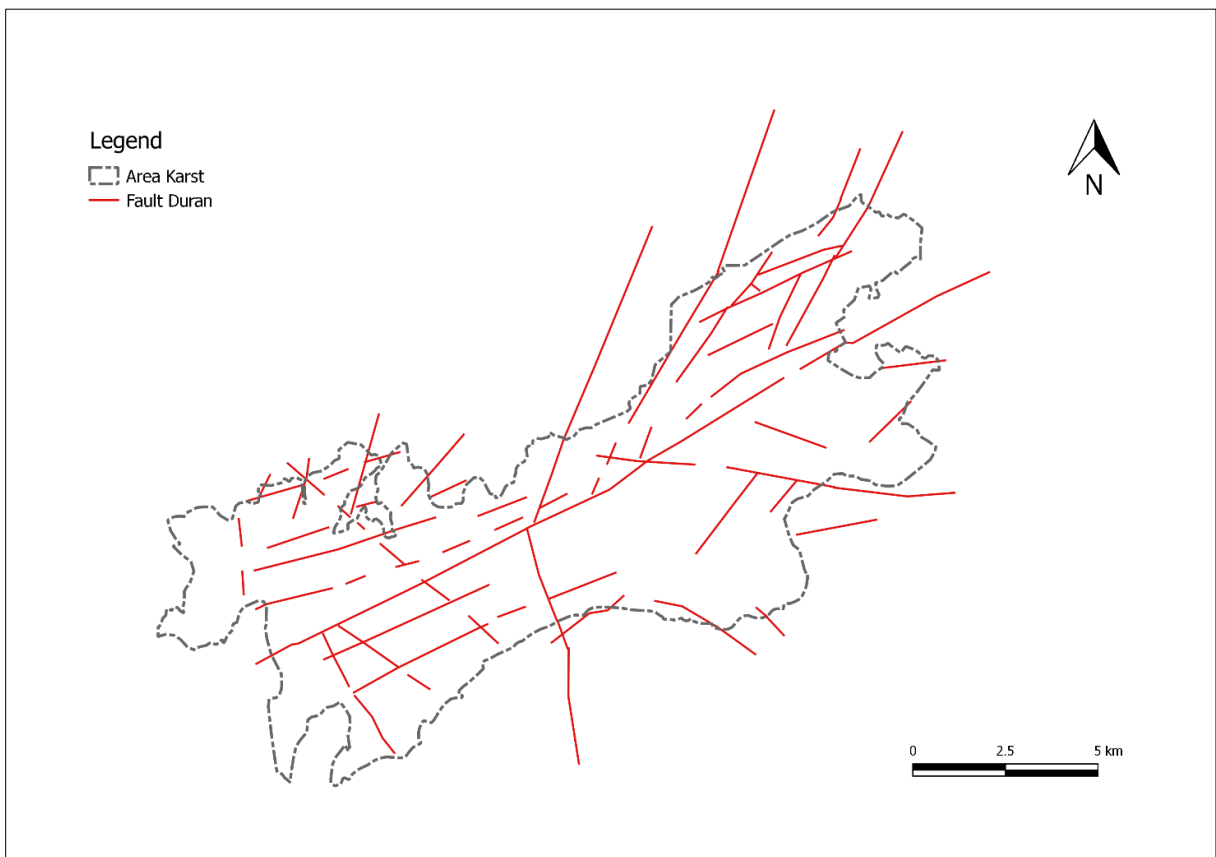
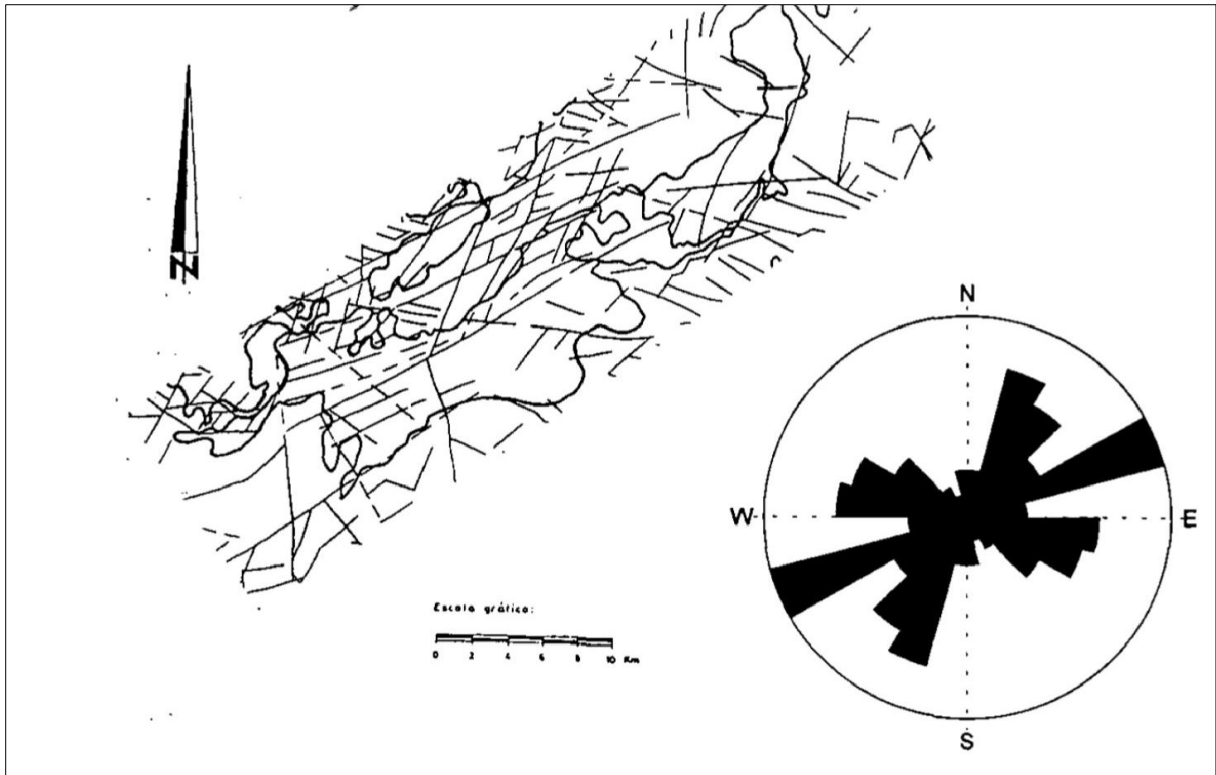


Figure 3.2. a) Lineaments for the central sector of the Serranía de Ronda: Sierra de Las Nieves and Siena Prieta. The orientation diagram (rose diagram) is elaborated with class intervals equal to 15° , Juan José Durán Valsero, 1996; b) Lineaments map. Prepared by the author from Figure 3.2.a

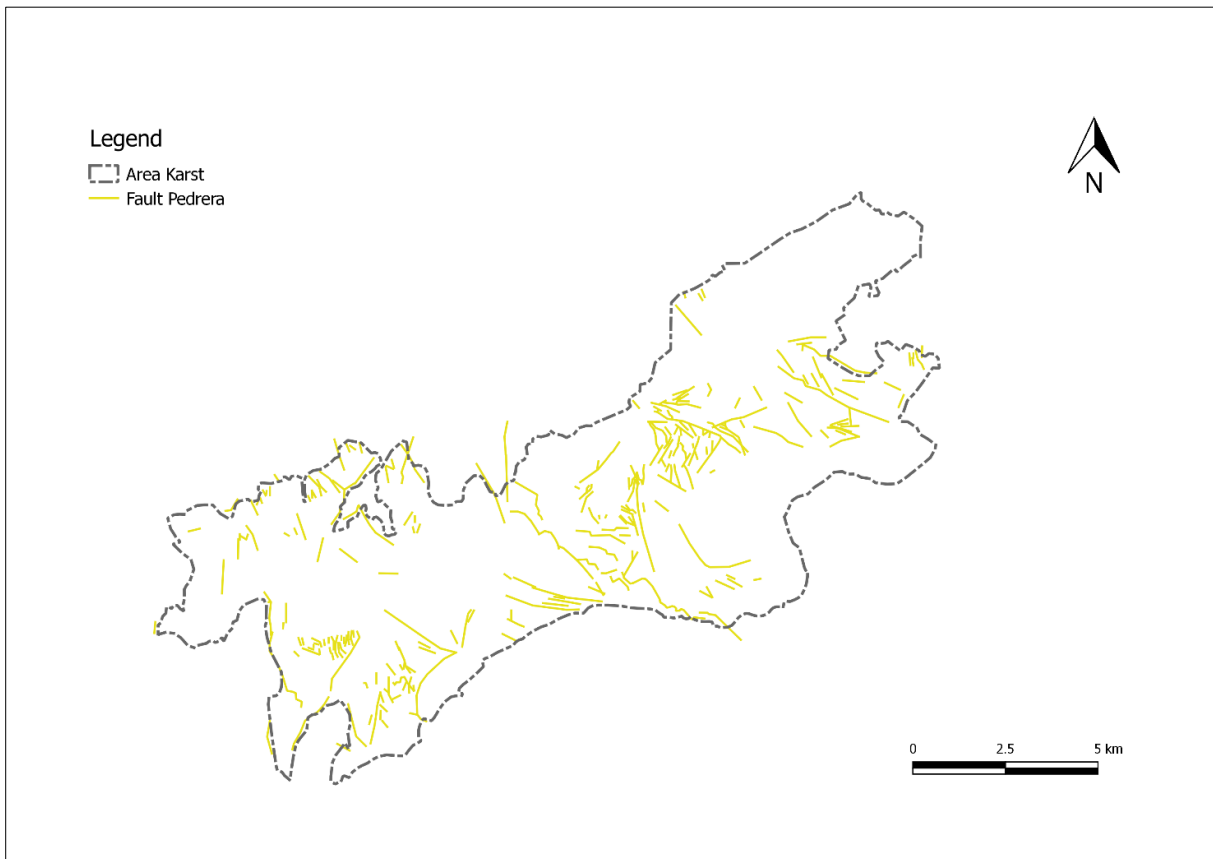
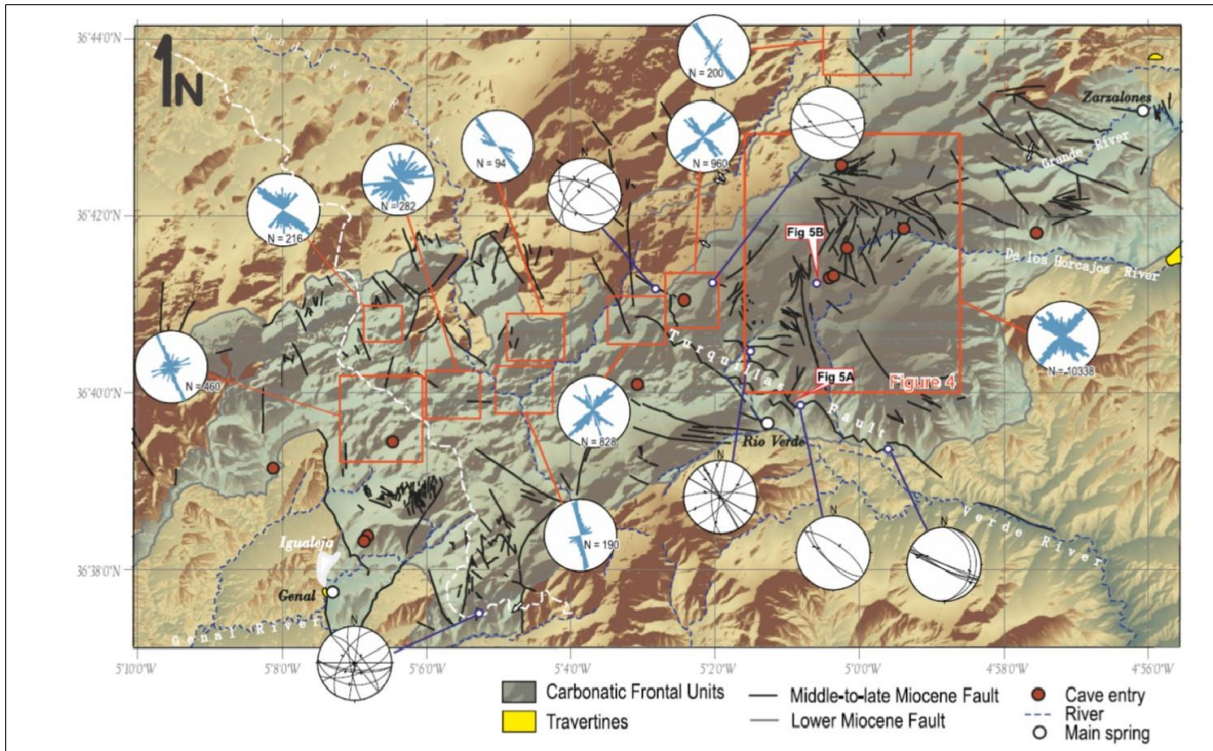


Figure 3.3. a) Simplified geological map of the Sierra de las Nieves over a digital elevation model where the main faults, cave entries, and springs are indicated. Joints (mostly subvertical) are represented in rose diagrams (in blue). Faults are plotted in stereographic projection, lower hemisphere, Pedrera, 2015; b) Lineaments map. Prepared by the author from Figure 3.3.a.

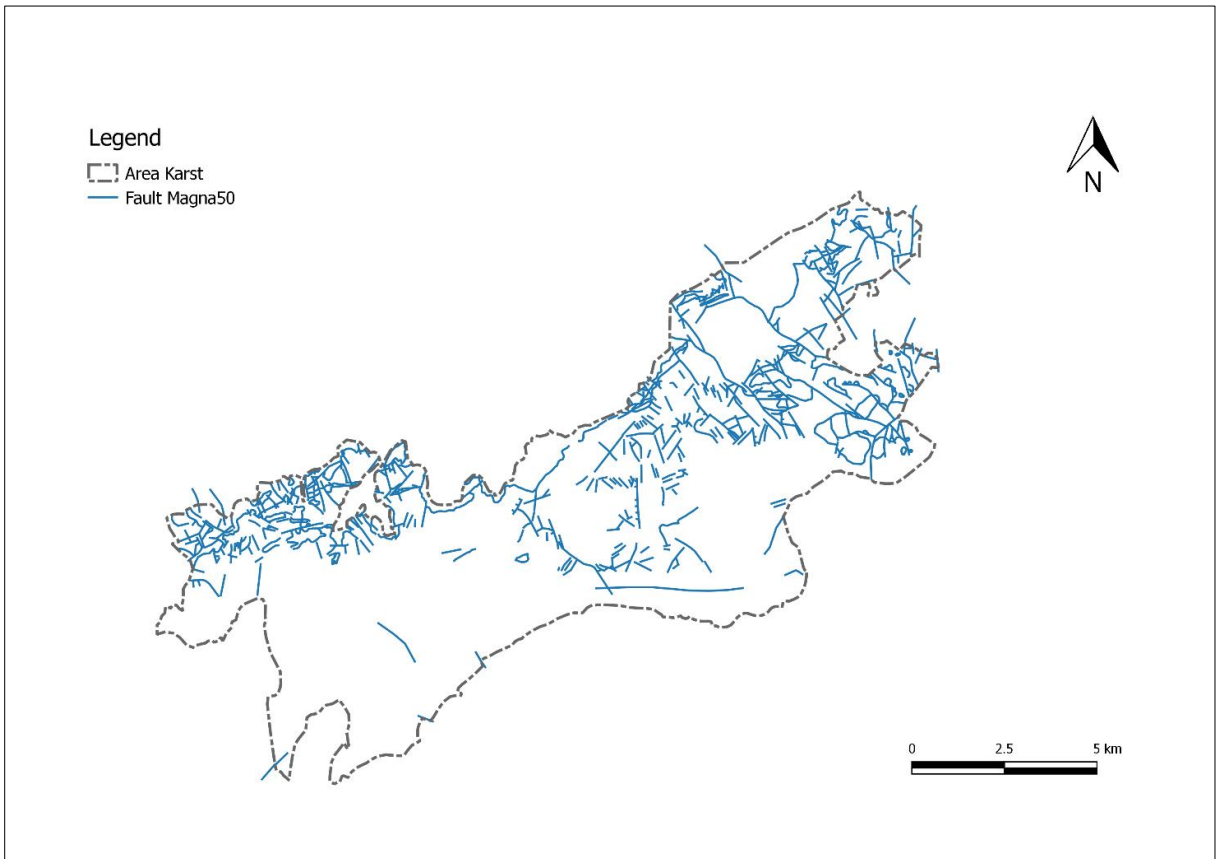
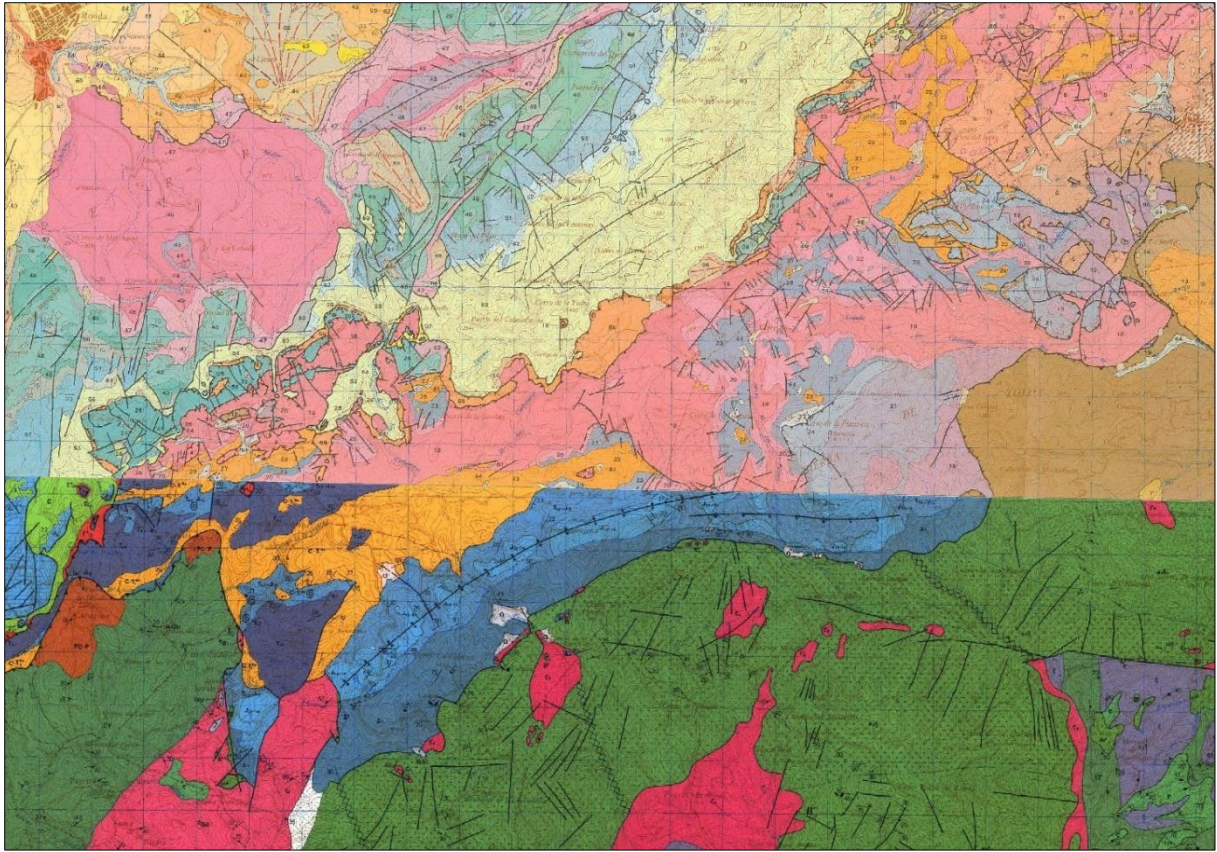


Figure 3.4. a) Combination of geological maps 1051 Ronda (1981) and 1065 Marbella (1972); b) Lineaments map. Prepared by the author from Figure 3.4.a.

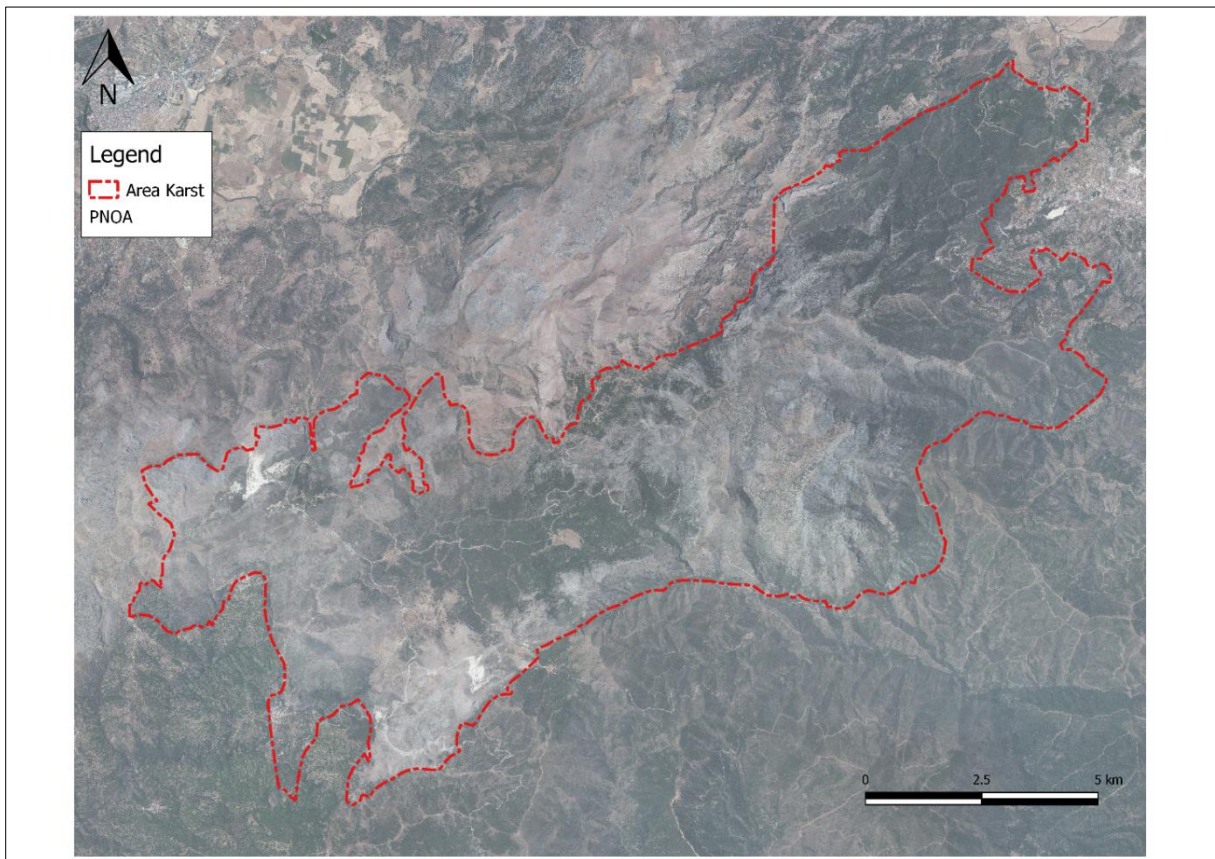
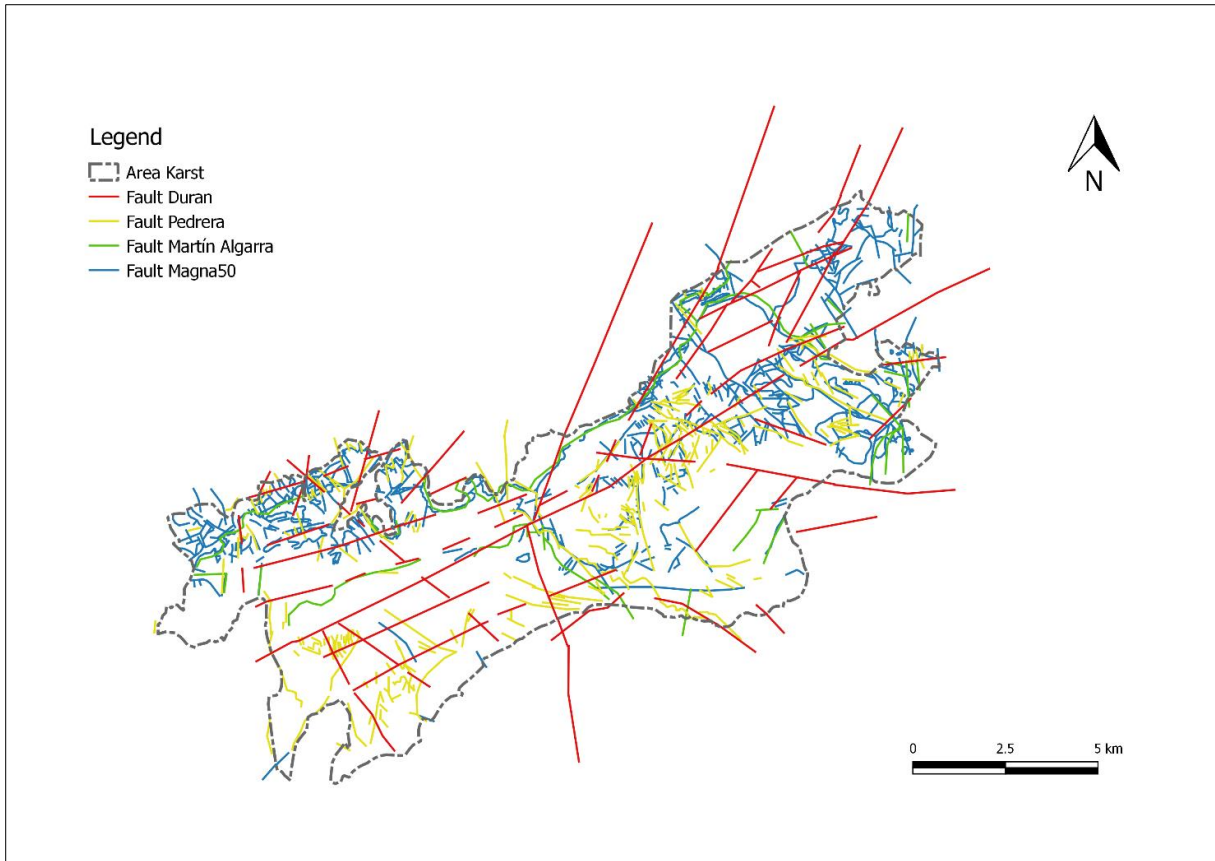


Figure 3. 5 a) Sum of lineaments from figures 3.1.b, 3.2.b, 3.3.b and 3.4.b. Prepared by the author; b) PNOA (National Plan of Aerial Orthophotography) of Sierra de las Nieves, 2013.



Figure 3.6. Synthesis map of lineaments, obtained from overlapping figures 3.5.a and 3.5.b.

After the image was synthesized, it was simplified in order to avoid a too high computational load subsequently in the realization of the 3D Model. Also in this case the PNOA image of the study area (Figure 3.5.b) was used. In figure 3.7 one can see how the simplification was carried out.



Figure 3.7. Example of how the simplification was made of Figure 3.6.

Finally, a directional analysis was carried out. First some sub-areas (Figure 3.8) were analysed, followed by the whole study area (Figure 3.9). This was done to understand if the study area can be considered homogeneous for the realization of the model and then to associate the lineaments obtained to tectonic events that occurred in the past.

From the analysis of the sub-areas of Figure 3.8 it was possible to understand that sub-areas 2, 4, 5 and 6 have a similar behaviour, mainly with fractures trending N60E-N70E and minor directional groups with N65E, N165E, N35E and N110E trends.

As regards sub-area 1, the main directions in descending order are N35E, N100E, N160E and in sub-area 3 they are N150E, N110E, N35E. It was decided, despite some differences in the rose diagrams of the different sub-areas, to consider the study area as a homogeneous area.

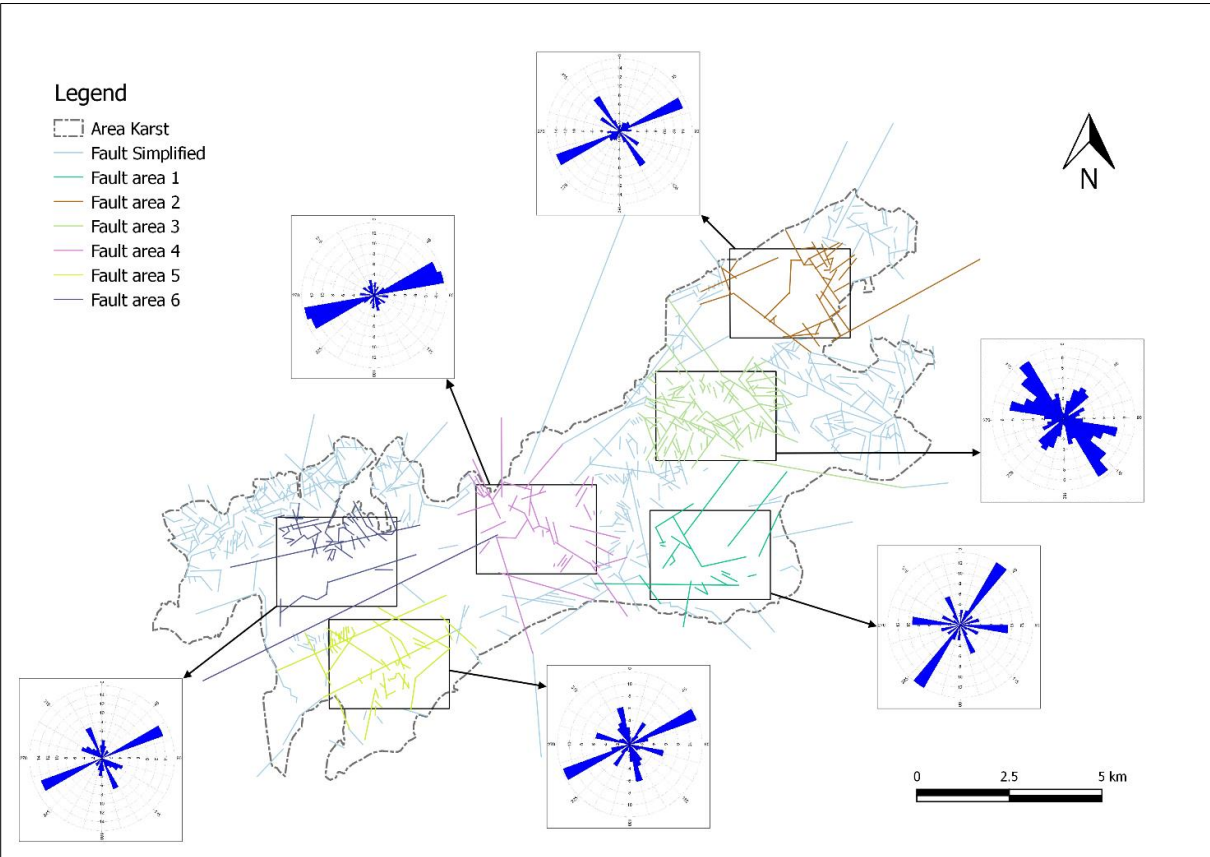


Figure 3. 8. Lineaments in the entire area and analysis of six sub-areas with the relative rose diagram (in blue, realized with RockWorks2016).

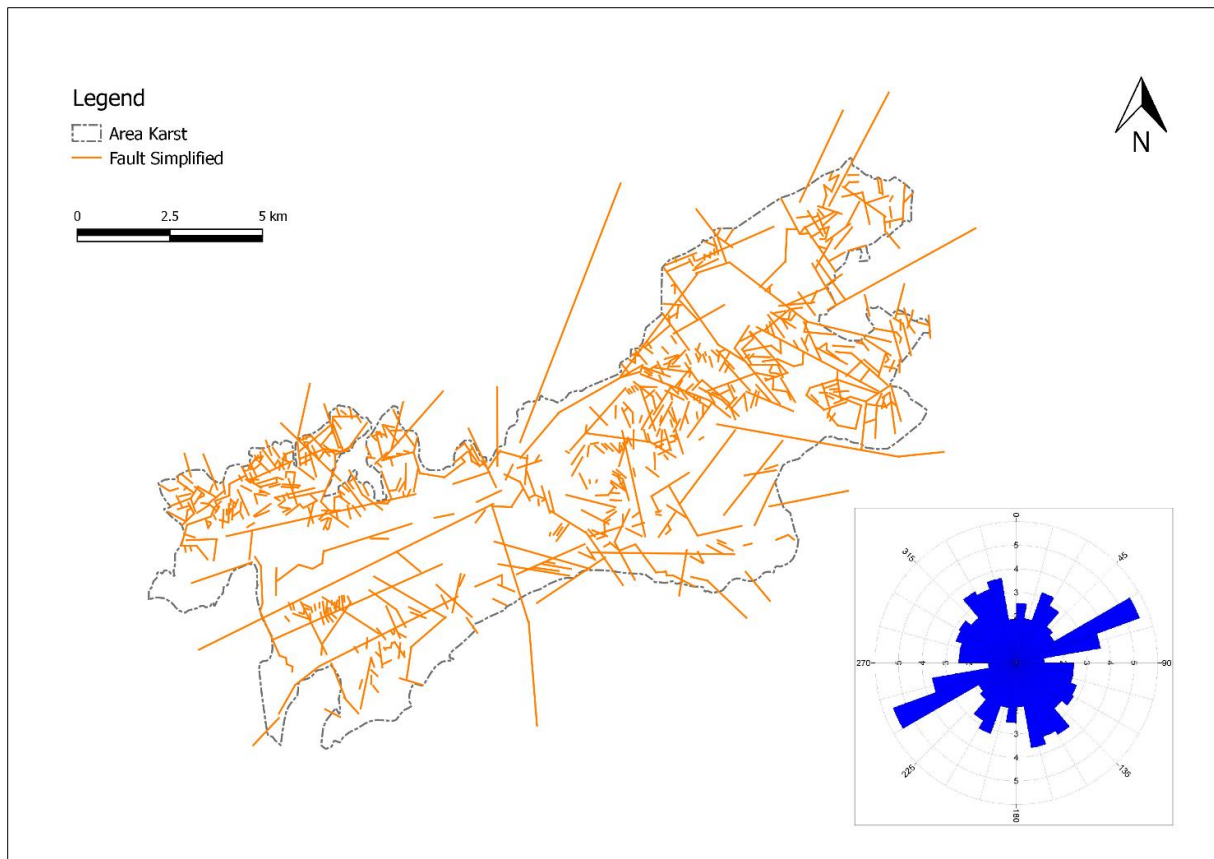


Figure 3. 9. Simplified lineaments and rose diagram (class intervals = 10°) of karst of the Sierra de las Nieves.

Also in Figure 3.9, all the simplified fractures are represented with the relative rose diagram of the whole area. From this figure it was possible to analyse that there are five main directions which are the same ones analysed in the subareas. For this reason, we have considered 5 different families of direction assigning each lineament to a family. The five families chosen are the following:

- *Family 1*: N50E - N85E
- *Family 2*: N135E - N175E
- *Family 3*: N15E - N50E
- *Family 4*: N85E - N135E
- *Family 5*: N5W - N15E

Once each lineament was assigned to its relative family, it was ascertained that no assignment errors had been committed with respect to the same fault, that is with respect to its tectonic origin. Some of the assignments were manually changed. Figures 3.10.a and 3.10.b show an example of the process realized on twenty lineaments.

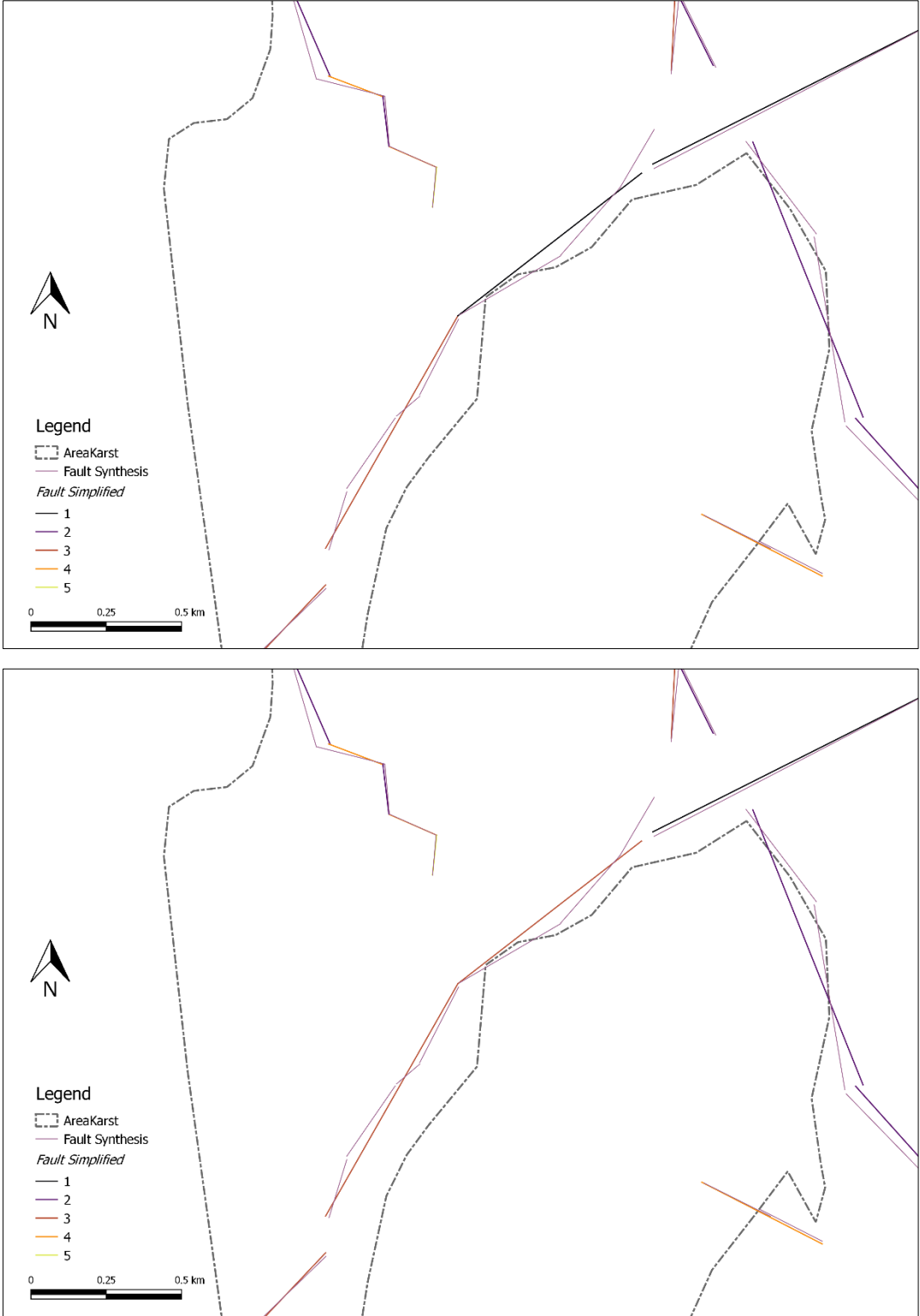


Figure 3. 10. a) Result of the assignment with respect to the rank of directions; b) Example of a manual correction related to assignments.

In the following image we can see the five family subdivision made and manually corrected. (Figure 3.11)

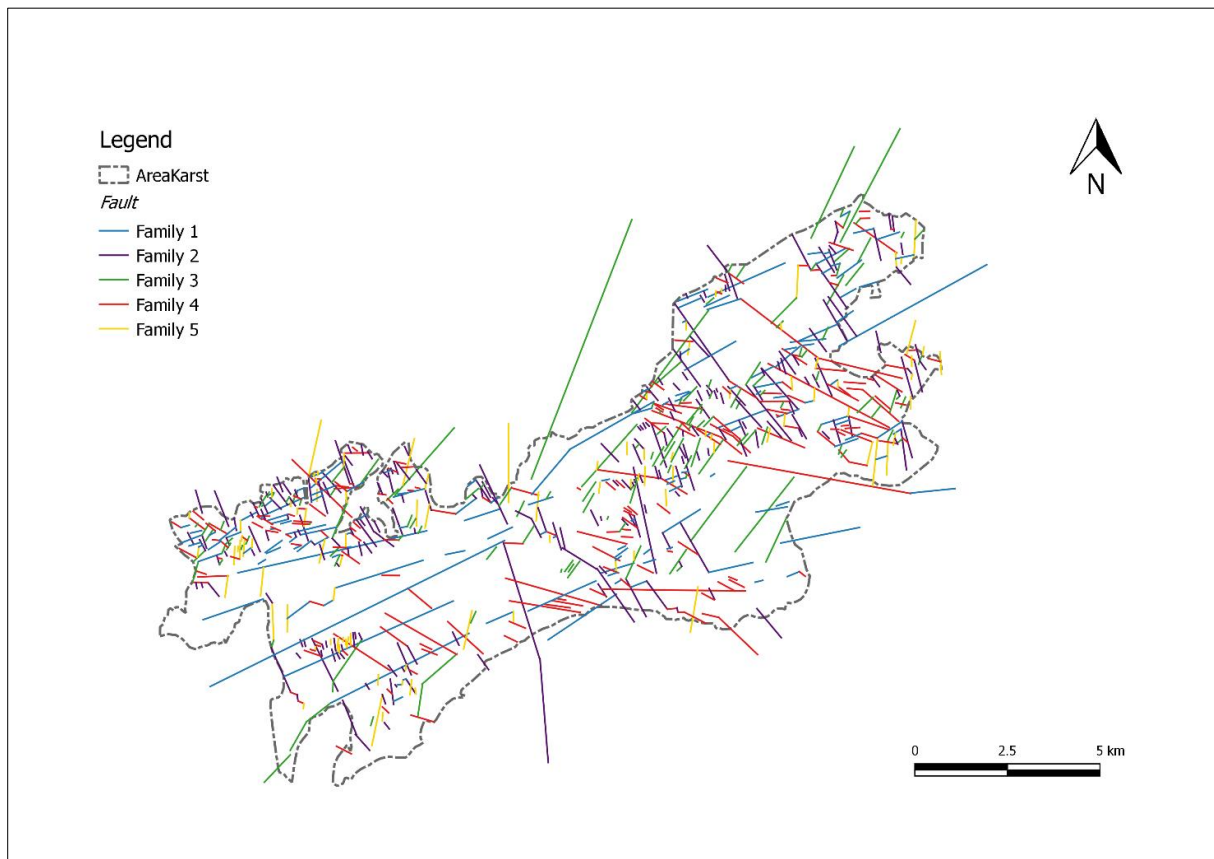


Figure 3. 11. Subdivision and assignment of fractures according to the trending of families

3.1. Tectonic Origin of Families

The literature of the study area was analyzed to verify if there were relations between the chosen families and the geotectonic origin. The massif has several types of discontinuities (faults, diaclases, karstified surfaces, striae) in different directions.

In total we considered 809 lineaments that are represented in the Figure 3.11 where we can distinguish different types of discontinuity that allowed us to discriminate the families. In the study by Cristina Liñan Baena (2005) 216 discontinuities were measured in situ, with a predominance of directions N-S to N15E and N135E to N165E. These directions correspond to two of the three types of modern fractures (formed from the Middle-Late Miocene) recognized by Benavente and Sanz de Galdeano (1999) in the Betic Cordillera. These two main directions correspond respectively to families 5 and 2.

Also according to the Liñan study there is a clear coincidence between the directions of the karstification surfaces and the fault planes; where most of the faults are normal or strike-slip faults with reverse components. The fault planes found by Liñan are N-S, N150E and N90E, the latter was not reflected in the analyses carried out in this thesis work.

The main directions of karstification measured by Liñan are N0-15E, N150E, N60E and N30E, which corresponds to families 5, 2, 1 and 3.

The microstructural analysis of the data obtained in the field (Liñan, 2005) allows one to highlight three tectonic phases, consistent with the observations made in nearby areas (López Chicano, 1992, Pistre et al., 1996, Andreo, 1997) although the chronology of them is difficult to establish formally. These three tectonic phases are:

1. Strike-slip phase, with a compression oriented approximately E-W. The age attributed to it is Lower Miocene. This phase may have created fractures with N60E and N120E directions. These fractures correspond to families 1 and 4.
2. Phase of strike-slip regime, with a compression that varies NNW-SSE to N-S. This phase is probably of the late Miocene age and is attributed to fractures with N10E and N130E directions, and these belong to families 5 and 4.
3. Extensive phase, attributed to the Pliocene and the Ancient Quaternary, is essentially visible on planes N-S and N135E to N150E, correspond to families 5 and 2.

The normal extensive phase seems to be the most marked in the massif, and it played an essential role in the acquisition of the hydrodynamic properties of the aquifer, as well as in karstogenesis (Liñan, 2005). This extensive phase caused the opening of fractures with N-S and NNW-SSE directions (families 5 and 2), such as the important fractures N130E (family 4) that cross the study area, favoring the development of karstification according to these directions. However, the flow of groundwater is not only conditioned by fracturing, but the stratification and geological structure also exert a great influence.

In the study carried out by Pedrera et al. (2015) three groups of features are highlighted. The most important set, considering its frequency and length, is composed of faults trending NW-SE to WNW-ESE and featuring high dip and normal to normal-dextral kinematics; most of the faults show straight planes with dip angles higher than 50-60°. One of the main high-dipping faults belonging to this group is the so-called Turquillas fault, which cross-cuts the contact between the Frontal Units and the peridotites (Pedrera et al. 2015). This group of fractures has been associated with middle-to-late Miocene age activity and corresponds to family 4.

The second group always recognized in the same study concerns faults with N30E-N40E directions (Family 3) with low strike dispersion, high dips and a normal to normal-dextral component. Finally, N160E-N180E normal-sinistral faults are also found. These are generally shorter and correspond to Family 2.

The study of Pedrera also analysed several caves including GESM cave with a prevailing N130E strike (Family 4), Prestá cave with N35E trend (Family 3) and the Sima del Aire cave where three marked groups were recognized trending N35E, N125E and N180E. These groups are respectively associable with families of lineaments 3, 4 and 5.

4. Statistical Analysis of the Lineaments

4.1 Introduction

In this chapter every family will be analysed to construct the model. This model will be realized with reference to the following observations:

- **Generation model**

FracMan7 has three separate fracture location algorithms on which the model is based. Which are chosen depending on what sort of behavior our fractures exhibit (FracMan 760 Manual):

- *The Baecher model* (Baecher, Lanney and Einstein, 1978) was one of the first well characterized discrete fracture models. In this model, the fracture centers are located uniformly in space, and, using a Poisson process, the fractures are generated as disks with a given radius and orientation. The Enhanced Baecher model extends the Baecher model by providing a provision for fracture terminations and more general fracture shapes. The Enhanced Baecher model utilizes fracture shapes initially generated as polygons with three to sixteen sides. These polygons can be equilateral (aspect ratio of one) or elongated, with the aspect ratio (major to minor axis size and orientation) defined by the user.
- *The Nearest Neighbour model* is a simple, non-stationary model in which fracture intensity P_{32} decreases exponentially depending on the distance from the "major features" identified by the user.
- *The Levy Lee model* is based upon "Levy Flight" (Mandelbrot, 1985). The Levy Flight process is a type of random walk, for which the length L of each step is given by the probability and cumulative distribution functions:

$$pdf(L) = 0 \quad \text{when} \quad L \leq L_s \quad (4.1.1)$$

$$pdf(L) = \frac{D}{L} \left(\frac{L_s}{L}\right)^D \quad (4.1.2)$$

$$cdf(L) = 0 \quad \text{when} \quad L \leq L_s \quad (4.1.3)$$

$$cdf(L) = 1 - \left(\frac{L_s}{L}\right)^D \quad (4.1.4)$$

where D is the fractal mass dimension of the point field of fracture centers, L is the distance from one fracture center to the next generated fracture center, and L_s is the minimal hop distance in the generation sequence. Levy Flight is a one-dimensional process for points on a line. In FracMan7, this is extended to two dimensions (fracture traces on a trace plane) and three dimensions (fractures in space).

The generation point is the center of the fracture. This option was chosen because it is faster than Surface Points.

A Fisher Distribution is commonly used for modelling the distribution of 3-dimensional orientation vectors (Fisher, 1953). It may be considered as the three-dimensional equivalent of a Normal distribution wrapped over the surface of a sphere. The variance of the orientations is equal in all directions from the mean orientation and a cone that intersects the sphere as a small-circle describes the confidence region. (Graham Borradaile, 2003).

Fisher's model is summarised in its simple form of a probability density function (PDF) that defines the frequency (density) of orientations in a small area on the sphere as:

$$PDF = \frac{k}{4\pi \sin k} \cdot \exp(k \cdot \cos \rho) \quad (4.1.6)$$

Where ρ is the angular deviation from the mean vector, in degrees, and k is the "Fisher constant" or dispersion factor. A simple approximation to k is given by Fisher's k :

$$k \approx \frac{n-1}{n-R} \quad (4.1.7)$$

Here, n is the number of orientations sampled and R is the magnitude of the resultant vector.

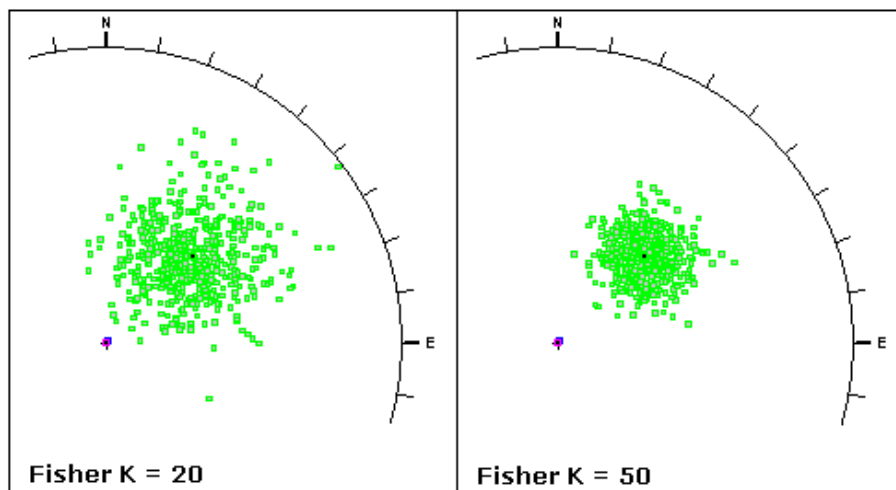


Figure 4.1.2. Effect of Fisher k on a randomly generated joint set of 500 samples (<https://rocscience.com>).

$\rho \backslash k$	0.1	1	2	5	10	50	100	200	500	∞
0	0.79	0.77	0.70	0.53	0.39	0.19	0.14	0.11	0.07	Sin ρ
5	0.79	0.77	0.70	0.54	0.40	0.21	0.17	0.14	0.12	
10	0.79	0.77	0.70	0.54	0.43	0.25	0.22	0.20	0.20	
20	0.79	0.77	0.72	0.58	0.49	0.38	0.37	0.36	0.36	
30	0.79	0.78	0.74	0.64	0.58	0.53	0.52	0.52	0.52	
40	0.79	0.78	0.76	0.71	0.68	0.66	0.66	0.66	0.66	
50	0.79	0.78	0.78	0.77	0.77	0.77	0.77	0.78	0.78	
60	0.79	0.79	0.79	0.82	0.85	0.87	0.87	0.87	0.87	
70	0.79	0.80	0.82	0.87	0.90	0.94	0.94	0.94	0.94	
80	0.79	0.80	0.83	0.90	0.94	0.98	0.98	0.99	0.99	
90	0.79	0.80	0.83	0.91	0.95	0.99	0.99	1.00	1.00	

Table 4.1.1. - $1/C_{32}$ with different values of k and ρ (After Wang, 2006).

In this way a first approximation of the P_{32} parameter was calculated which will be very important when the Fracture Model is simulated. However, when the model is validated, it will be important to check the P_{32} value calculated with the Wang formula.

- **Fracture orientation**

As for the distribution of the orientations, as previously stated, the Fisher function was used. To characterize this function, three parameters are needed. The first is the average of the orientations, the second the inclination $90^\circ - \rho$, taking into consideration the pole type representation. In general, poles and dip vectors are terms used to define the orientation of a plane in space. Fractures in FracMan7 are modelled as planar polygons and use poles or dips to describe their orientation. The pole is a vector normal to the fracture plane and usually (by convention) points downward (Figure 4.1.3). The third parameter to define Fisher's distribution for fracture orientation is k , which indicates the concentration of the distribution.

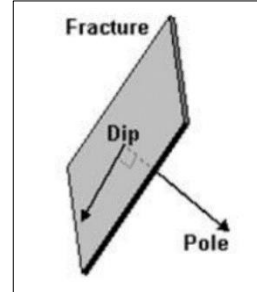


Figure 4.1.3. Difference between Pole and Dip.

- **Fracture size**

FracMan7 allows the user to convert trace length to fracture radius automatically. Through *Trace Length Fracture Size*, it was possible to analyse the distribution that best describes the behaviour of the lineaments referred to as lengths. In all five families, the distribution function that best represents this behaviour is the lognormal function.

Fracture size is specified in terms of the equivalent radius of the fractures before termination. The equivalent radius, r_e , is defined by the radius of the circle with an area equal to the area of the polygon, A_f , which represents the fracture:

$$A_f = \pi r_e^2 \quad (4.1.8)$$

- **Termination probability**

For all models, fracture termination is specified by the termination probability, P_T . P_T is the probability that a fracture will terminate given an intersection with another fracture:

$$P_T \cong \frac{N_T}{N_{Fi}} \quad (x.1.9)$$

where N_T is the number of T intersections for fractures in this set with fractures from previously generated sets, and N_{Fi} is the number of fractures in the set having intersections with fractures from previously generated sets. If N_{Fi} is zero, then P_T is zero. The relationship is not exact, because when FracMan7 terminates fractures at intersections, any intersections with fractures on the portion of the fracture discarded cannot be counted toward N_{Fi} . The value of P_T varies from 0 to 1, or it can be expressed as a percentage.

This form of termination disturbs the distribution of fracture size, since portions of fractures are "discarded" if they extend beyond the intersection where termination occurs. This is only a problem for high termination percentages.

4.2. Family 1

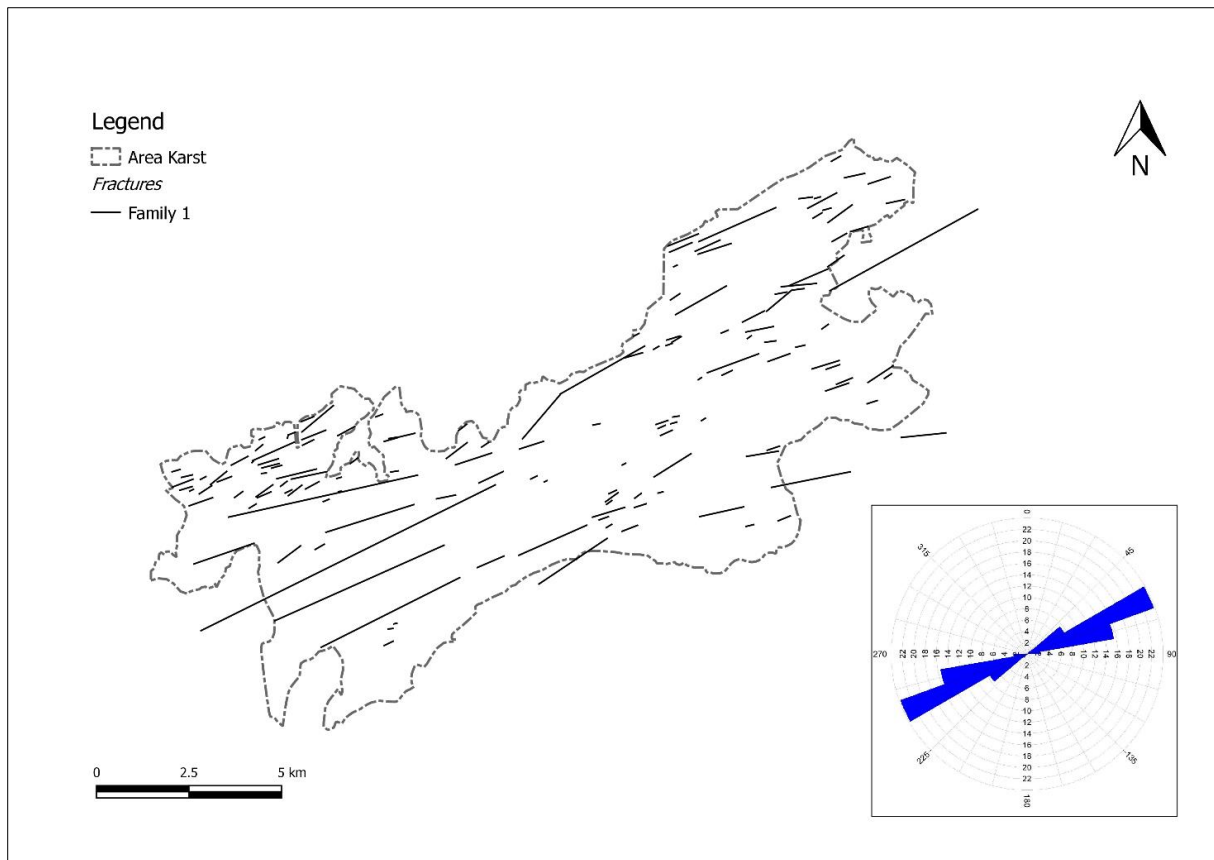


Figure 4.2. 1. Lineaments and rose diagram of Family 1.

There are 147 lineaments place in Family 1, direction N50E-N85E where the tectonic origin may be associated with the age of the Lower Miocene.

In the following figure the histogram of lengths with its statistical summary is shown.

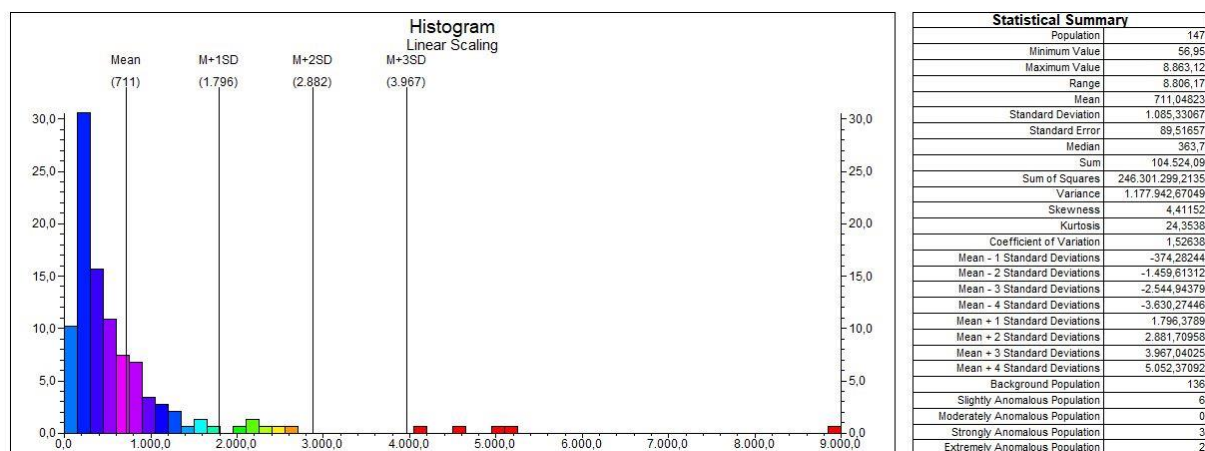


Figure 4.2. 2. Lengths histogram expressed in meters (bin = 150 m, the relative percentage is on the ordinates) and its statistical summary of Family 1 (RockWorks2016).

4.2.1. Generation model

For the generation of the model it was decided to do the spatial study through an older version of FracMan (1998) that supported this analysis with many more generation models than the FracMan7. The analysis performed with FracMan1998 is shown below:

```

Version: Fracsys 2.602  Date: 17:09 Jan 31 19118
=====
                Baecher Analysis

                File: familia1.f2d

Region: Upper-Left  (211.48,16125.53)
Region: Lower-Right (21359.71,1586.12)
Grid Size (min,max) (2000.00,7000.00)

                Chi Squared: 9
Confidence level: 97.35  %
-----
Box Dimension: 1.517
Correlation:    0.9887
    
```

Figure 4.2.1. 1. Results of Spatial Analysis for Family 1 with FracMan1998.

For the Family 1 it was decided to use the *The Baecher model*.

4.2.2. Global fracture intensity P_{32}

For the calculation of parameter P_{32} , as explained in the introduction of chapter 4.1, it was necessary to proceed with the calculation of the conversion parameter C_{32} from table 4.1.1. To achieve this calculation, the characteristic parameters of the Fisher distribution were defined by comparing the data analysed in the literature of the study area. For Family 1 the parameters are:

$$k = 65$$

$$\rho = 70$$

Obtaining: $1/C_{32} = 0.94$ and the conversion factor $C_{32} = 1.06$

For the calculation of P_{32} , the intensity $P_{21} = 0.0007445 \text{ m}^{-1}$ was calculated through FracMan7, which allowed the calculation of the first approximation of P_{32} , through formula 4.1.5. This was equal to 0.0007891 m^{-1} .

k	ρ	$1/C_{32}$	C_{32}	$P_{21} [L^{-1}]$	$P_{32} [L^{-1}]$
65	70	0.94	1.06	0.0007445	0.0007891

Table 4.2.2. 1. Parameters for the first approximation of the P_{32} calculation for Family 1.

4.2.3. Fracture orientation

The Pole type orientation was specified. To represent the Fisher function for the description of the distribution of the orientations one needs the parameters k and ρ of each family, in this case present in table 4.2.2.1. Finally, the value of the median of the directions of the fractures is necessary, which for the Family 1 is equal to N67.5E. 90° (α) must be added or subtracted to this value, depending on the inclination characteristic for this family. In Figure 4.2.3.1 the Fisher function is shown in stereographic representation.

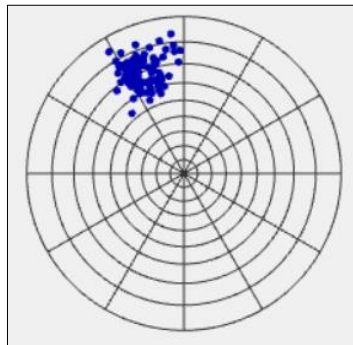


Figure 4.2.3. 1. Fisher distribution for Family 1 with stereographic representation (FracMan7).

4.2.4. Fracture size

From the analysis carried out for the distribution of lengths, the distribution that best fits our data, as already mentioned above, is Lognormal. The following are the results of this analysis:

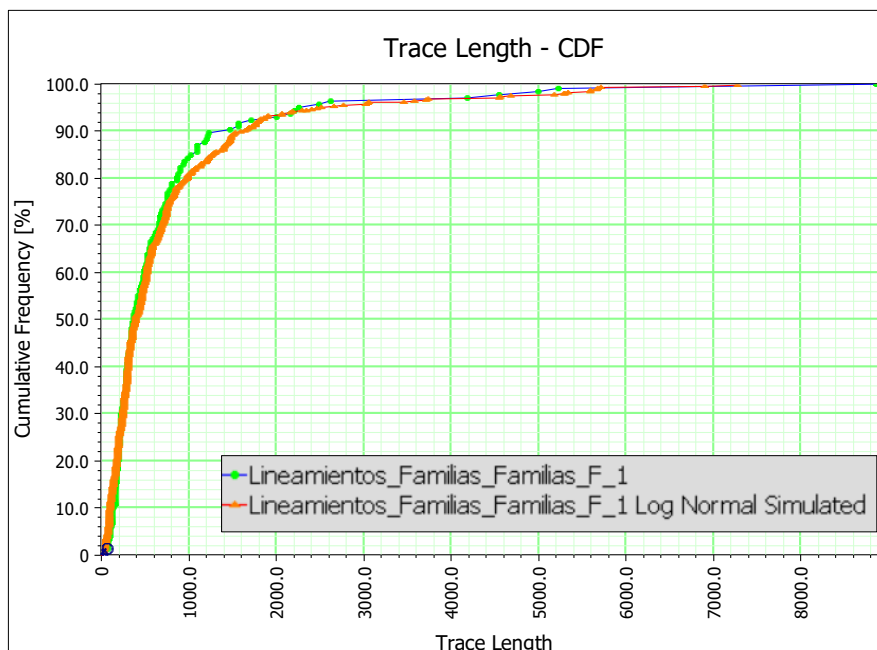


Figure 4.2.4. 1. Best fit of Lognormal distribution for Family 1 (Trace Length expressed in meters).

<i>Lineamientos_Familias_Familias_F_1</i>	
Trace Len Mean	711.018
Trace Len Dev	1085.33
Radius Mean	146.921
Radius Deviation	211.945
Sim. Trace Len Mean	731.163
Sim. Trace Len Dev	1020.29
K-S Test	0.0612245
Significance	0.938833

Table 4.2.4. 1. Results of Lognormal simulation fit (Family 1).

The values necessary for the *Fracture Size* to execute the simulation are the mean and the standard deviation of the equivalent radius, respectively 146.92 and 211.94.

4.2.5. Termination probability

Termination probability of Family 1 calculated is $P_T = 0.71$

4.3. Family 2

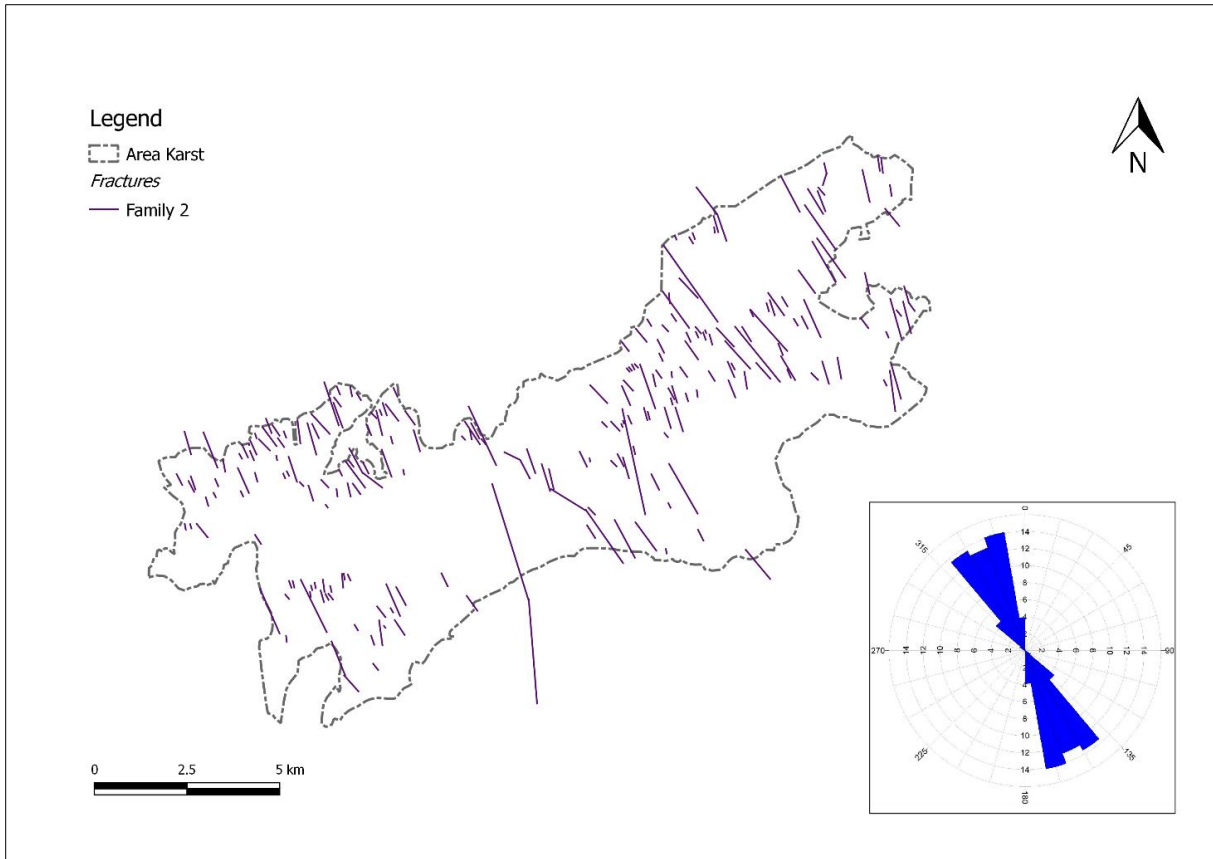


Figure 4.3. 1. Lineaments and rose diagram of Family 2.

The are 233 lineamentes placed in Family 2, direction N135E-N175E and the tectonic origin may be associated with the Late Miocenic Age. This family is very important for the development of karst.

In the following figure the histogram of lengths with its statistical summary is shown.

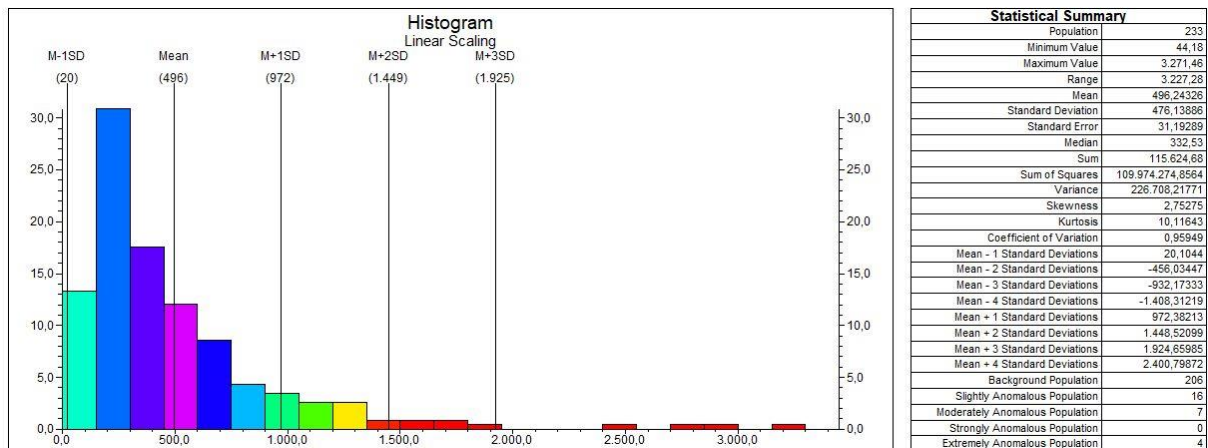


Figure 4.3. 2. Lengths histogram expressed in meters (bin = 150 m, the relative percentage is on the ordinates) and its statistical summary of Family 2 (RockWorks2016).

4.3.1. Generation model

It was decided to use the *The Baecher model* for Family 2. The results of spatial analysis of FracMan1998 are shown below:

```

Version: Fracsys 2.602  Date: 17:14 Jan 31 19118
=====
                Baecher Analysis

File: familia2.f2d

Region: Upper-Left  (422.96,15966.91)
Region: Lower-Right (20936.75,528.71)
Grid Size (min,max) (2000.00,7000.00)

Chi Squared: 10
Confidence level: 95.29  %
-----
Box Dimension: 1.656
Correlation: 0.9917
    
```

Figure 4.3.1. 1. Results of Spatial Analysis for Family 2 with FracMan1998.

4.3.2. Global fracture intensity P_{32}

As explained for Family 1 in chapter 4.2.2, the parameters necessary for the first approximation of P_{32} intensity have been calculated. The parameters are shown in the table below:

k	ρ	$1/C_{32}$	C_{32}	$P_{21} [L^{-1}]$	$P_{32} [L^{-1}]$
50	85	0.99	1.01	0.0008354	0.0008437

Table 4.3.2. 1. Parameters for the first approximation of the P_{32} calculation for Family 2.

4.3.3. Fracture orientation

The median of directions of this group of lineaments is N155E.

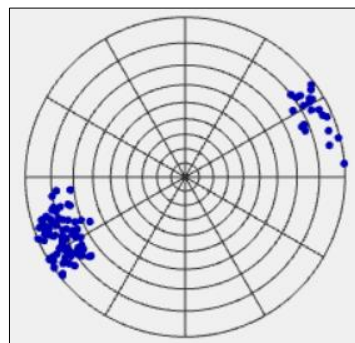


Figure 4.3.3. 1. Fisher distribution for Family 2 with stereographic representation (FracMan7).

4.3.4. Fracture size

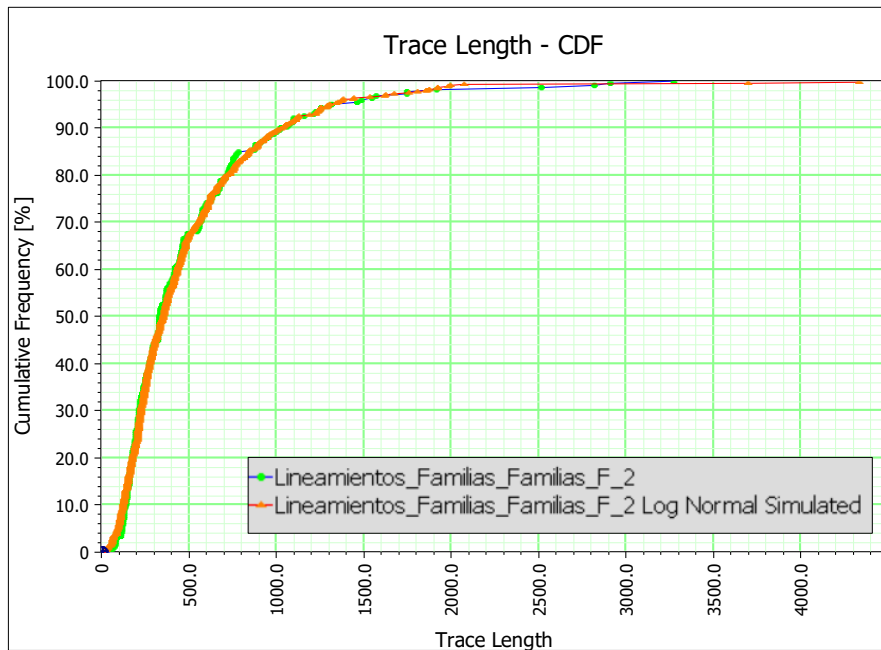


Figure 4.3.4. 1. Best fit of Lognormal distribution for Family 2 (Trace Length expressed in meters).

<i>Lineamientos_Familias_Familias_F_2</i>	
Trace Len Mean	496.244
Trace Len Dev	476.139
Radius Mean	177.772
Radius Deviation	156.712
Sim. Trace Len Mean	484.474
Sim. Trace Len Dev	445.359
K-S Test	0.0429185
Significance	0.980481

Table 4.3.4. 1. Results of Lognormal simulation fit (Family 2).

The values necessary for the *Fracture Size* to execute the simulation are the mean and the standard deviation of the equivalent radius, respectively 177.72 and 156.71.

4.3.5. Termination probability

The termination probability of Family 2 calculated is $P_T = 0$.

4.4. Family 3

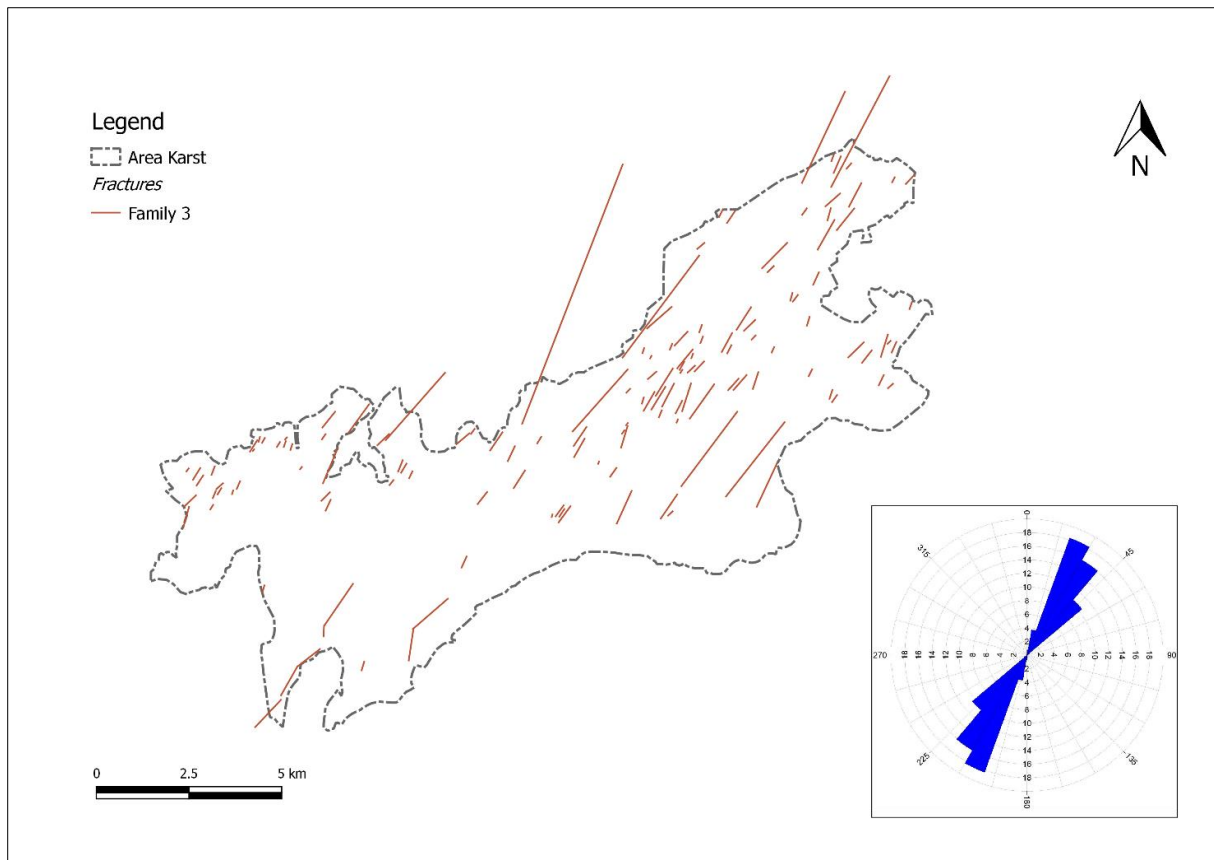


Figure 4.4. 1. Lineaments and rose diagram of Family 3.

There are 137 lineaments placed in Family 3, direction N15E-N50E and as regards the tectonic origin, nothing exhaustive was found in the literature of the study area.

In the following figure the histogram of lengths with its statistical summary is shown.

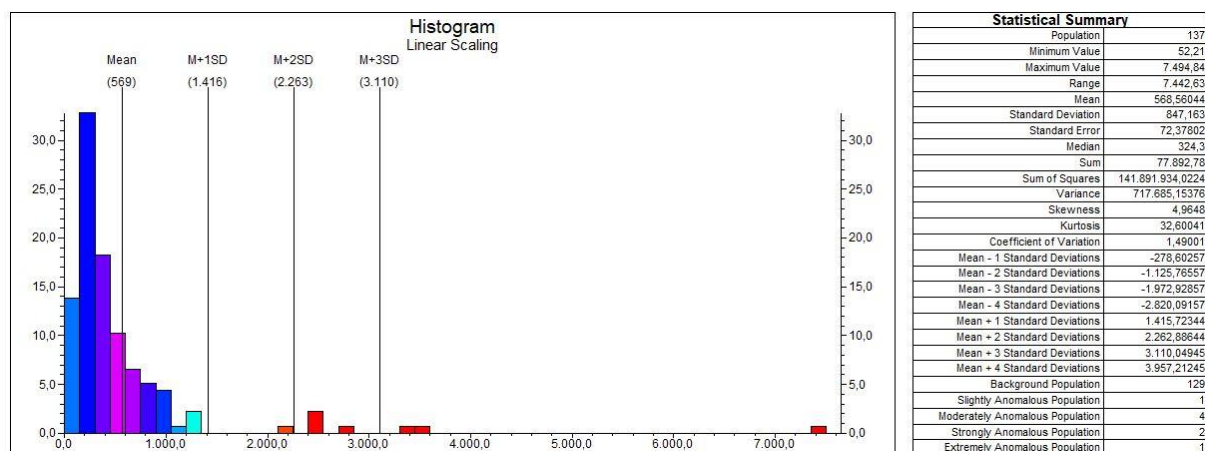


Figure 4.4. 2. Lengths histogram expressed in meters (bin = 150 m, the relative percentage is on the ordinates) and its statistical summary of Family 3 (RockWorks2016).

4.4.1. Generation model

For the Family 3 the best result of spatial analysis given by was the *Power Law model*, as can be seen in Figure 4.4.1.1.

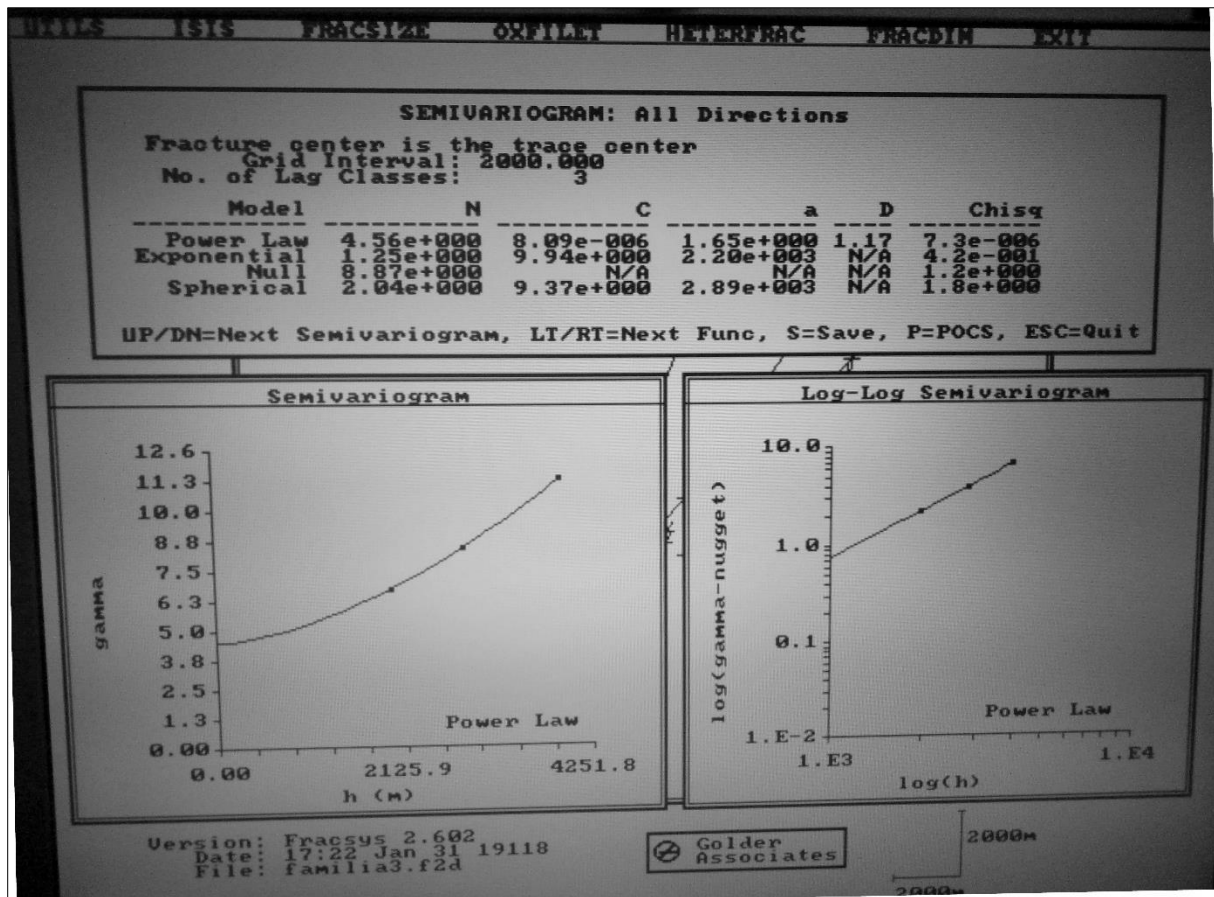


Figure 4.4.1. 1. Results of Spatial Analysis for Family 3 with FracMan1998.

Since FracMan7 does not support the *Power Law model*, it was decided to opt for *The Baecher model*.

4.4.2. Global fracture intensity P_{32}

Table 4.4.2.1. shows the parameters for the first approximation of the P_{32} for Family 3.

k	ρ	$1/C_{32}$	C_{32}	$P_{21} [L^{-1}]$	$P_{32} [L^{-1}]$
65	85	0.99	1.01	0.0005169	0.0005221

Table 4.4.2. 1. Parameters for the first approximation of the P_{32} calculation for Family 3.

4.4.3. Fracture orientation

The median of directions of this family of lineaments is N32.5E

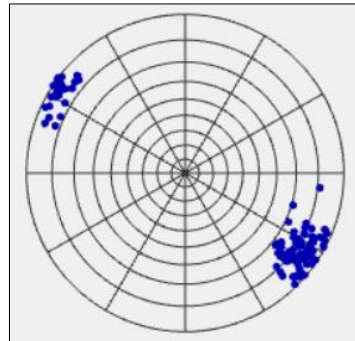


Figure 4.4.3. 1. Fisher distribution for Family 3 with stereographic representation (FracMan7).

4.4.4. Fracture size

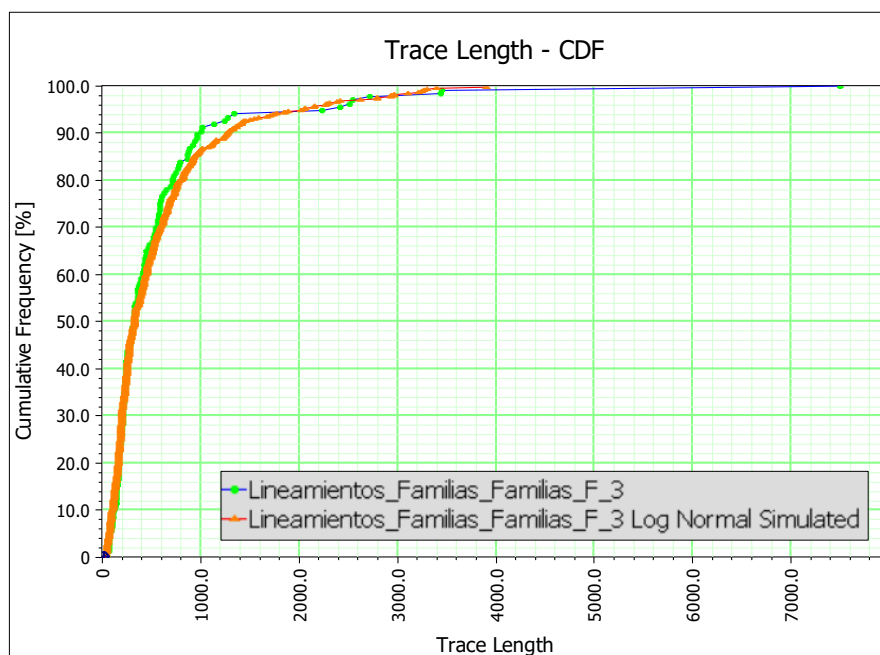


Figure 4.4.4. 1. Best fit of Lognormal distribution for Family 3 (Trace Length expressed in meters).

<i>Lineamientos_Familias_Familias_F_3</i>	
Trace Len Mean	568.561
Trace Len Dev	847.163
Radius Mean	121.482
Radius Deviation	170.919
Sim. Trace Len Mean	554.857
Sim. Trace Len Dev	625.701
K-S Test	0.0656934
Significance	0.920318

Table 4.4.4. 1. Results of Lognormal simulation fit (Family 3).

The values necessary for the *Fracture Size* to execute the simulation are the mean and the standard deviation of the equivalent radius, respectively 121.48 and 170.92.

4.4.5. Termination probability

The Termination probability of Family 3 calculated is $P_T = 0$.

4.5. Family 4

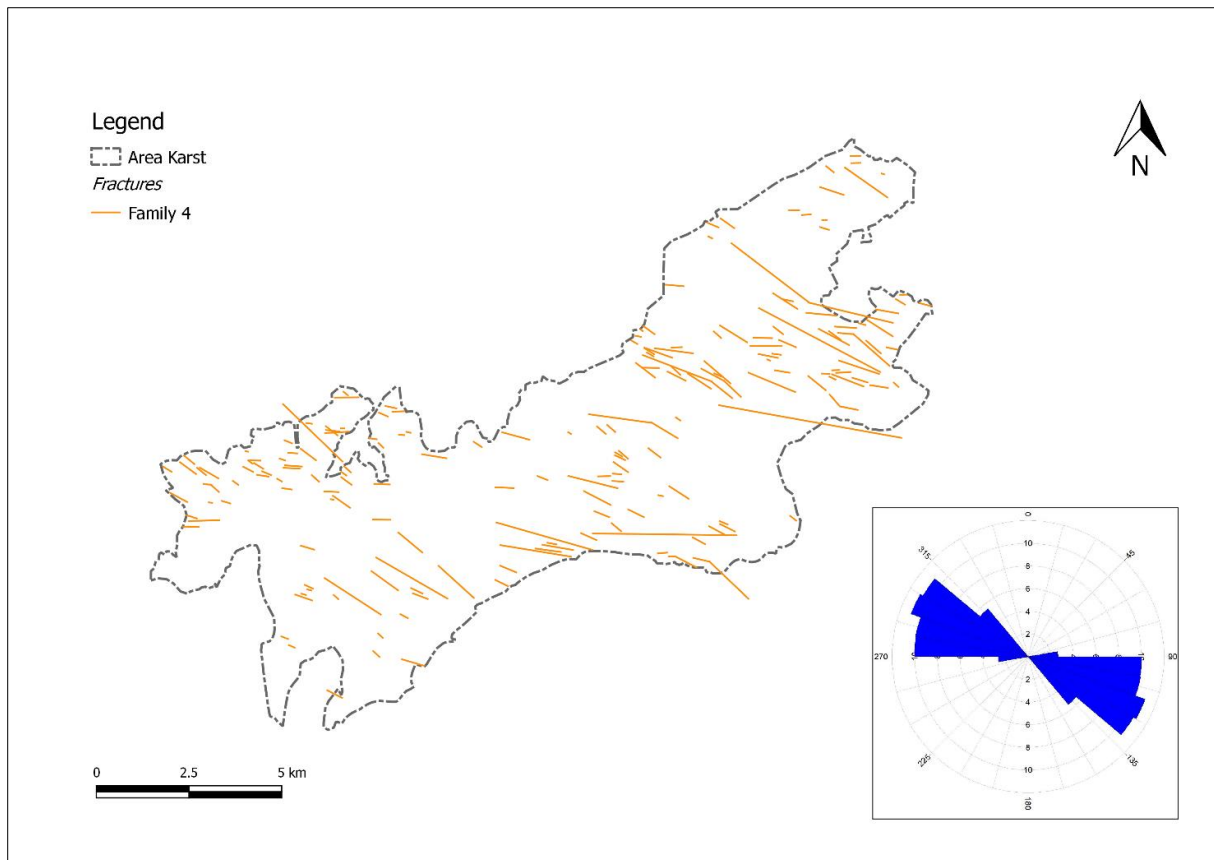


Figure 4.5. 1. Lineaments and rose diagram of Family 4.

There are 195 lineaments placed in Family 4, direction N85E-N135E and the tectonic origin may be associated with the Lower Miocenic Age.

In the following figure the histogram of lengths with its statistical summary is shown.

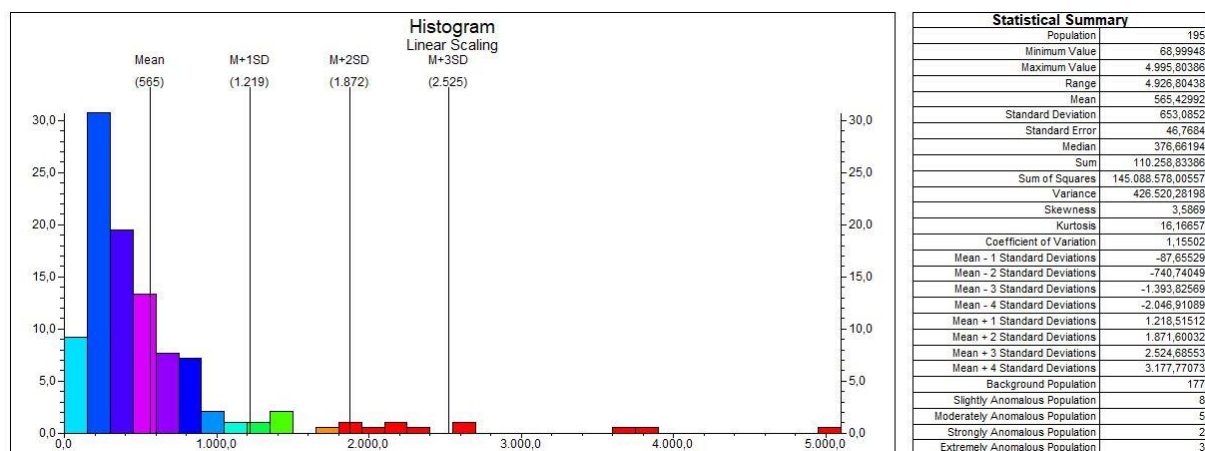


Figure 4.5. 2. Lengths histogram expressed in meters (bin = 150 m, the relative percentage is shown on the ordinates) and its statistical summary of Family 4 (RockWorks2016).

4.5.1. Generation model

For the generation of the Family 4 model, which has a visually different distribution from the others, the analysis carried out with FracMan1998 led to the decision to use the *Levy Lee model*.

The following figure shows the spatial analysis carried out for Family 4, where it can be seen that the Levy Lee model is perfectly suited to the spatial distribution, with the significance level equal to 97.31%.

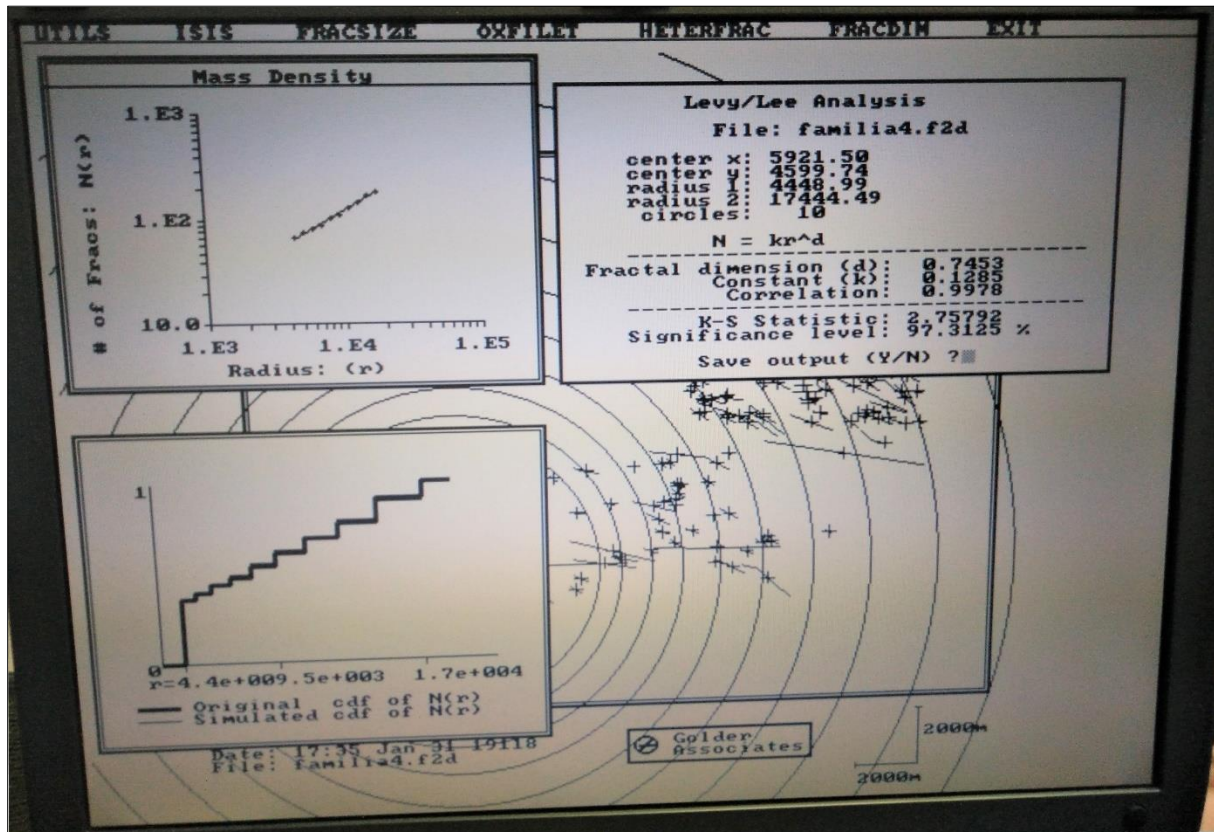


Figure 4.5.1. 1. Results of Spatial Analysis for Family 4 with FracMan1998.

The *Levy-Lee fractal model* requires derivation of a dimension D for the three-dimensional process of fracture centres from the two-dimensional pattern of fracture traces. La Pointe (2002, “Derivation of parent fracture population statistics from trace length measurements of fractal fracture populations”, *Int. J. Rock Mech. Min. Sci.*, Vol. 39, pp. 381-388) presents a derivation to convert the fractal mass dimension of points on a plane to the dimension of points in three-dimensional space required for fracture generation. This derivation indicates that the three-dimensional fractal process should be generated using a fractal dimension one greater than the dimension calculated for the two-dimensional trace plane.

For this reason, the value of the *Fractal Dimension* in two-dimensions that can be read from figure 4.5.1.1, $d = 0.7453$, has been added to 1 to obtain the fractal dimension in three-dimensions which is equal to $D = 1.7453$.

To be completed, the *Levy-Lee model* needs a second parameter, the *Minimum Step Size*. To calculate the *Minimum Step Size* one needs the model value of the distribution of minimum

distance between the centre of one fracture and its next closest fracture centre (Figure 4.5.1.2.). It resulted on the order of 300 meters. This parameter will have to be checked because it will be fundamental for the realization of the model.

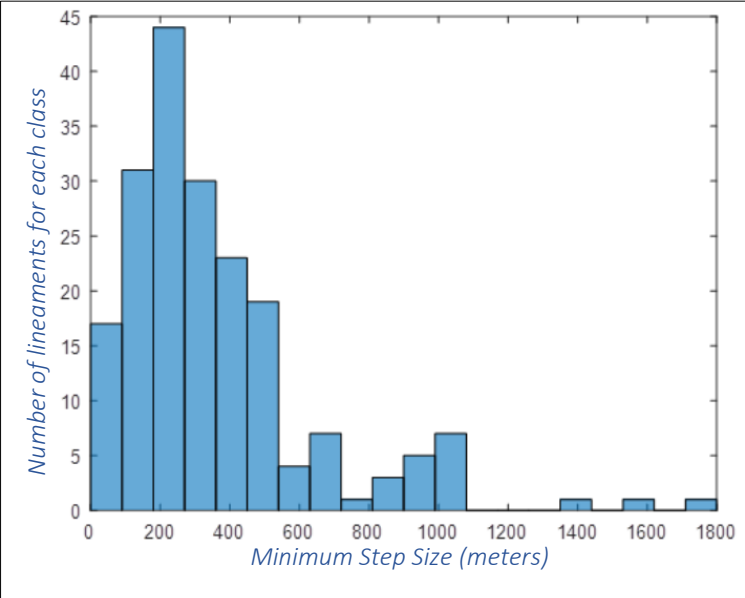


Figure 4.5.1. 2. Distribution of the Minimum Step Distance of Family 1 on a total number of 195 fractures.

4.5.2. Global fracture intensity P_{32}

Table 4.5.2.1. shows the parameters for the first approximation of the P_{32} for Family 4.

k	ρ	$1/C_{32}$	C_{32}	$P_{21} [L^{-1}]$	$P_{32} [L^{-1}]$
40	55	0.82	1.22	0.0008261	0.0010078

Table 4.5.2. 1. Parameters for the first approximation of the P_{32} calculation for Family 4.

4.5.3. Fracture orientation

The median of directions of this group of fractures is N110E.

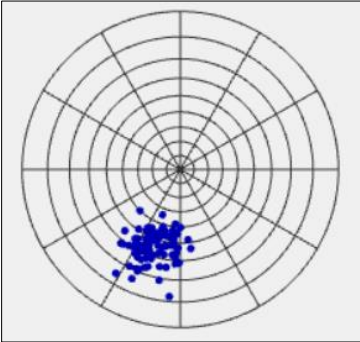


Figure 4.5.3. 1. Fisher distribution for Family 4 with stereographic representation (FracMan7).

4.5.4. Fracture size

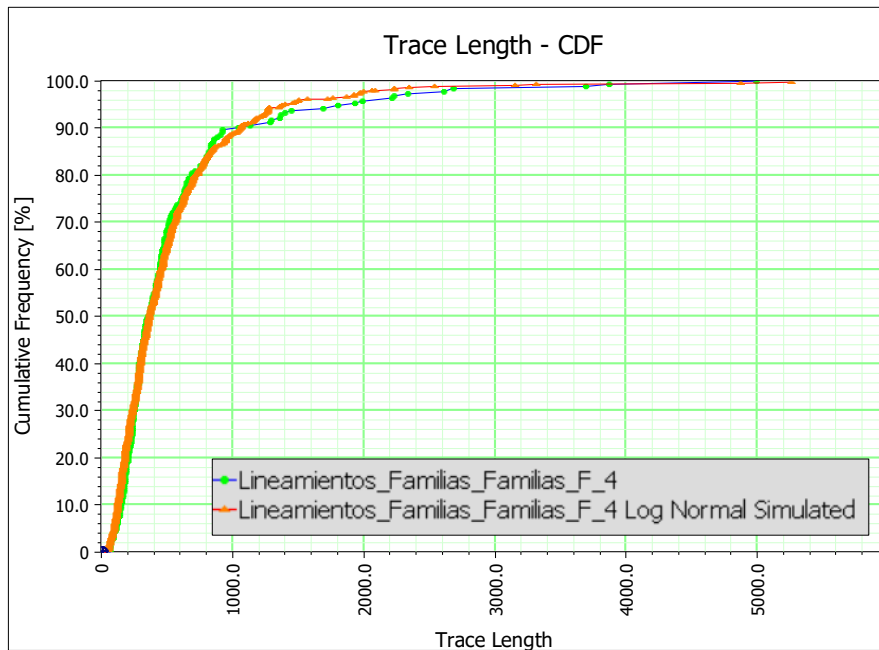


Figure 4.5.4. 1. Best fit of Lognormal distribution for Family 4 (Trace Length expressed in meters).

<i>Lineamientos_Familias_Familias_F_4</i>	
Trace Len Mean	558.238
Trace Len Dev	653.171
Radius Mean	162.128
Radius Deviation	177.01
Sim. Trace Len Mean	516.128
Sim. Trace Len Dev	530.806
K-S Test	0.0564103
Significance	0.907626

Table 4.5.4. 1. Results of Lognormal simulation fit (Family 4).

The values necessary for the *Fracture Size* to execute the simulation are the mean and the standard deviation of the equivalent radius, respectively 162.13 and 177.01.

4.5.5. Termination probability

The termination probability of Family 4 calculated is $P_T = 0$.

4.6. Family 5

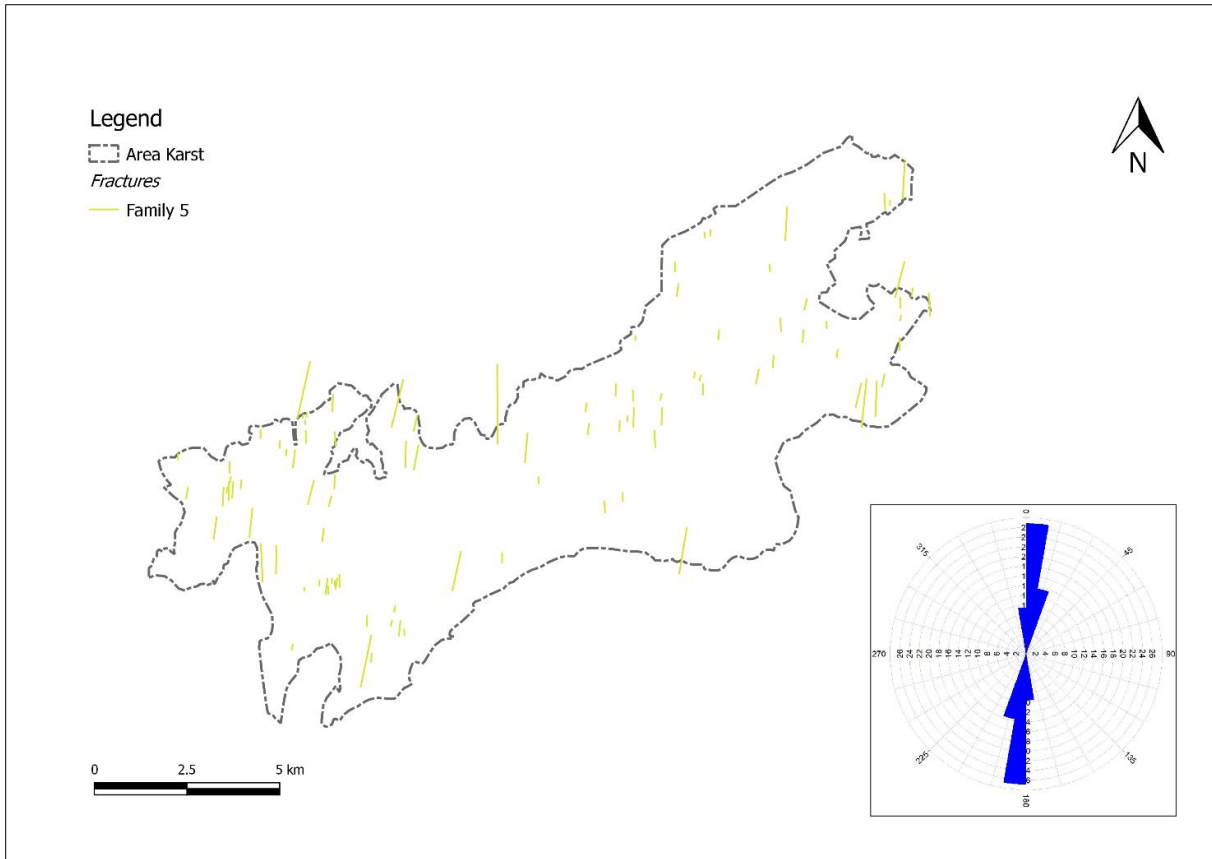


Figure 4.6. 1. Lineaments and rose diagram of Family 5.

There are 97 lineaments placed in Family 5, direction N5W-N15E and the tectonic origin may be associated with the Pliocenic Age and the Ancient Quaternary Age. Also in this case, the fractures of Family 5 granted a good development of karst.

In the following figure the histogram of lengths with its statistical summary is shown.

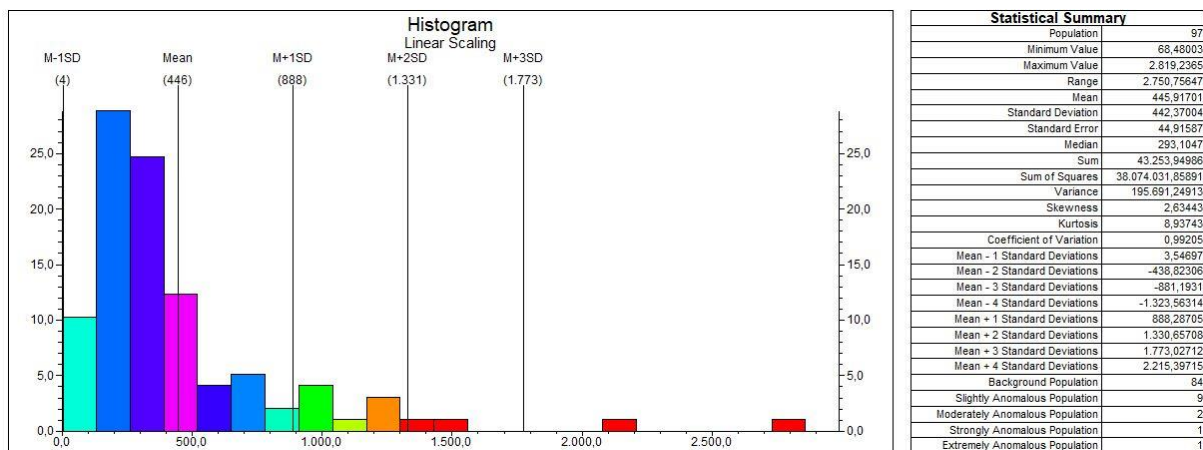


Figure 4.6. 2. Lengths histogram expressed in meters (bin = 130 m, the relative percentage is shown on the ordinates) and its statistical summary of Family 5 (RockWorks2016).

4.6.1. Generation model

For Family 5 it was decided to use the *The Baecher model*.

4.6.2. Global fracture intensity P_{32}

Table 4.6.2.1. shows the parameters for the first approximation of the P_{32} for Family 5.

k	ρ	$1/C_{32}$	C_{32}	$P_{21} [L^{-1}]$	$P_{32} [L^{-1}]$
200	85	0.99	1.01	0.0002777	0.0002805

Table 4.6.2. 1. Parameters for the first approximation of the P_{32} calculation for Family 5.

4.6.3. Fracture orientation

The median of directions of this family is N5E.

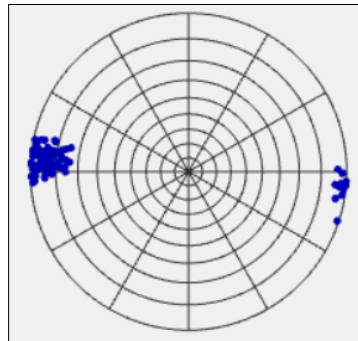


Figure 4.6.3. 1. Fisher distribution for Family 5 with stereographic representation (FracMan7).

4.6.4. Fracture size

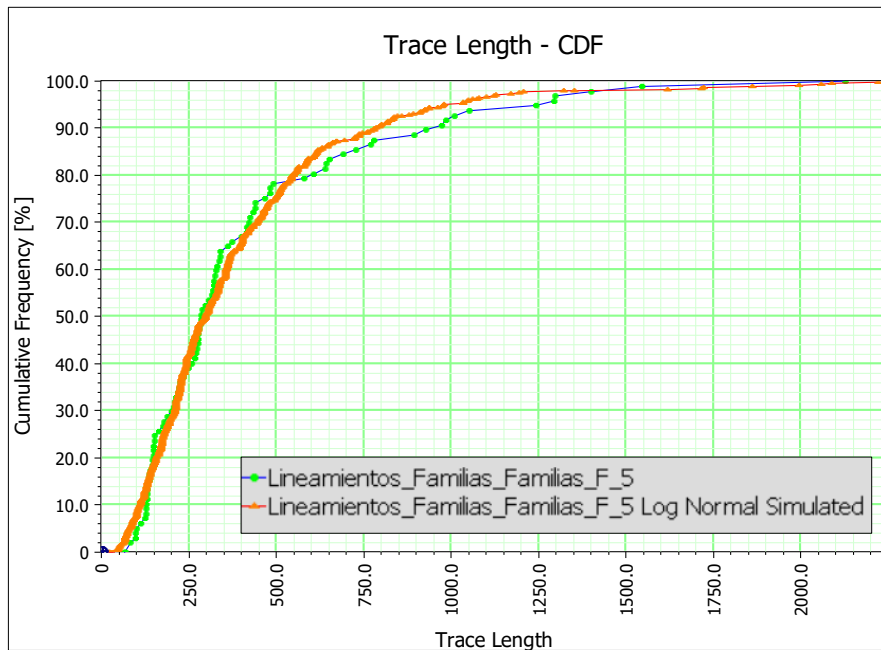


Figure 4.6.4. 1. Best fit of Lognormal distribution for Family 5 (Trace Length expressed in meters).

<i>Lineamientos_Familias_Familias_F_5</i>	
Trace Len Mean	413.86
Trace Len Dev	366.745
Radius Mean	159.427
Radius Deviation	128.753
Sim. Trace Len Mean	384.493
Sim. Trace Len Dev	316.334
K-S Test	0.0618557
Significance	0.990482

Table 4.6.4. 1. Results of Lognormal simulation fit (Family 5).

The values necessary for the *Fracture Size* to execute the simulation are the mean and the standard deviation of the equivalent radius, respectively 159.43 and 128.75.

4.6.5. Termination probability

The termination probability of Family 5 calculated is $P_T = 0$.

4.7. Summary of the parameters to be included in the model

Table 4.7.1. Summary of all parameters required for the model.

Generation model														
Family 1			Family 2			Family 3			Family 4			Family 5		
<i>The Baecher model</i>			<i>The Baecher model</i>			<i>The Baecher model</i>			<i>Levy-Lee model (*)</i>			<i>The Baecher model</i>		

$P_{32} [L^{-1}]$														
Family 1			Family 2			Family 3			Family 4			Family 5		
0.000789155			0.000843753			0.000522114			0.001007797			0.000280472		

Fracture orientation														
Family 1			Family 2			Family 3			Family 4			Family 5		
<i>Fisher distribution</i>			<i>Fisher distribution</i>			<i>Fisher distribution</i>			<i>Fisher distribution</i>			<i>Fisher distribution</i>		
$\alpha^{(**)}$	90- ρ	k												
157.5	-20	65	245	5	50	122.5	5	65	200	35	40	275	5	200

Fracture size (equivalent radius)										
Family 1		Family 2		Family 3		Family 4		Family 5		
<i>Log Normal distribution</i>		<i>Log Normal distribution</i>		<i>Log Normal distribution</i>		<i>Log Normal distribution</i>		<i>Log Normal distribution</i>		
Mean	Dev	Mean	Dev	Mean	Dev	Mean	Dev	Mean	Dev	
146.92	211.95	177.77	156.71	121.48	170.92	162.13	177.01	159.43	128.75	

Probability Termination P_T				
Family 1	Family 2	Family 3	Family 4	Family 5
0.71	0	0	0	0

Finally, for all the simulations 20 was inserted as the *Number of Sides* in the *Fracture Shape*.

(*) For the *Levy-Lee model* of Family 4, the following parameters are required:

- Fractal dimension (three-dimensions), $D = 1.7453$
- Minimum Step Size $\sim 300 \text{ m}$

(**) $\alpha \rightarrow$ see chapter 4.3.2.

5. 3D Discrete Fracture Model Creation

5.1. Simplified Model

To realize the model, after calculating all the necessary parameters described in the previous chapter, a first provisional model was created with a simplified volume (parallelepiped). This volume is equal to $72 \cdot 10^9 \text{ m}^3$. The attributes of coordinates, inclination and lengths are shown in Table 5.1. The value of depth z was chosen according to the geological section reported in the paper by Carolina Guardiola-Albert et al. (*Comparison of Recharge Estimation Methods During a Wet Period in a Karst Aquifer*. 2015). This section is shown in Figure 5.1.2.

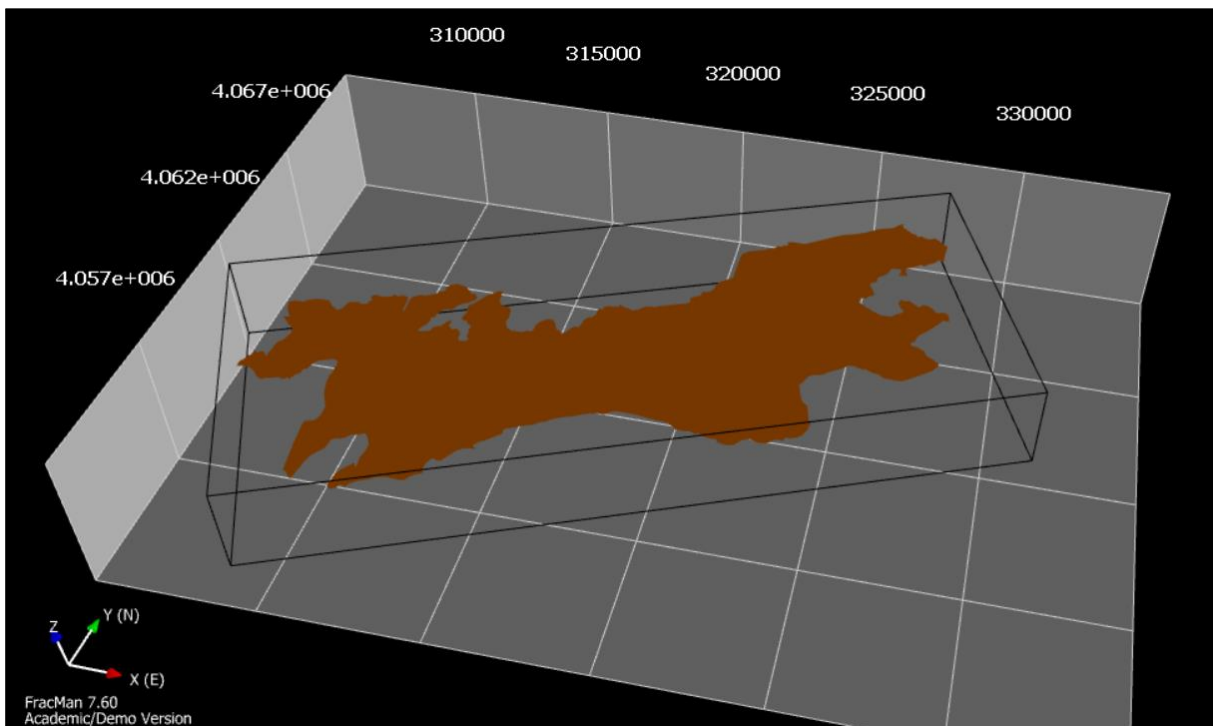


Figure 5.1. 1. Representation of the volume (parallelepiped) used for the creation of the simplified model. (FracMan7)

Center [m]	
X	318500
Y	4061600
Z	0
Scan	
Trend	67
Plunge	0
Length	24000
Transverse	
Trend	337
Plunge	0
Length	10000
Height	
Trend	180
Plunge	-89.3541
Length	3000

Table 5.1. 1. Attributes for simplified volume

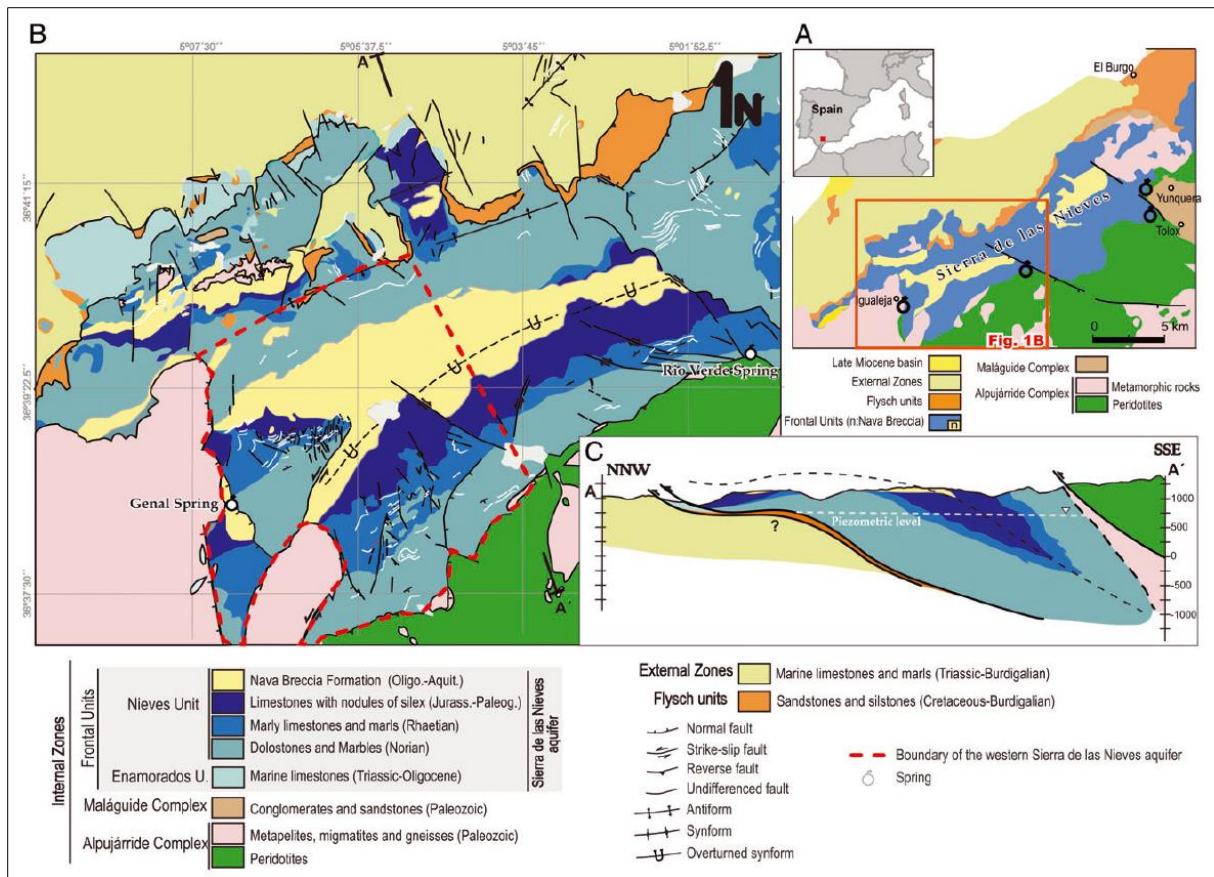


Figure 5.1. 2. Location and hydrogeological map of the study area (modified from Liñan 2003). (A) General location, (B) hydrogeological map, and (C) geological cross-section. (Carolina Guardiola-Albert et al., 2015)

The provisional model is necessary for a first validation of some of the parameters chosen for the realization of the definitive model. In this chapter the work carried out on the provisional model of Family 1 will be presented in a more accurate way to understand the procedures performed. In the end only the most significant results and parameters will be reported for the remaining families.

By inserting the parameters shown in Table 4.6.1, a first approximation of the model into the provisional volume was made (Figure 5.1.3). It should be emphasized that the result of the simulation was a manual iterative process, where, first, the author visually checked the result obtained before carrying out more in-depth analyses.

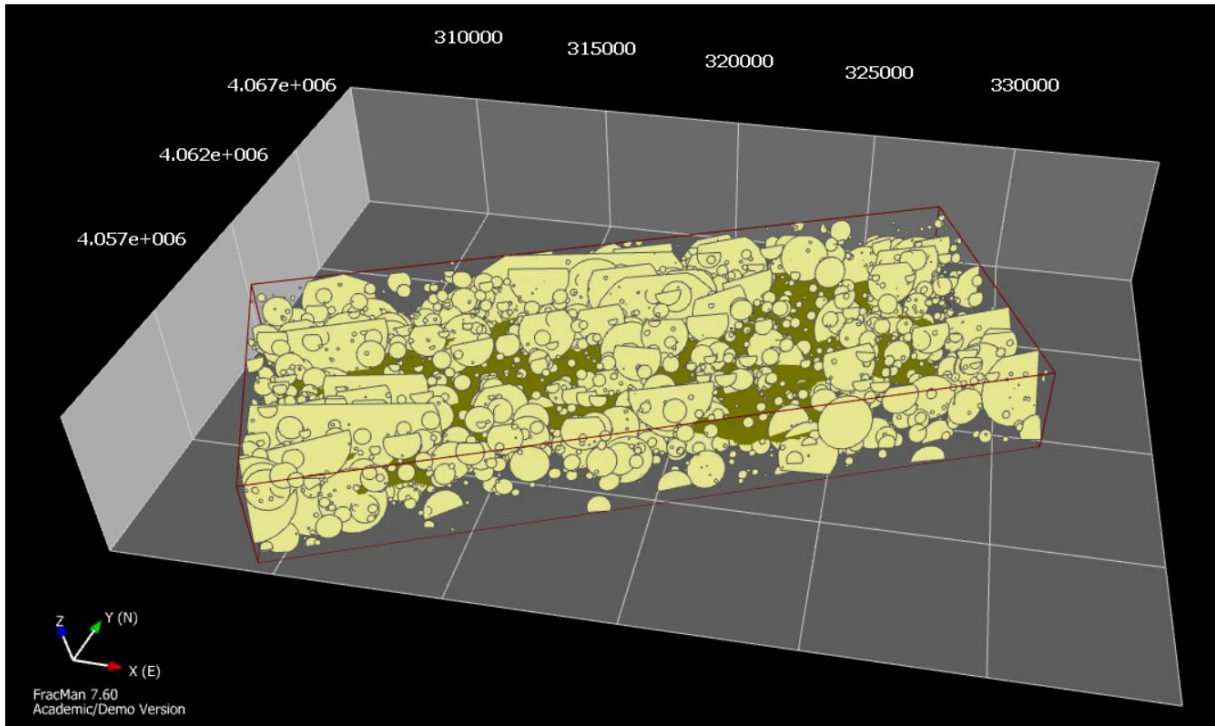


Figure 5.1. 3. Simplified 3D Discrete Fractures Model in a basic volume. (Family 1)

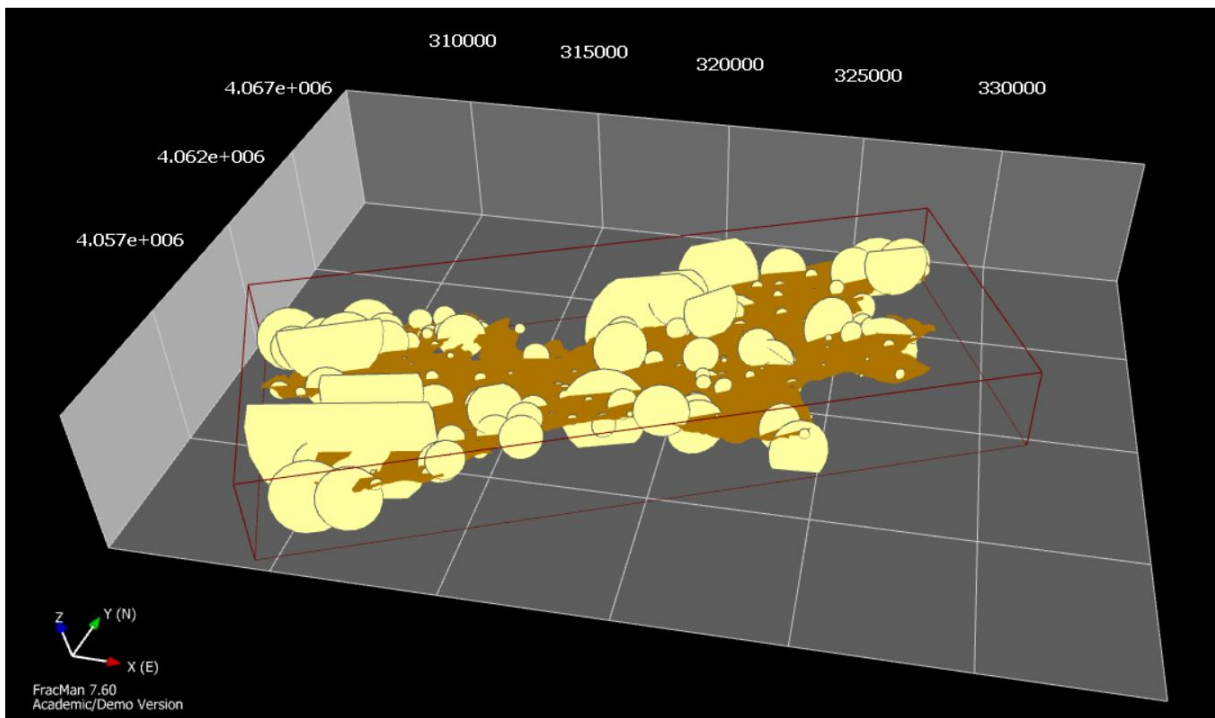


Figure 5.1. 4. Intersecting fractures of Simplified 3D Discrete Fractures Model (Family 1)

Once the first approximation of the model was made, the fractures that intersect the study area were analysed to verify if there was a correspondence with the data entered.

In Figure 5.1.4 the fractures that intersect the study area are shown in a 3D representation and in the following images (Figures 5.1.5 and 5.1.6) it is possible to see the difference between the real trace map and the simulated one (2D representation).

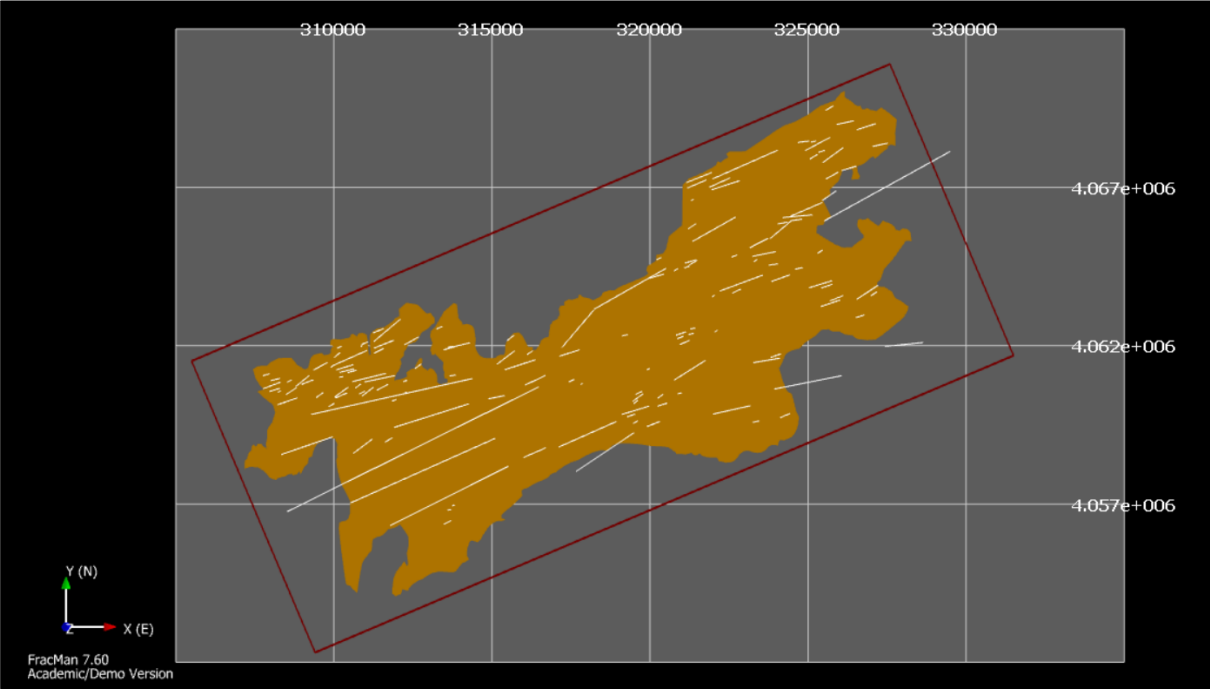


Figure 5.1. 5. Real trace map of Family 1.

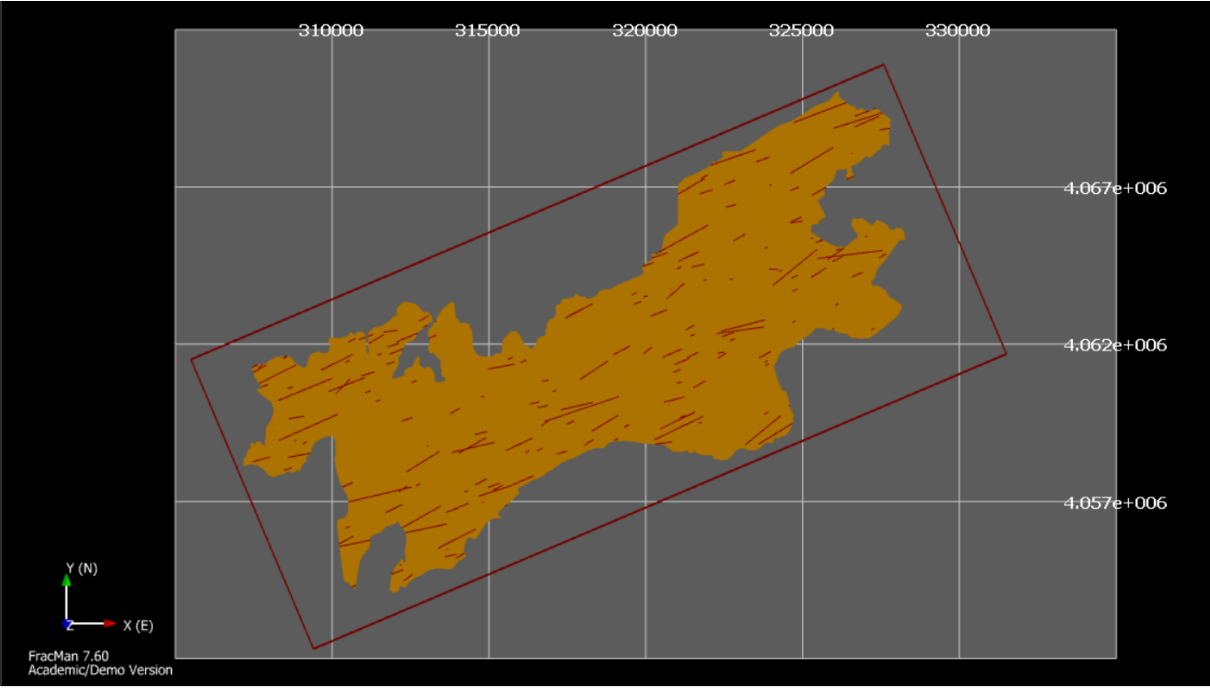


Figure 5.1. 6. Simulated intersecting fractures (lineaments, 2D) of Family 1.

The first verification analysis between the Figure 5.1.5 and 5.1.6 was visual. A second check was made by calculating the simulated P_{21} and comparing it with the P_{21} of the real lineaments. In the case in which the value of P_{21} between the real and the simulated trace maps was clearly different, new calculations of P_{32} were completed. The conversion factor C_{32} was based on these changes. Finally, the number of real lineaments was compared with the number of simulated ones for each family.

The compared values of the results of the simulations for each family is reported in the Table 5.1.2.

Family	Initial parameters (real)		Simulated parameters	
	P_{21}	Trace number	P_{21}	Trace number
1	0.0007445	147	0.0007456	188
2	0.0008354	233	0.0008484	264
3	0.0005170	137	0.0006196	159
4	0.0008261	195	0.0007977	217
5	0.0002777	97	0.0002706	94

Table 5.1. 2. Comparison between real and simulated P_{21} and trace number.

The results obtained are all satisfactory, except with the case of Family 3, where the value of P_{21} changes considerably between the initial and the simulated trace maps. For this reason, an additional iteration took place for changing the parameter P_{32} to be included in the model. After various simulations it was decided to use the new P_{32} equal to 0.00051, which gave the following results:

- $P_{21} = 0.0005142$
- Trace number = 152

There are no substantial differences between the values of real and simulated P_{21} . As regards the number of lineaments, generally some families have a greater number in the simulation than the reality. As can be seen in the length histograms given in chapter 4, this difference can be given by the fact, that there are some very large fractures, except in the case of Family 5.

These values, within the length distribution functions, have a probability so low that in most cases in the simulations do not appear. For this reason, to obtain a value of P_{21} that is as close as possible to the real one, in the absence of large fractures, FracMan7 created more fractures to achieve the desired intensity. In this case, this difference in the trace number was considered acceptable.

5.2. 3D Discrete Fracture Model

Once the parameters have been chosen (see chapter 4.6) and verified in the simplified model described in the previous chapter, a volume that is as close as possible to reality was created. Then, as in the case of the simplified model, the model was implemented for each family.

5.2.1. Volume

For the realization of the complete model, a volume that is more approximate to the actual geological formation of karst was created. To do this, two surfaces, lower and upper, were formed. The simulation was carried out in the volume interposed between these two areas. As shown in the section in Figure 5.1.2.C, the geological section of the study area presents a syncline, with a power of about 2000 meters. In the most northeaster part of the study area the power is higher than 3000 meters, due to the presence of Pico Torrecilla (1919 m). For this reason, a lower surface has been created with an inclination similar to that of the section. Subsequently, the Turquillas fault, which almost bisects the study area, was taken into consideration by the literature of the study area (see Figure 3.3.a). It was decided then to divide the lower surface into two and to lower the western part of 250 meters and to raise the eastern part by another 250 meters to obtain a simplified physical vision of reality (Figures 5.2.1.1 and 5.2.1.2).

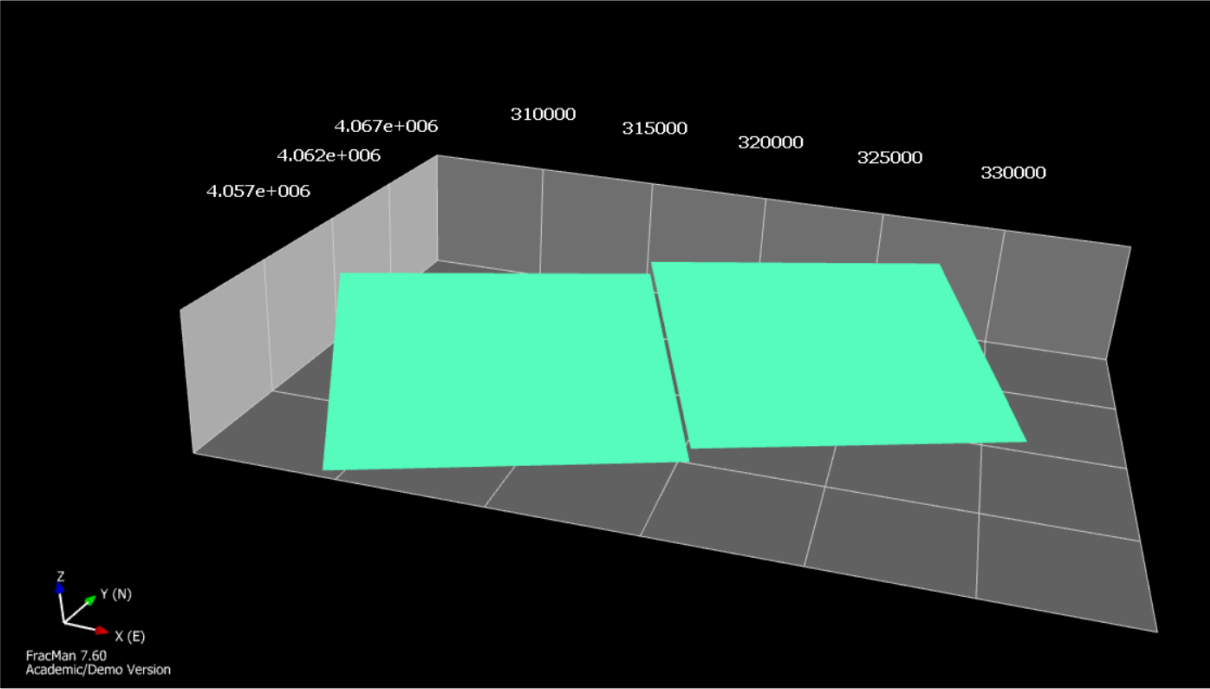


Figure 5.2.1. 1. Lower surface for the calculation of the new volume.

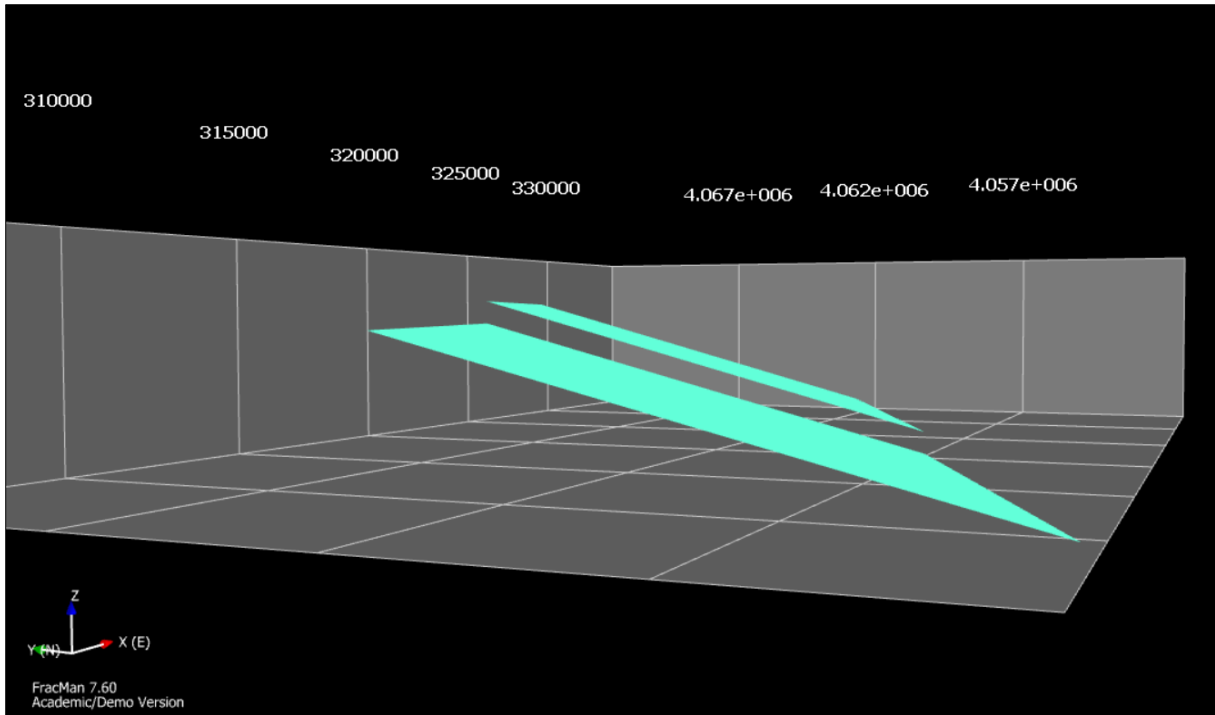


Figure 5.2.1. 2. Lower surface for volume calculation. Perpendicular view of the analysed section (Figure 5.1.2.C).

As regards the upper surface, the Digital Terrain Model (DTM) of the study area with a resolution of 100 meters was used. (Figure 5.2.1.3)

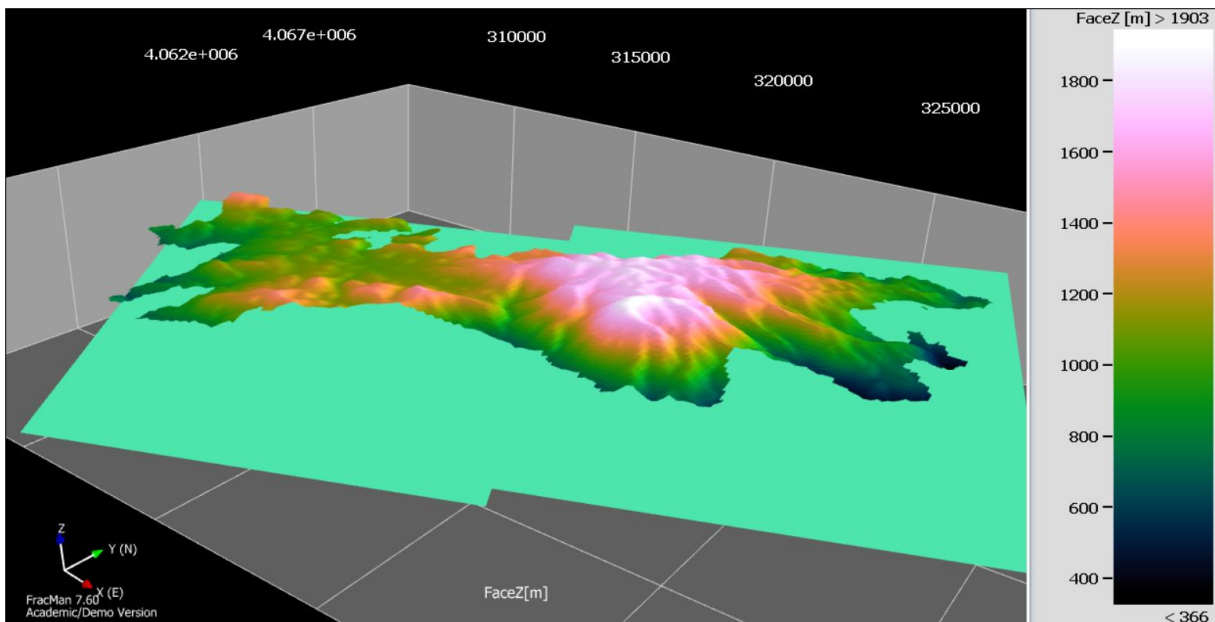


Figure 5.2.1. 3. Upper surface for volume calculation. DTM with resolution = 100 m.

5.2.2. Family 1

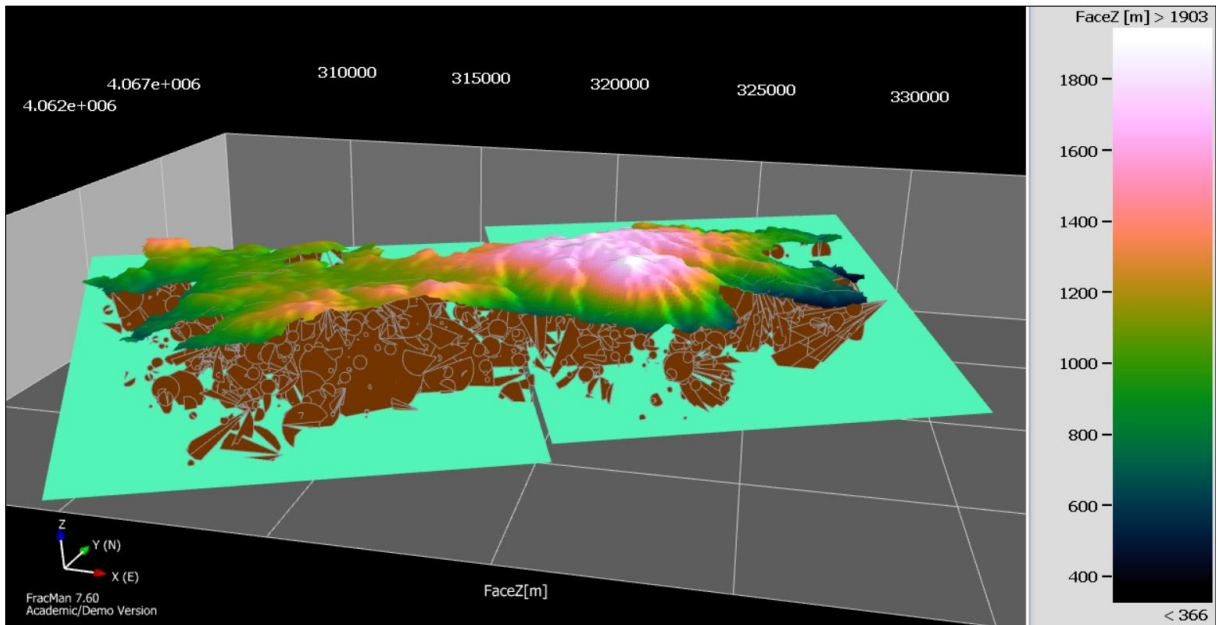


Figure 5.2.2. 1. 3D Discrete Fracture Model for Family 1.

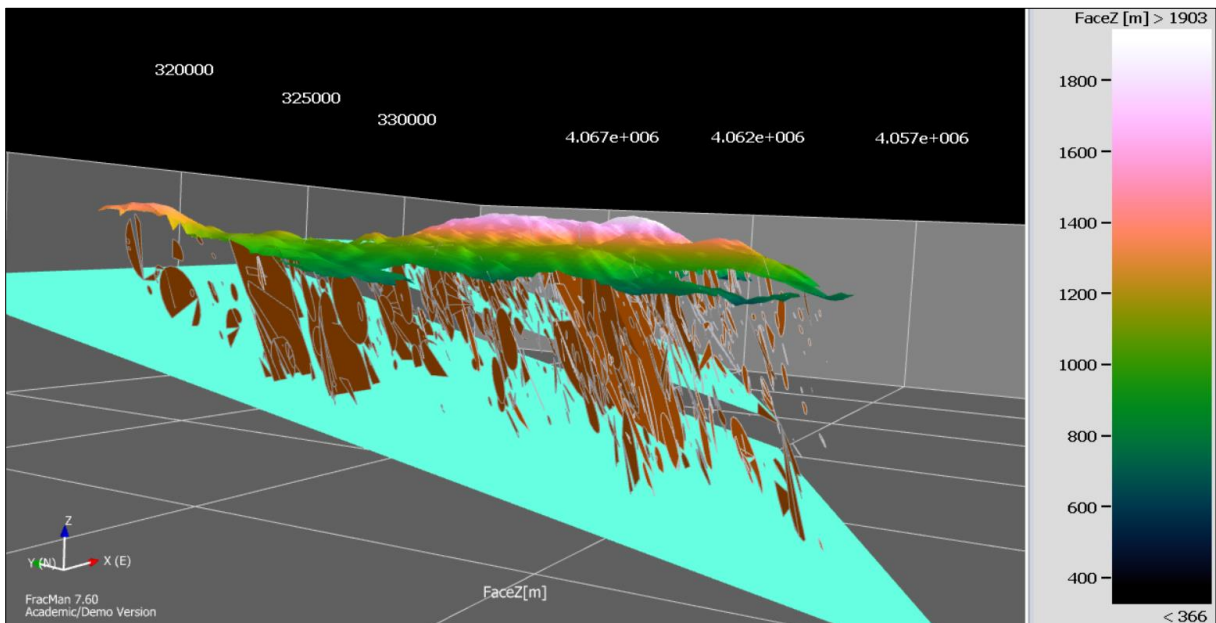


Figure 5.2.2. 2. 3D Discrete Fracture Model for Family 1.

5.2.3. Family 2

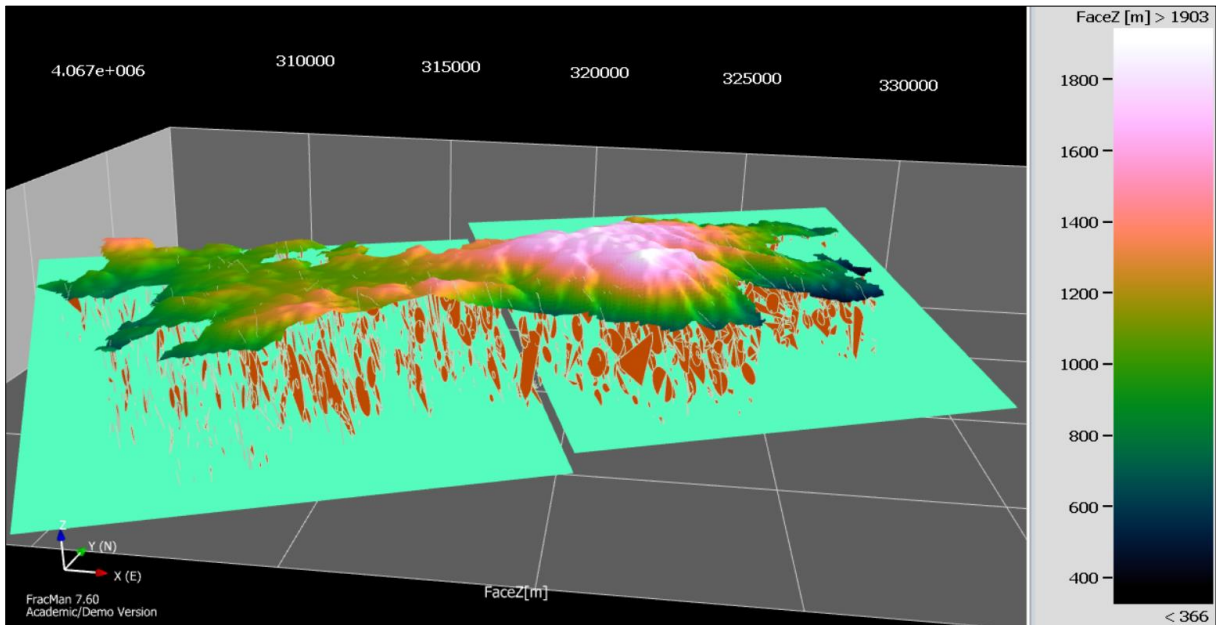


Figure 5.2.3. 1. 3D Discrete Fracture Model for Family 2.

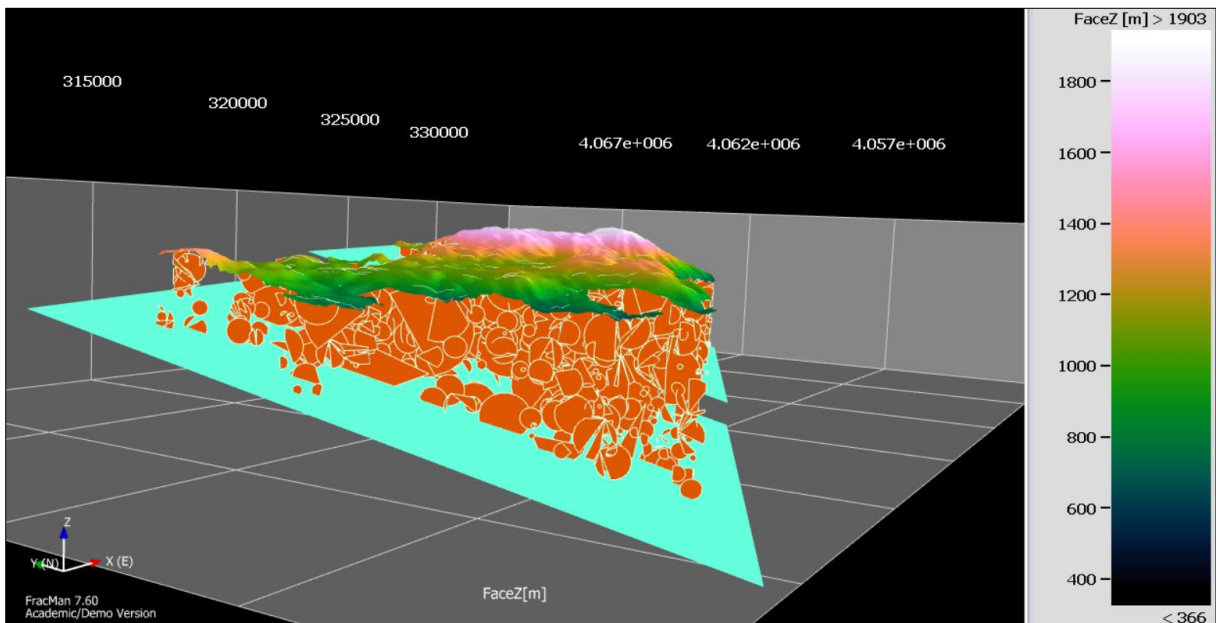


Figure 5.2.3. 2. 3D Discrete Fracture Model for Family 2.

5.2.4. Family 3

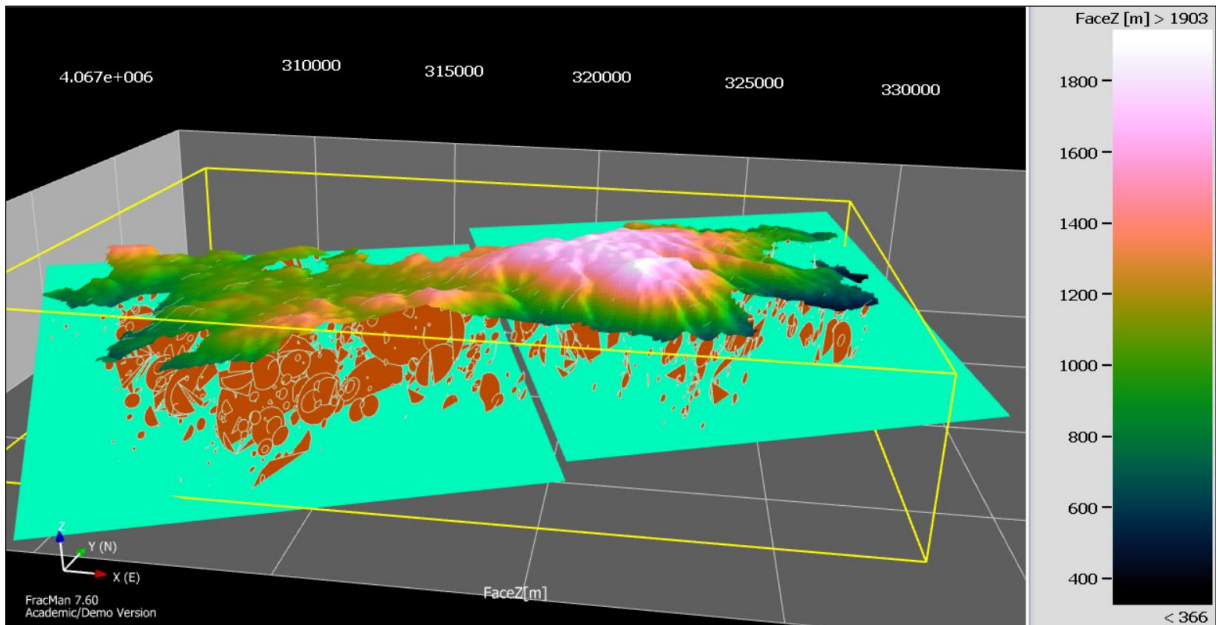


Figure 5.2.4. 1. 3D Discrete Fracture Model for Family 3.

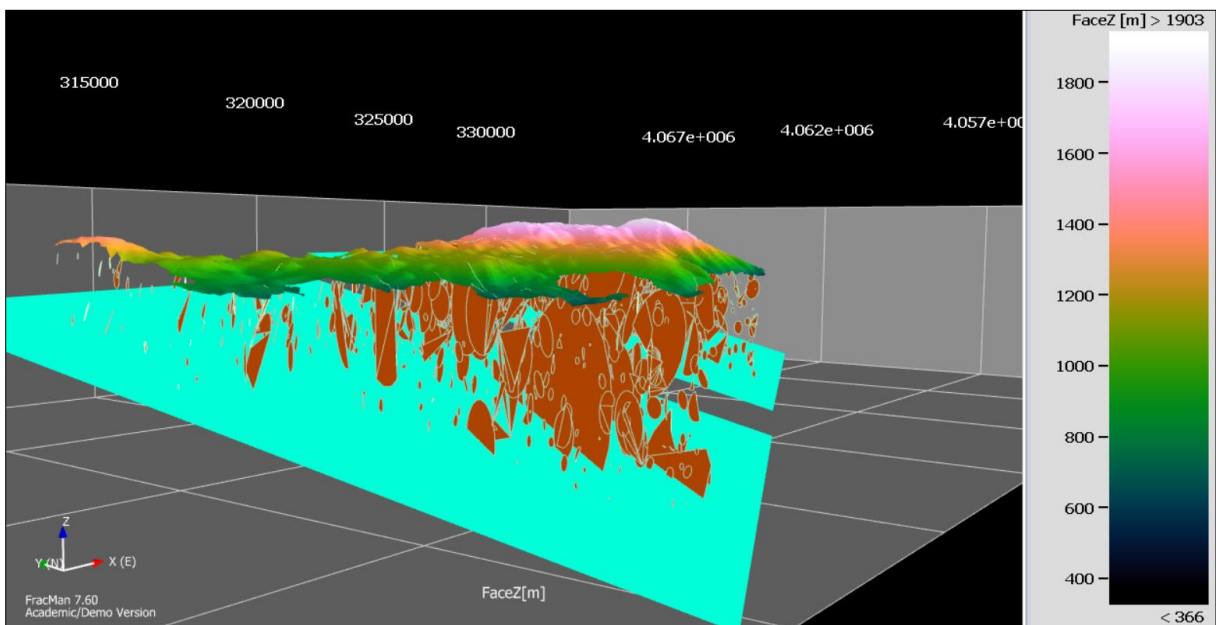


Figure 5.2.4. 2. 3D Discrete Fracture Model for Family 3.

5.2.5. Family 4

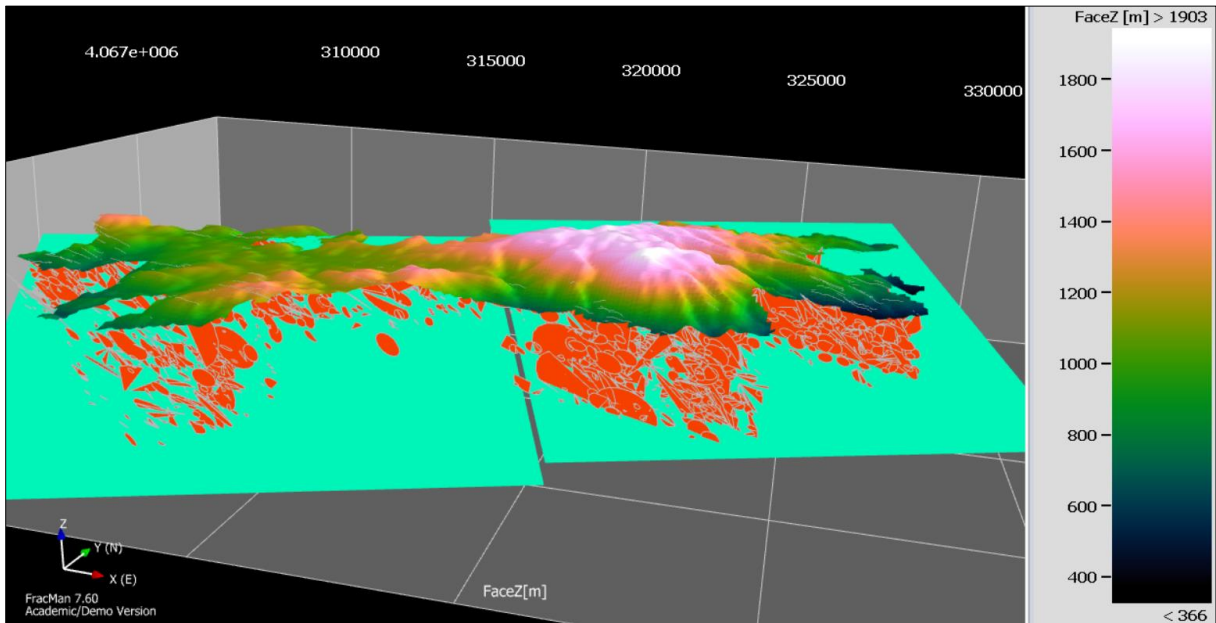


Figure 5.2.5. 1. 3D Discrete Fracture Model for Family 4.

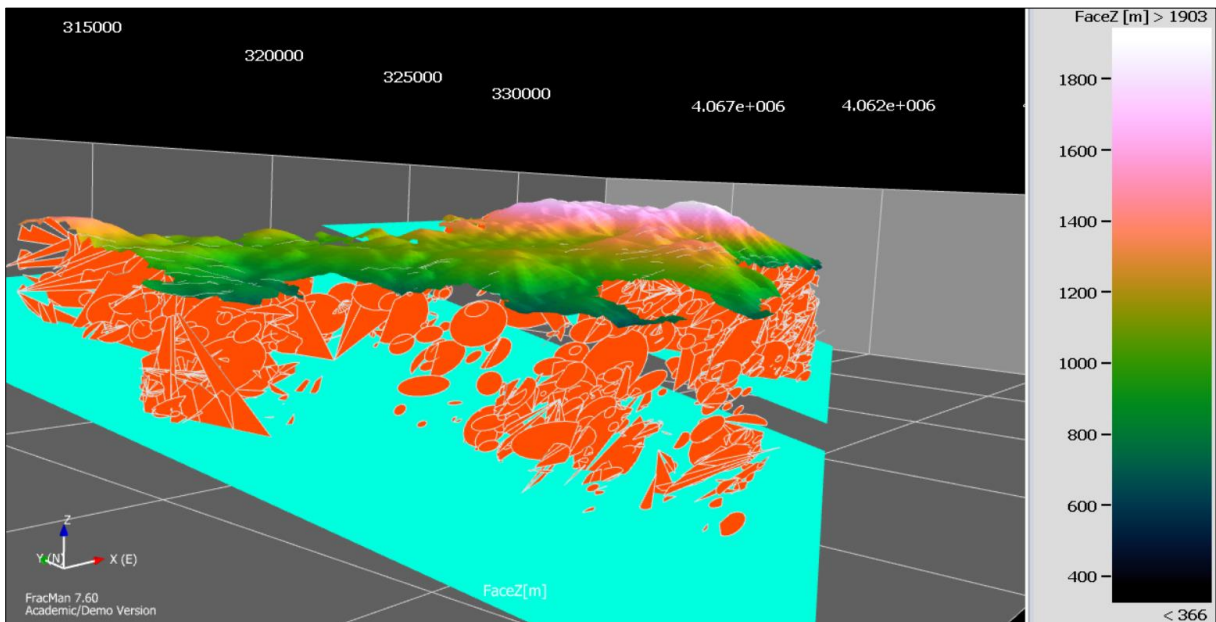


Figure 5.2.5. 2. 3D Discrete Fracture Model for Family 4.

5.2.6. Family 5

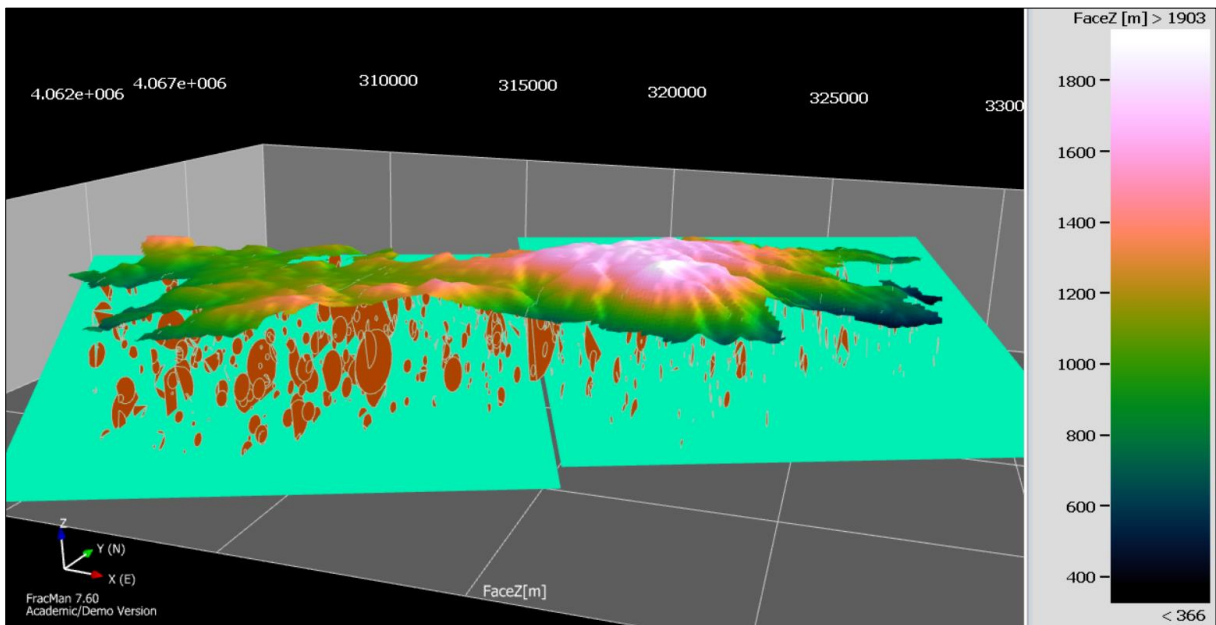


Figure 5.2.6. 1. 3D Discrete Fracture Model for Family 5.

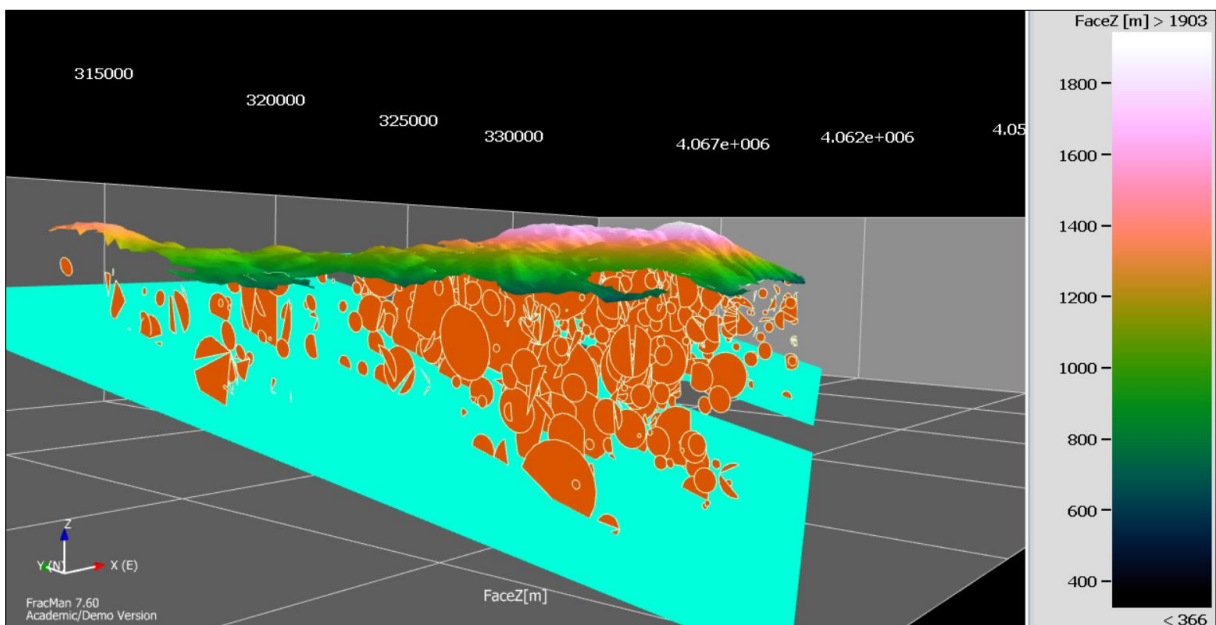


Figure 5.2.6. 2. 3D Discrete Fracture Model for Family 5.

5.2.7. Completed Fracture Model

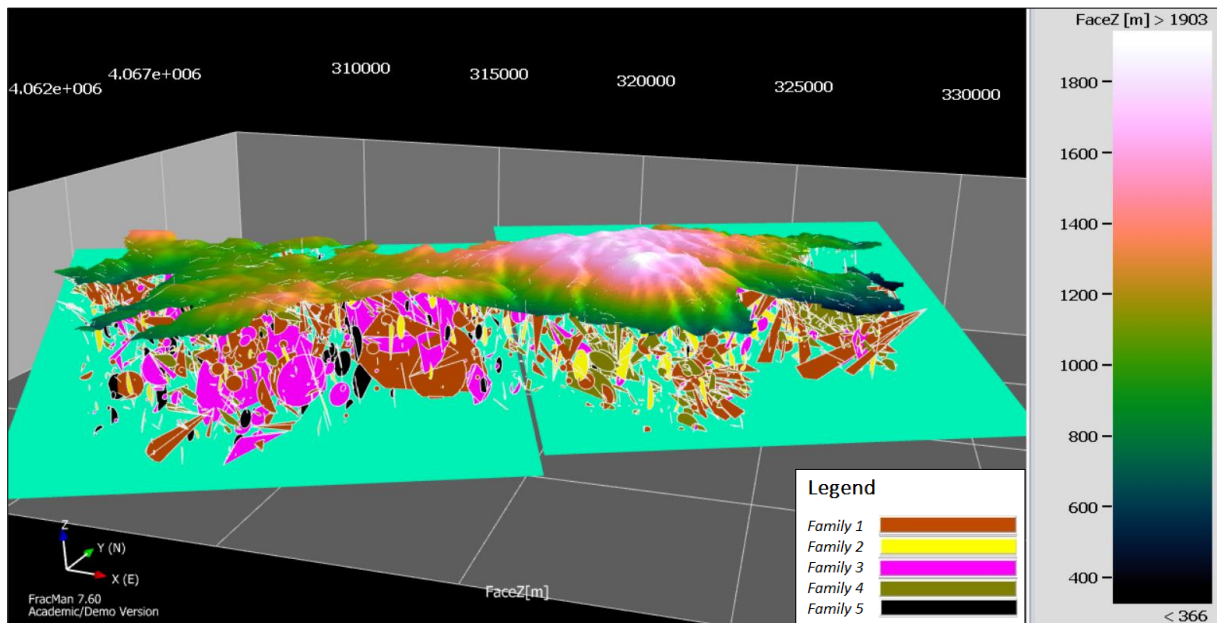


Figure 5.2.7. 1. Completed 3D Discrete Fracture Model. Percentage of fractures displayed = 30%.

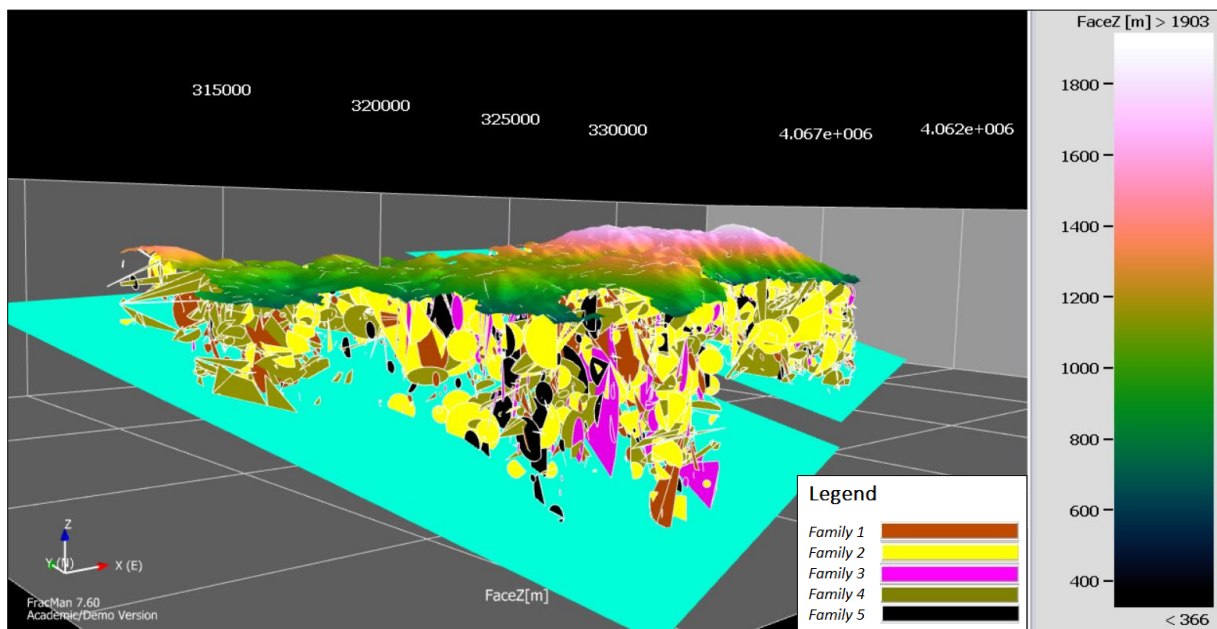


Figure 5.2.7. 2. Completed 3D Discrete Fracture Model. Percentage of fractures displayed = 30%.

6. Model Validation

To validate the model, some significant data were compared between the real ones and those of the created fracture model. In this case the analysis was initially carried out for each family, and finally on the complete model. The data compared for the validation of the fracture model are the following:

- P_{21}
- Visual Comparison
- Comparison Length Histograms
- Stereonet (stereographic projection) and Rose Diagram of fractures

Regarding the first three points, two-dimensional data, a surface of the study area at a height of 600 m above sea level was realized. This decision is due to the fact that, considering the volume described in chapter 5.2.1, the 600 m height study area is the area that most intersects the fractures obtained in the model with the indicated volume. This did not pose a problem in the case of the simplified model, because the study area was completely within the simplified volume, at a height of 0 m above sea level. Therefore, it did not create problems for the verification of the parameters to be analysed.

In the following image (Figure 6.1) it is possible to see the lower and upper surfaces that delimit the simulation volume and the study area (600 m above sea level). This surface was used for the calculation of some parameters necessary for the validation of the model.

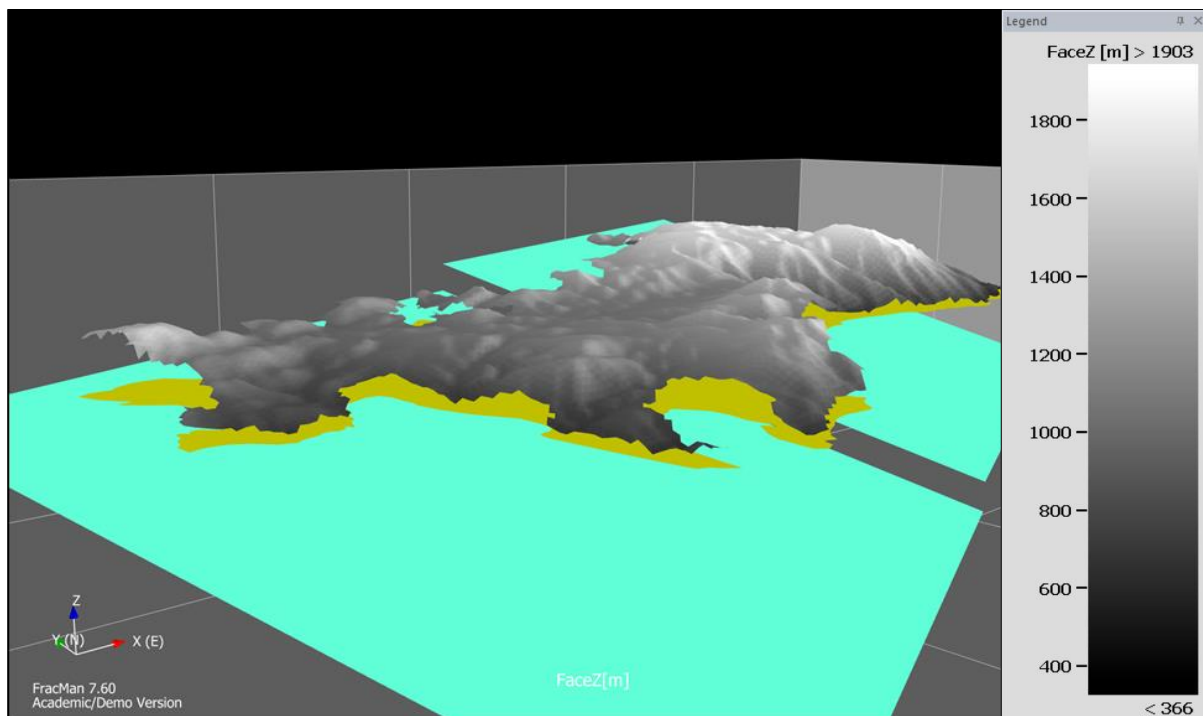


Figure 6. 1. Lower and upper surfaces that delimit the simulation volume and study area (600 m above sea level) for the calculation of some parameters necessary for model validation.

Once the surface was intersected with the fractures created by the model, the first three points were analysed. A three-dimensional example of the simulated fractures that intersect the study area (600m) is shown in Figure 6.2.

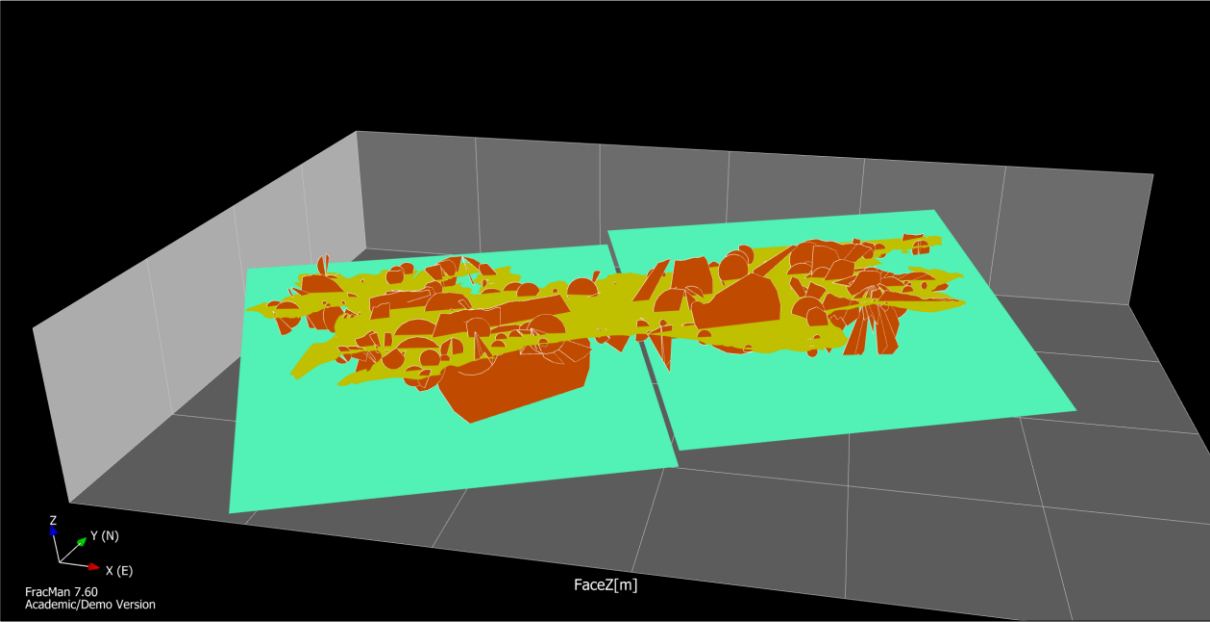


Figure 6. 2. Example of the simulated fractures that intersect the study area (600 m) of Family 1.

6.1. P₂₁

Family	Real P ₂₁	Simulated P ₂₁	Percentage error (%)
1	0.0007445	0.0007442	0.03
2	0.0008354	0.0008895	6.48
3	0.0005170	0.0005123	0.90
4	0.0008261	0.0008269	0.10
5	0.0002777	0.0002780	0.13
Total	0.0031919	0.0032501	1.82

Table 6.1. 1. Real and simulated P₂₁ and percentage error.

The values of P₂₁ are widely acceptable for families 1, 3, 4 and 5 where the percentage error does not exceed 1%. However, for family 2, the error obtained is equal to 6.48%. It was decided to consider this error acceptable, because the values of the P₂₁ analysed here refer only to the fractures that intersect the study area (600 m). Therefore, they are values that change a lot depending on the altitude. The total error of the sum of all fractures is 1.82%, acceptable and obviously influenced by a high error value of P₂₁ for the family 2.

6.2. Visual Comparison

After analysing the P_{2l} values, all the maps obtained from the intersection of the 3D Discrete Fracture Model with the study area (600 m) were visually compared.

6.2.1. Family 1

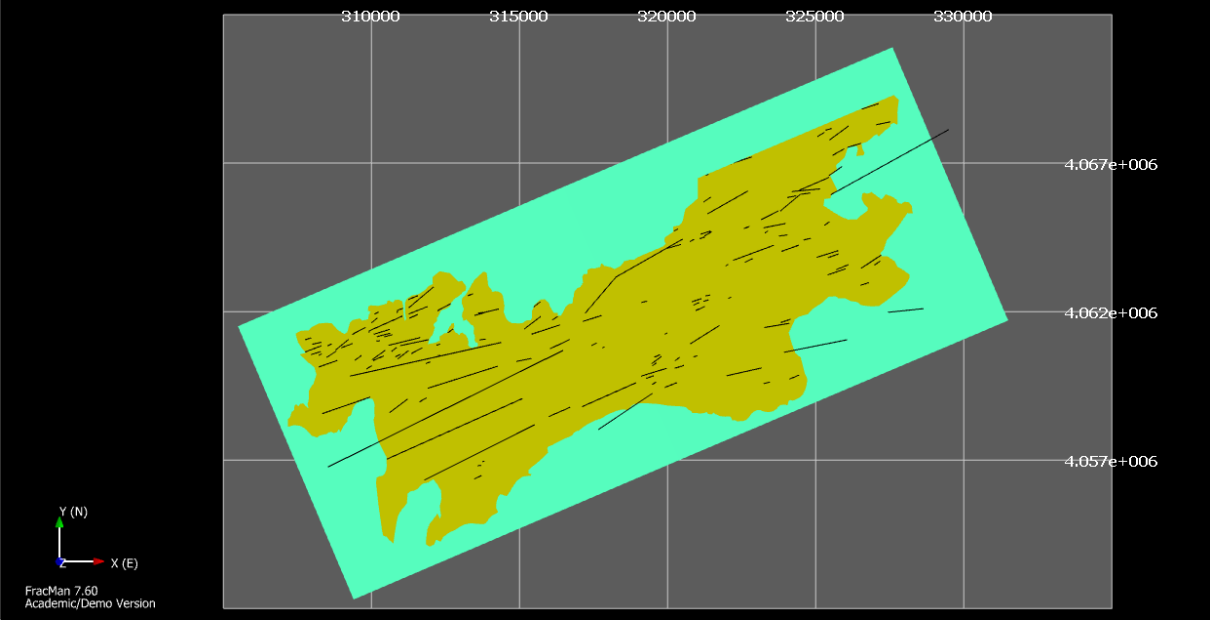


Figure 6.2.1. 1. Real trace map of Family 1.

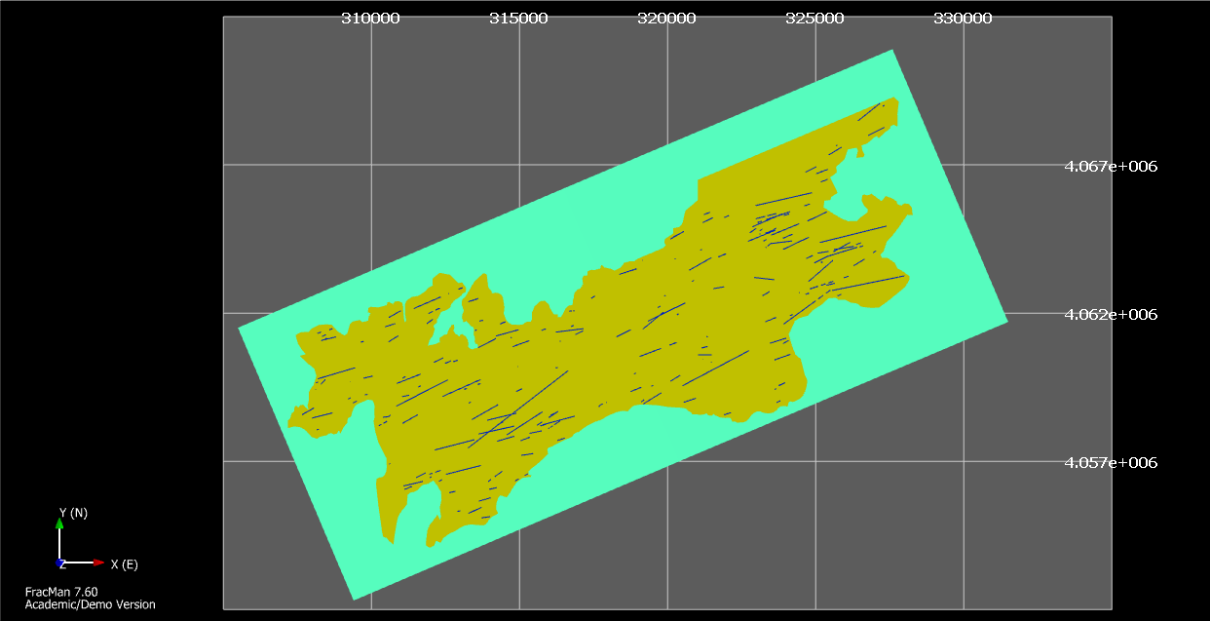


Figure 6.2.1. 2. Simulated trace map of Family 1, obtained from the intersection of simulated fractures with study area (600m).

6.2.2. Family 2

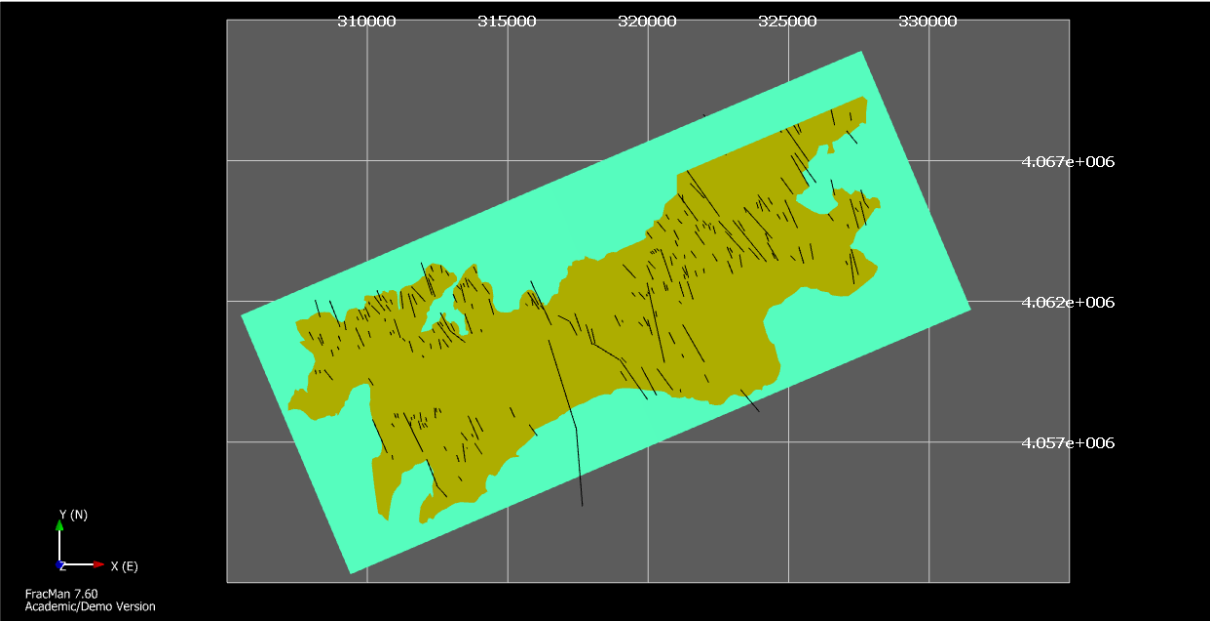


Figure 6.2.2. 1. Real trace map of Family 2.

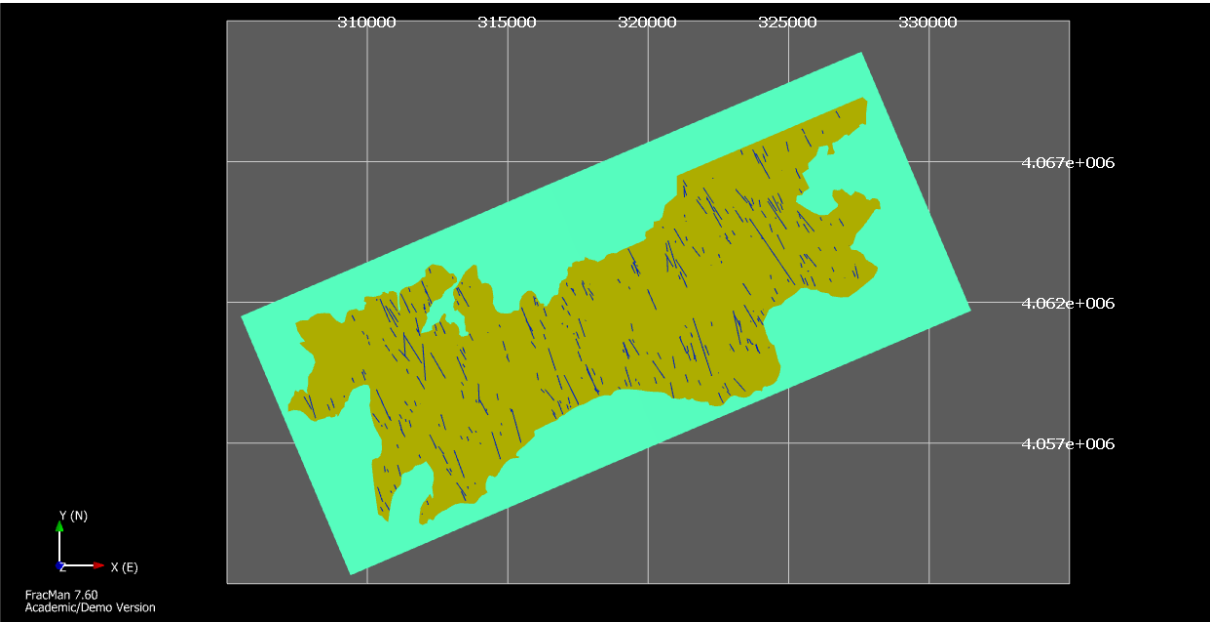


Figure 6.2.2. 2. Simulated trace map of Family 2, obtained from the intersection of simulated fractures with study area (600m).

From the visual comparison carried out for Family 2, it can be seen that the simulated trace map do not correspond optimally neither for length nor for distribution to real trace map. Presumably it would have been better to use another type of model, probably *The Levy-Lee Model*, even if the analysis carried out by FracMan1998 gave *The Baecher Model* (4.3.1) as the best result.

6.2.3. Family 3

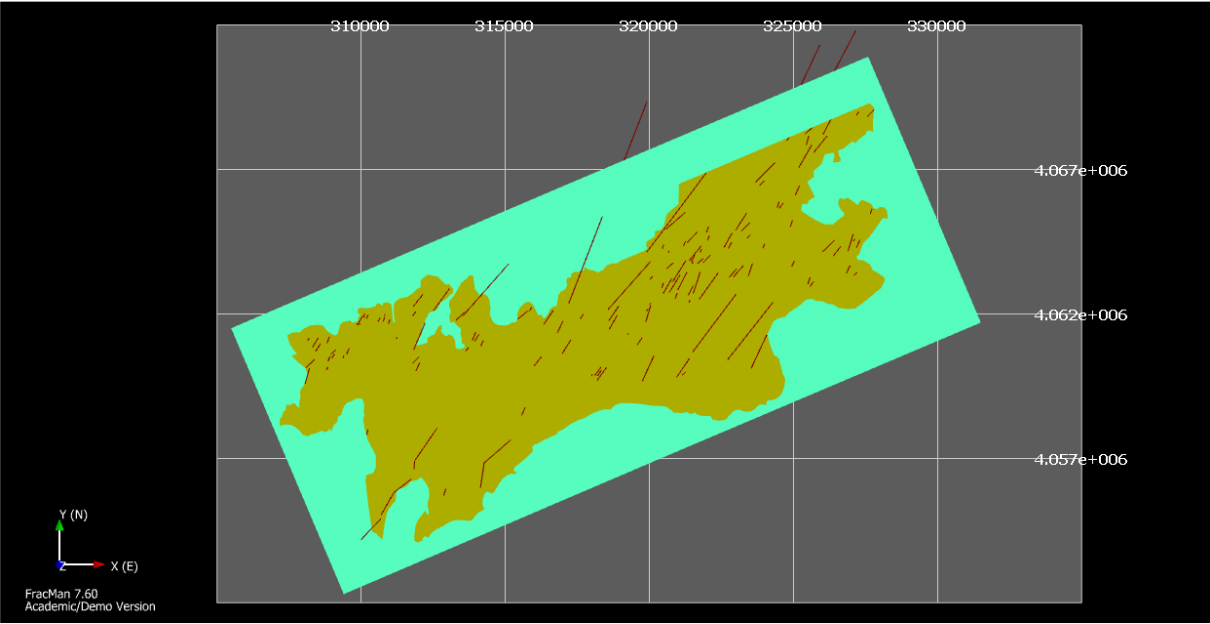


Figure 6.2.3. 1. Real trace map of Family 3.

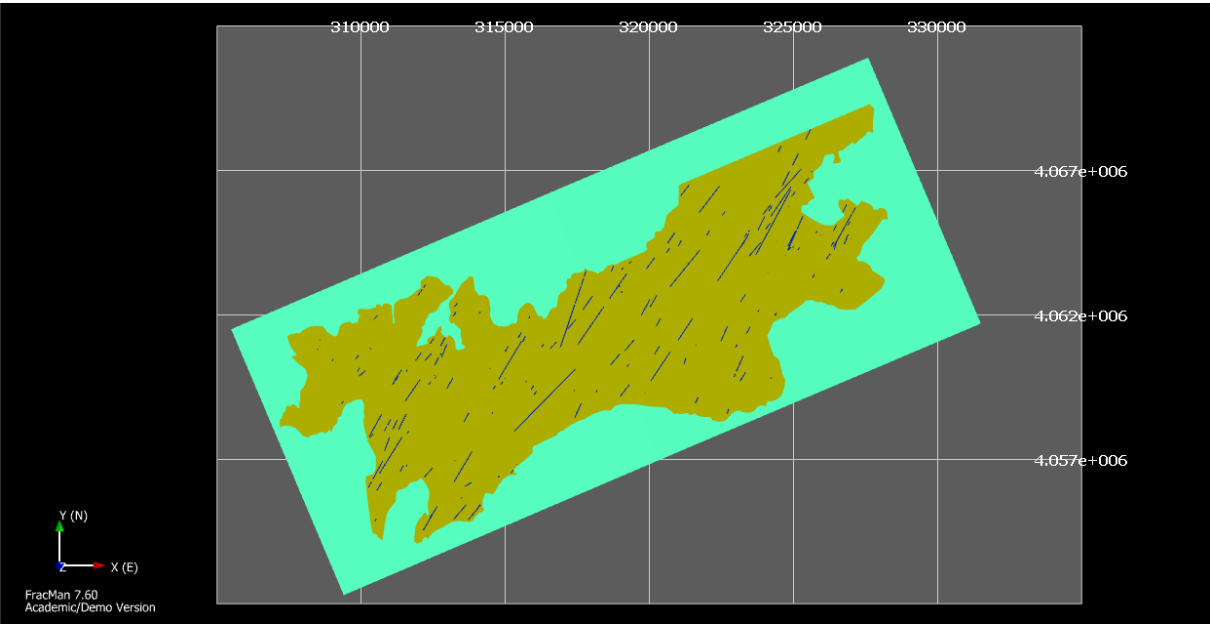


Figure 6.2.3. 2. Simulated trace map of Family 3, obtained from the intersection of simulated fractures with study area (600m).

6.2.4. Family 4

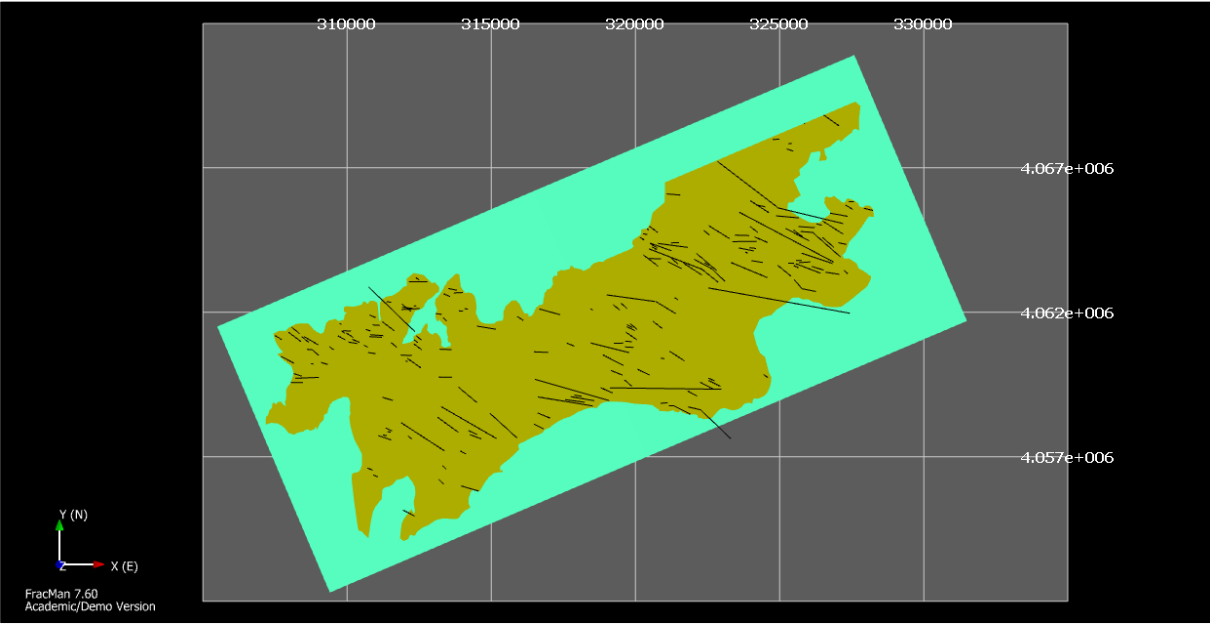


Figure 6.2.4. 1. Real trace map of Family 4.

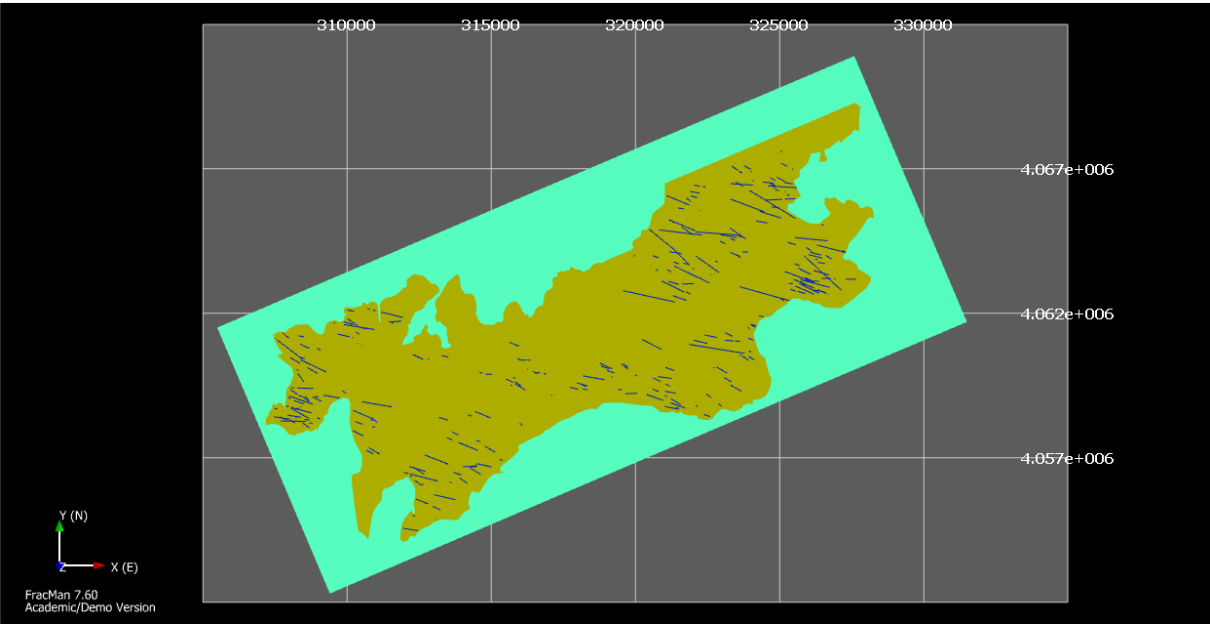


Figure 6.2.4. 2. Simulated trace map of Family 4, obtained from the intersection of simulated fractures with study area (600m).

6.2.5. Family 5

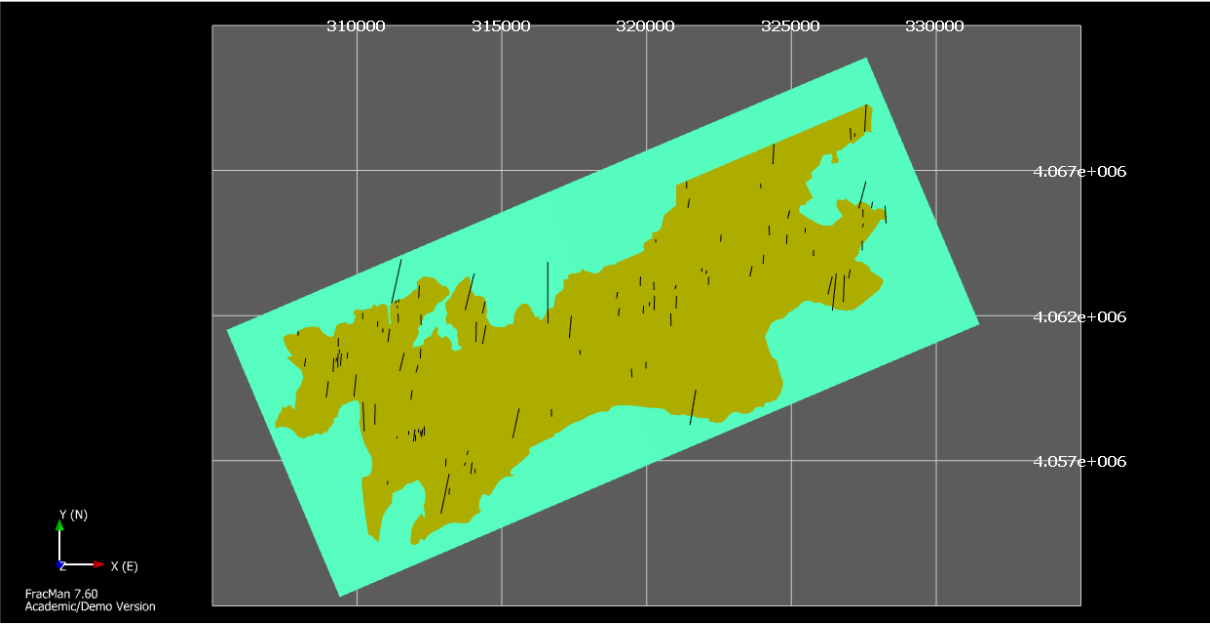


Figure 6.2.5. 1. Real trace map of Family 5.

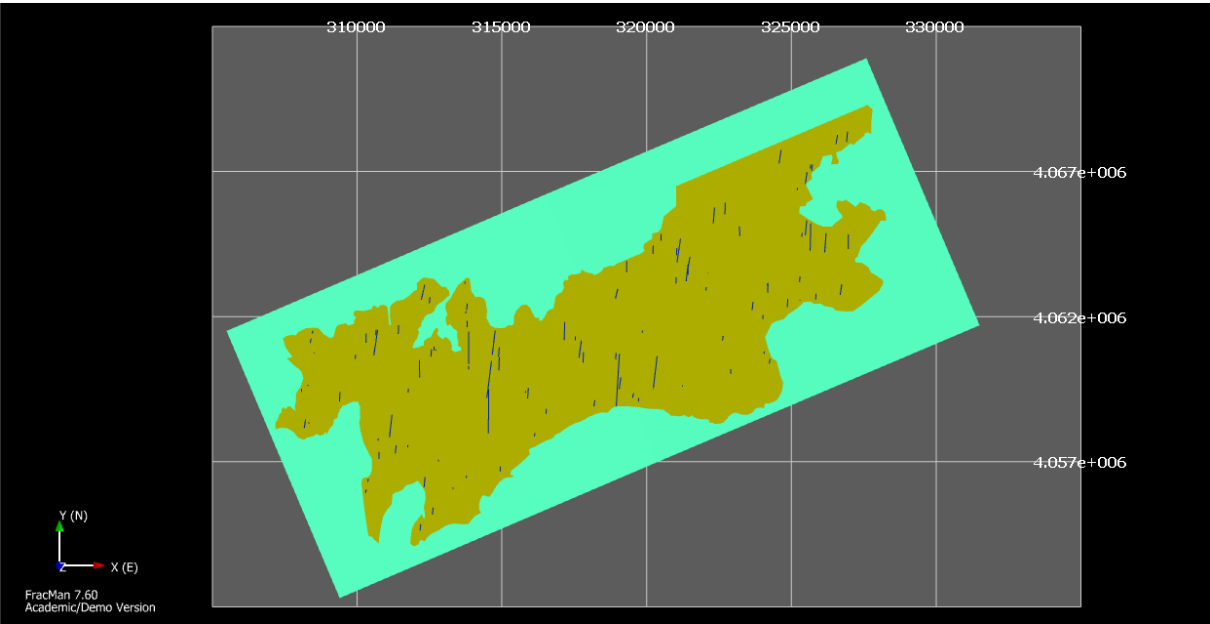


Figure 6.2.5. 2. Simulated trace map of Family 5, obtained from the intersection of simulated fractures with study area (600m).

6.2.6. Total Fracture Model

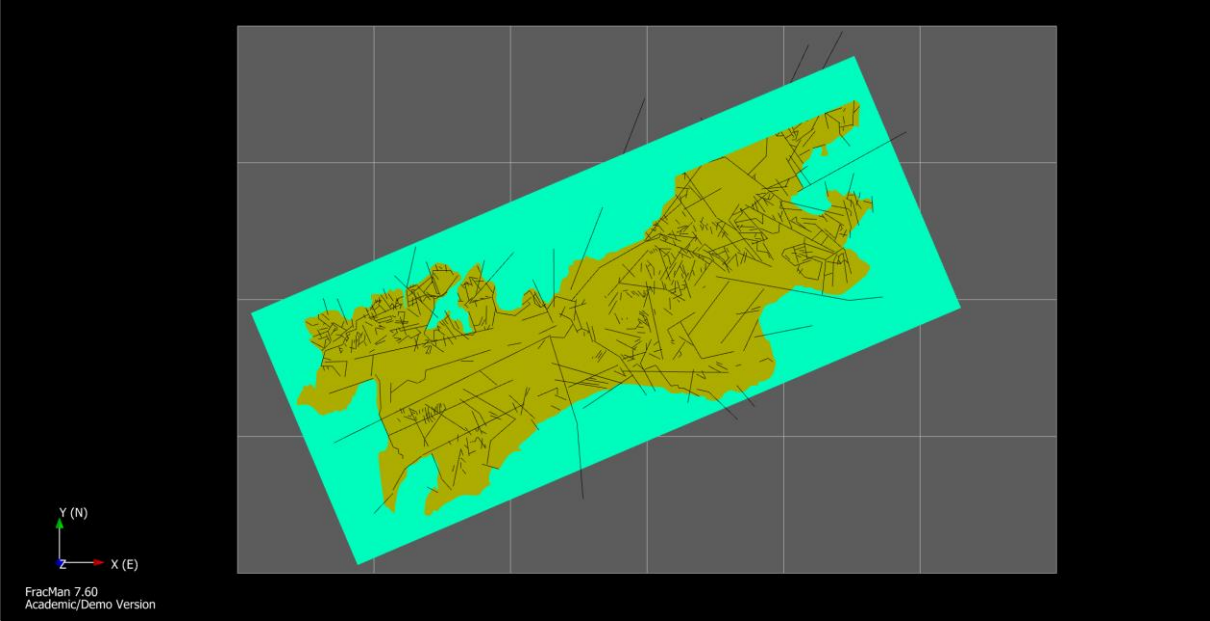


Figure 6.2.6. 1. Total real trace map.

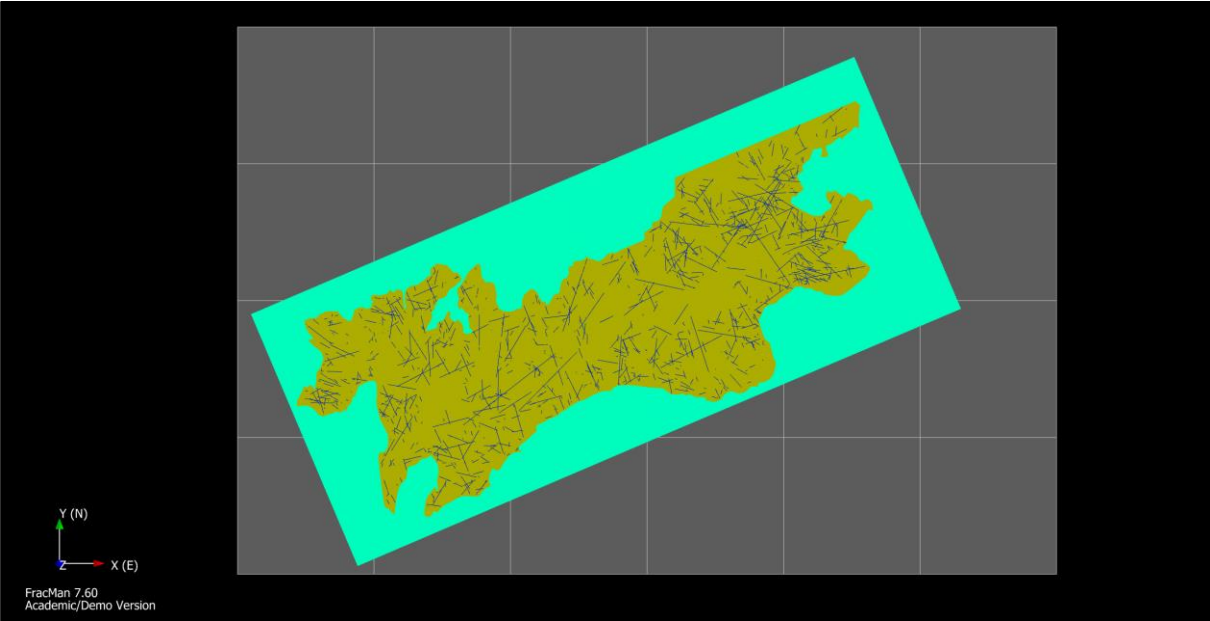


Figure 6.2.6. 2. Total simulated trace map obtained from the intersection of simulated fractures with study area (600m).

In analysing the visual comparison of the trace maps, a good correspondence was found in the families 1, 3, 4 and 5, both in terms of distribution and size of the fractures. Also for the value of P_{21} , Family 2 does not respond optimally to this analysis. It can be seen in Figures 6.2.2.1 and 6.2.2.2 that there is a certain discrepancy between the real trace map and the simulated one. The simulated map appears with a more homogeneous distribution with respect to the real traces and many smaller fractures. Obviously this factor is also reflected in the values of P_{21} calculated and shown in the previous chapter.

Obviously, there is also a good correspondence in the total simulated trace map, given that there is a good similarity in the single families.

Also in this case, as explained in chapter 5.1, there are discrepancies in all families, except for the family 5, in the lengths of the fractures. The probability of larger fractures, the tail of the probability distribution function, is so small that these types of fractures are almost never found in simulations. This problem could be solved by manually inserting some of the most significant and large fractures that the simulation does not take into consideration.

6.3. Comparison Length Histograms

After having visually compared the lineaments, we proceeded by matching the histograms of the Logarithms of lengths, calculating and comparing the sample number, mean, std. error of mean, median, mode, std. deviation, variance, range, minimum and maximum.

6.3.1. Family 1

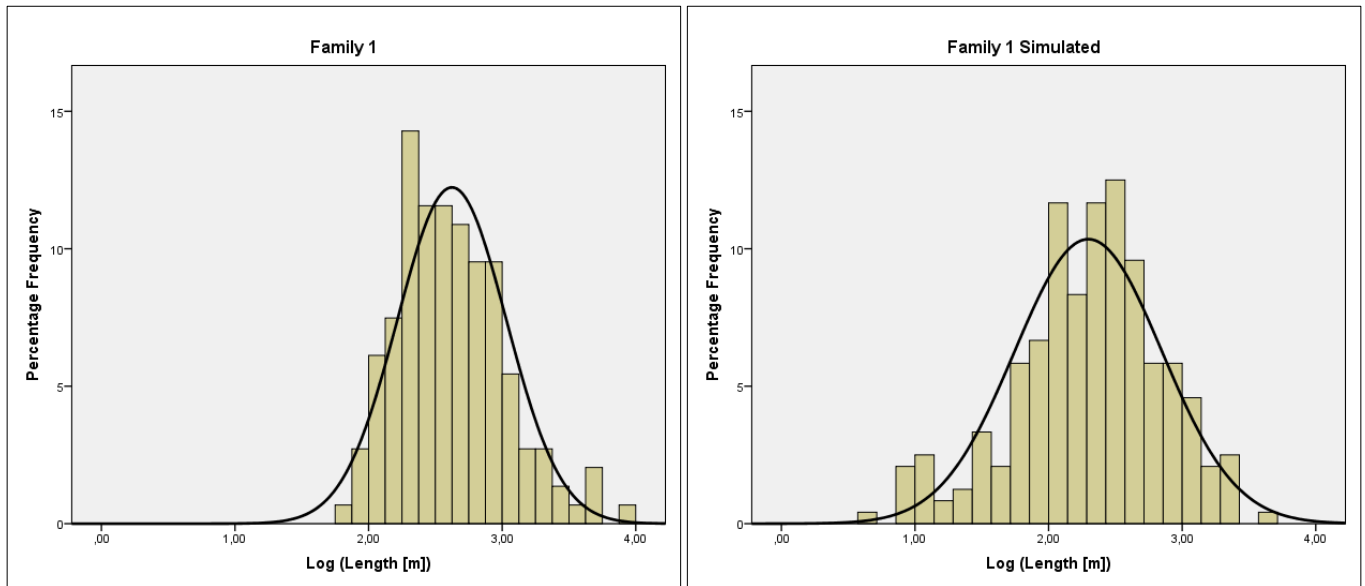


Figure 6.3.1. 1. A) Log (Length) Histogram of real trace map of Family 1. B) Log (Length) Histogram of simulated trace map of Family 1.

Statistics			
		Family1	Family1_Sim
N	Valid	147	240
Mean		2,6232	2,2970
Std. Error of Mean		,03362	,03555
Median		2,5600	2,3399
Mode		2,23 ^a	2,33 ^a
Std. Deviation		,40757	,55069
Variance		,166	,303
Range		2,19	3,05
Minimum		1,76	,58
Maximum		3,95	3,63

a. Multiple modes exist. The smallest value is shown

Figure 6.3.1. 2. Statistic comparison between real and simulated trace map of Family 1.

6.3.2. Family 2

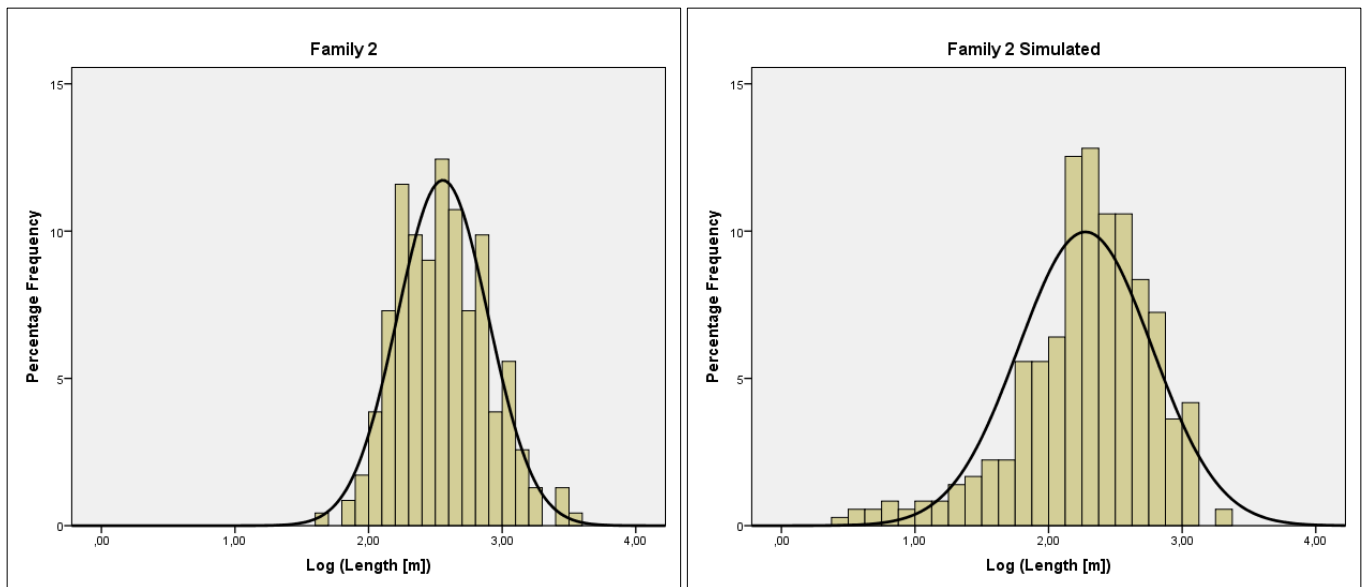


Figure 6.3.2. 1. A) Log (Length) Histogram of real trace map of Family 2. B) Log (Length) Histogram of simulated trace map of Family 2.

Statistics			
		Family2	Family2_Sim
N	Valid	233	359
Mean		2,5556	2,2754
Std. Error of Mean		,02228	,02639
Median		2,5218	2,3334
Mode		2,25	,87
Std. Deviation		,34015	,49998
Variance		,116	,250
Range		1,87	2,93
Minimum		1,65	,43
Maximum		3,51	3,36

Figure 6.3.2. 2. Statistic comparison between real and simulated trace map of Family 2.

6.3.3. Family 3

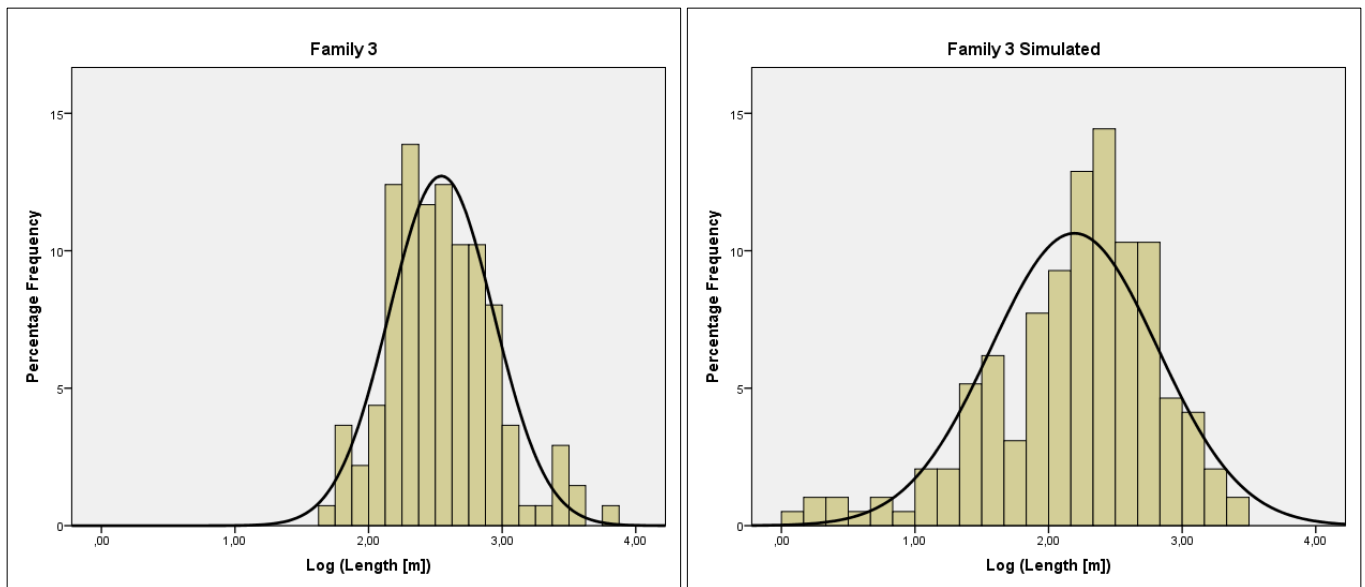


Figure 6.3.3. 1. A) Log (Length) Histogram of real trace map of Family 3. B) Log (Length) Histogram of simulated trace map of Family 3.

Statistics			
		Family3	Family3_Sim
N	Valid	137	194
Mean		2,5446	2,1928
Std. Error of Mean		,03349	,04488
Median		2,5109	2,3021
Mode		2,31	1,49 ^a
Std. Deviation		,39204	,62509
Variance		,154	,391
Range		2,16	3,35
Minimum		1,72	,14
Maximum		3,87	3,48

a. Multiple modes exist. The smallest value is shown

Figure 6.3.3. 2. Statistic comparison between real and simulated trace map of Family 3.

6.3.4. Family 4

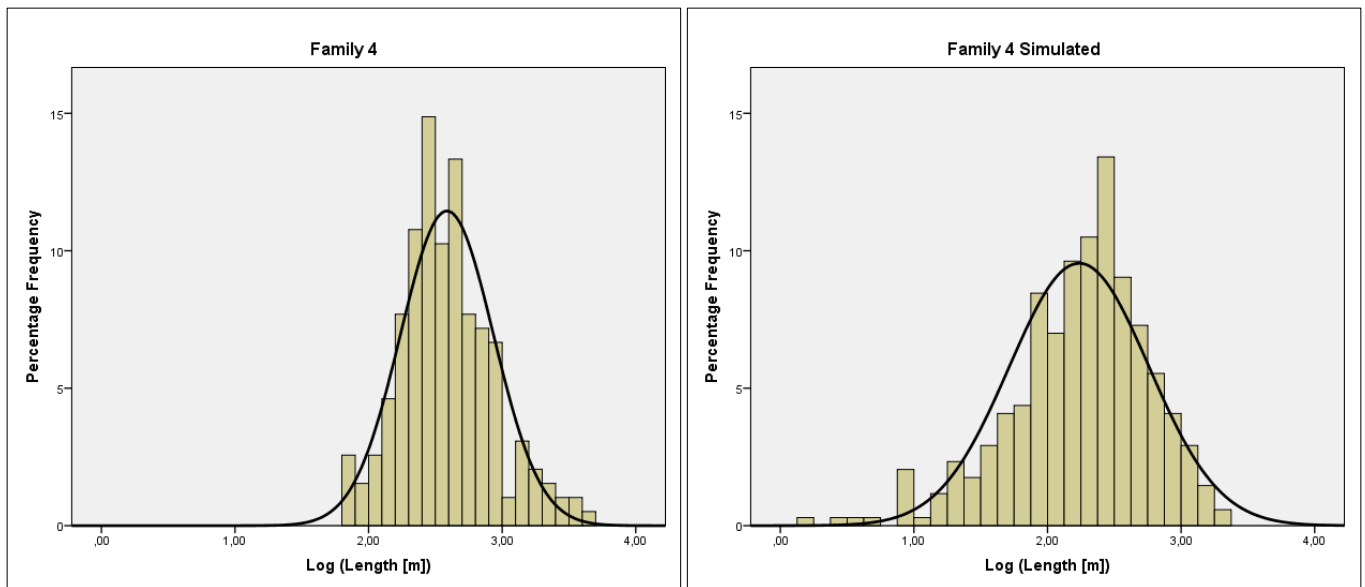


Figure 6.3.4. 1. A) Log (Length) Histogram of real trace map of Family 4. B) Log (Length) Histogram of simulated trace map of Family 4.

Statistics			
		Family4	Family4_Sim
N	Valid	195	343
Mean		2,5865	2,2366
Std. Error of Mean		,02495	,02821
Median		2,5568	2,3080
Mode		1,96 ^a	2,17
Std. Deviation		,34845	,52240
Variance		,121	,273
Range		1,86	3,16
Minimum		1,84	,13
Maximum		3,70	3,29

a. Multiple modes exist. The smallest value is shown

Figure 6.3.4. 2. Statistic comparison between real and simulated trace map of Family 4.

6.3.5. Family 5

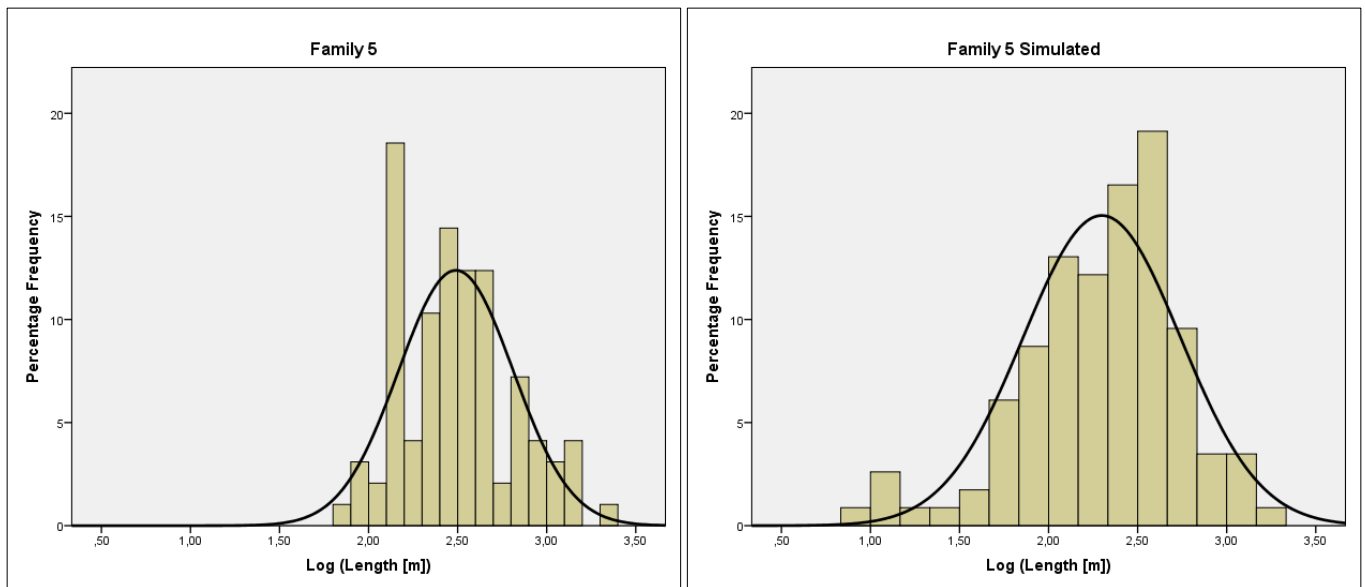


Figure 6.3.5. 1. A) Log (Length) Histogram of real trace map of Family 5. B) Log (Length) Histogram of simulated trace map of Family 5.

Statistics			
		Family5	Family5_Sim
N	Valid	97	115
Mean		2,4900	2,2986
Std. Error of Mean		,03270	,04121
Median		2,4569	2,3476
Mode		2,12	2,58
Std. Deviation		,32208	,44195
Variance		,104	,195
Range		1,49	2,29
Minimum		1,84	,89
Maximum		3,33	3,18

Figure 6.3.5. 2. Statistic comparison between real and simulated trace map of Family 5.

6.2.6. All Families

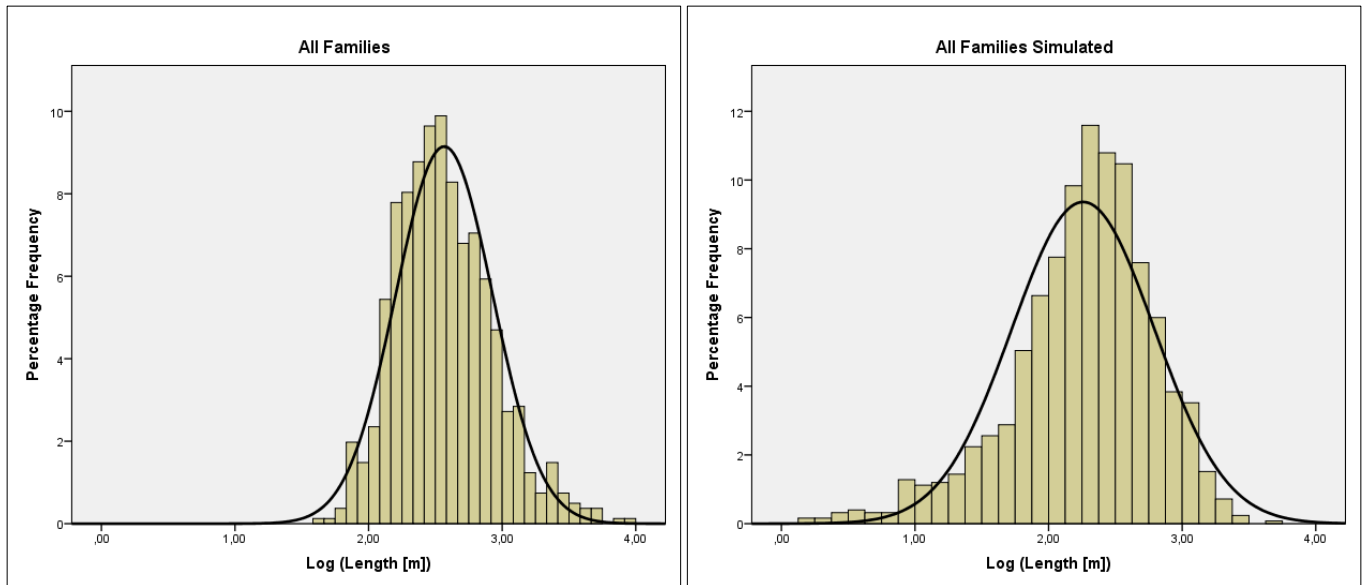


Figure 6.3.6. 1. A) Log (Length) Histogram of real trace map of totality of families. B) Log (Length) Histogram of simulated trace map of totality of families.

Statistics			
		All Families	All Simulated
N	Valid	809	1251
Mean		2,5656	2,2582
Std. Error of Mean		,01278	,01506
Median		2,5215	2,3294
Mode		2,29 ^a	2,17
Std. Deviation		,36340	,53264
Variance		,132	,284
Range		2,30	3,50
Minimum		1,65	,13
Maximum		3,95	3,63

a. Multiple modes exist. The smallest value is shown

Figure 6.3.6. 2. Statistic comparison between real and simulated trace map of all families.

6.4. Stereonet (stereographic projection) and Rose Diagram

6.4.1. Family 1

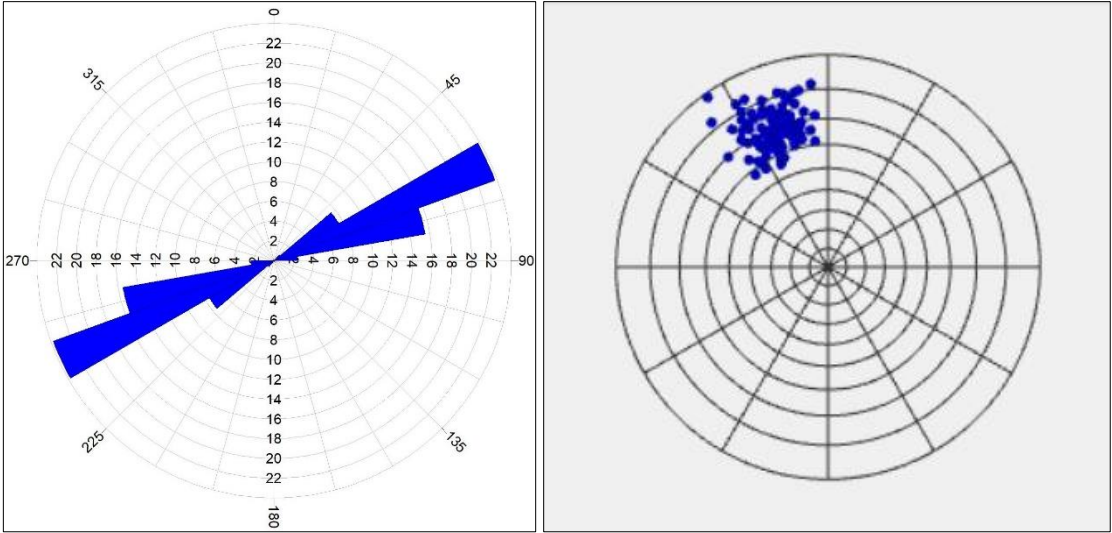


Figure 6.4.1. 3. a) Rose diagram of real trace map of Family 1. b) Polar stereographic projection of Fisher distribution that was inserted in the model creation of Family 1.

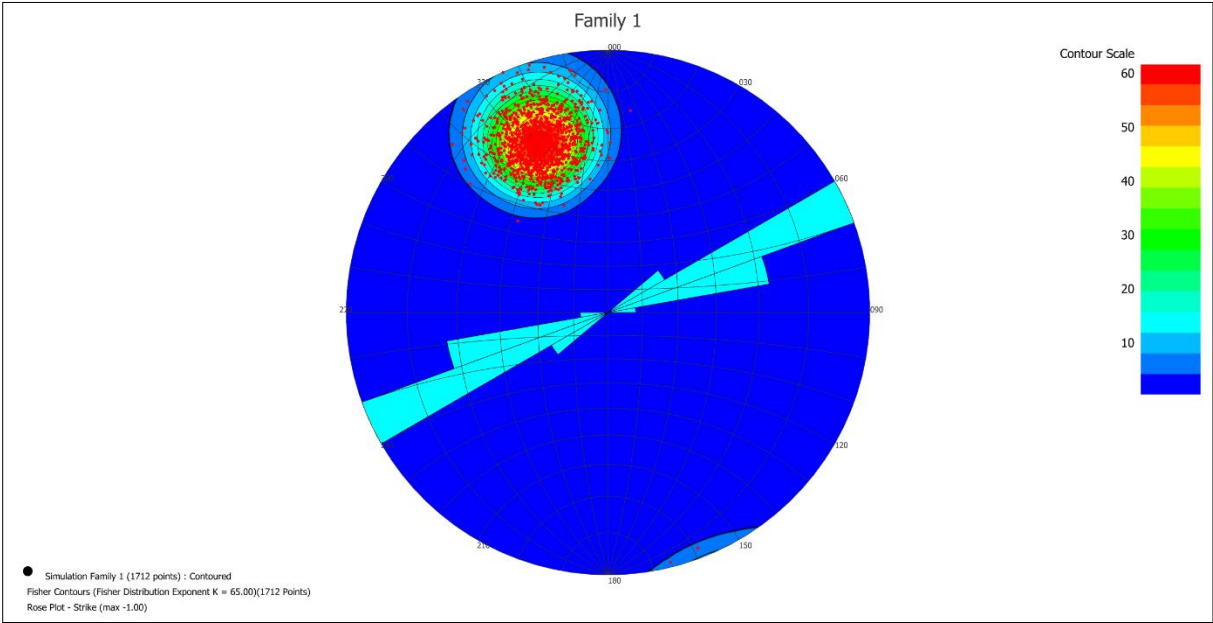


Figure 6.4.1. 4. Rose diagram and equatorial stereographic projection of simulated fractures of Family 1.

6.4.2. Family 2

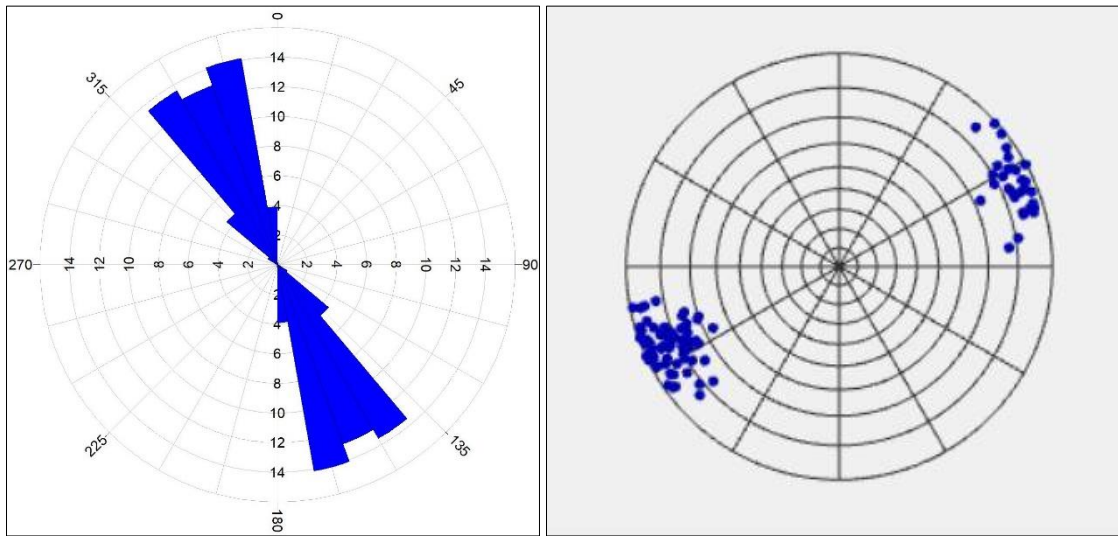


Figure 6.4.2. 3. a) Rose diagram of real trace map of Family 2. b) Polar stereographic projection of Fisher distribution that was inserted in the model creation of Family 2.

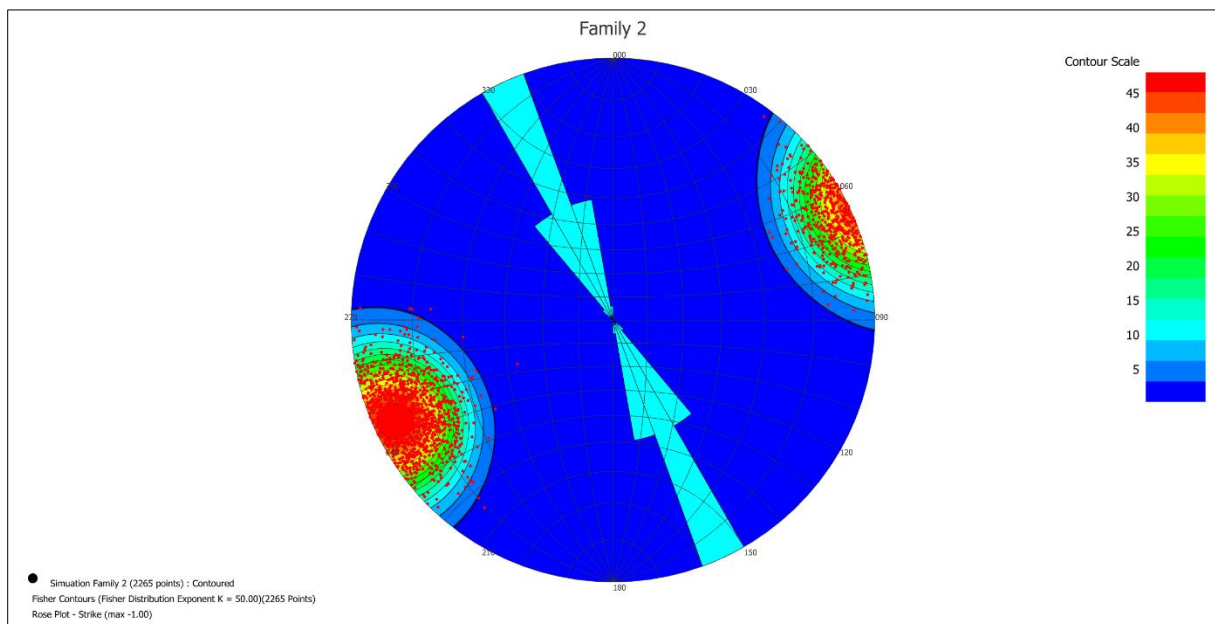


Figure 6.4.2. 4. Rose diagram and equatorial stereographic projection of simulated fractures of Family 2.

6.4.3. Family 3

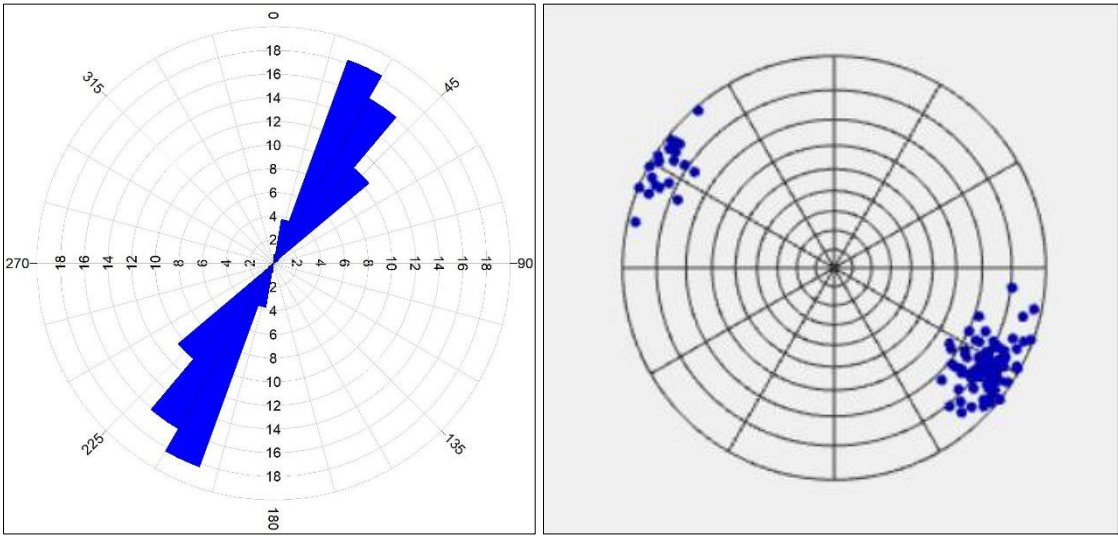


Figure 6.4.3. 3. a) Rose diagram of real trace map of Family 3. b) Polar stereographic projection of Fisher distribution that was inserted in the model creation of Family 3.

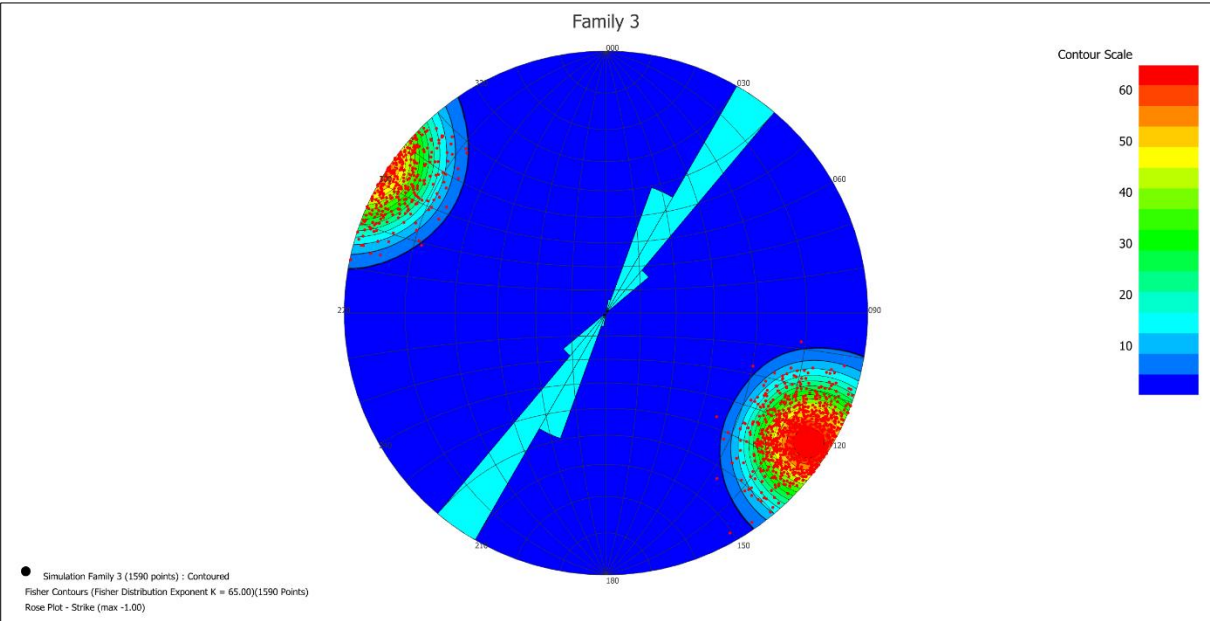


Figure 6.4.3. 4. Rose diagram and equatorial stereographic projection of simulated fractures of Family 3.

6.4.4. Family 4

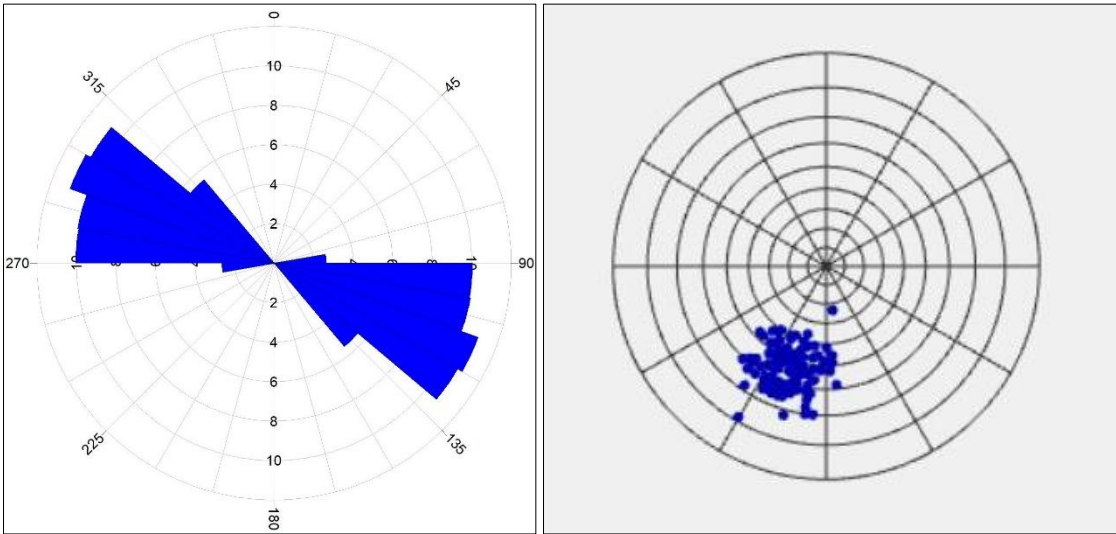


Figure 6.4.4. 3. a) Rose diagram of real trace map of Family 3i4. b) Polar stereographic projection of Fisher distribution that was inserted in the model creation of Family 4.

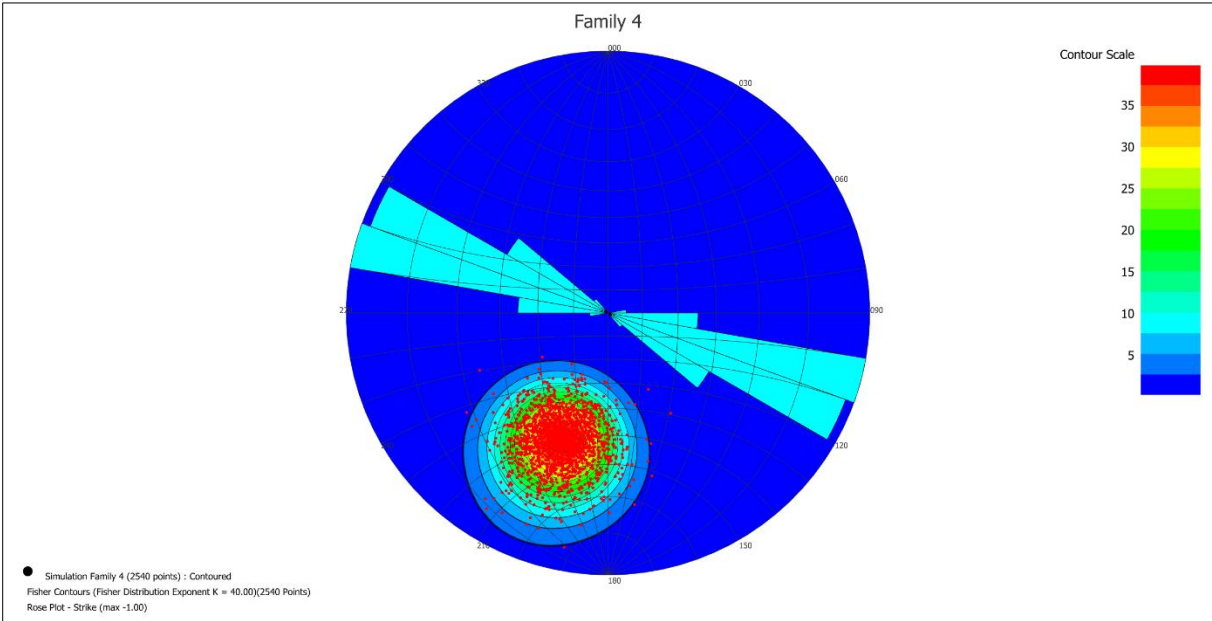


Figure 6.4.4. 4. Rose diagram and equatorial stereographic projection of simulated fractures of Family 4.

6.4.5. Family 5

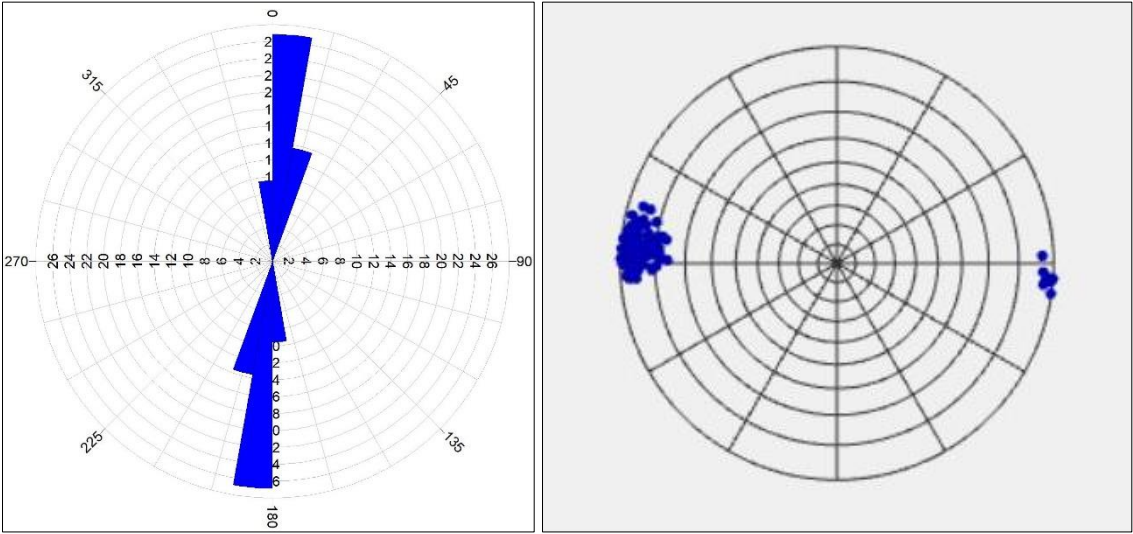


Figure 6.4.5. 3. a) Rose diagram of real trace map of Family 5. b) Polar stereographic projection of Fisher distribution that was inserted in the model creation of Family 5.

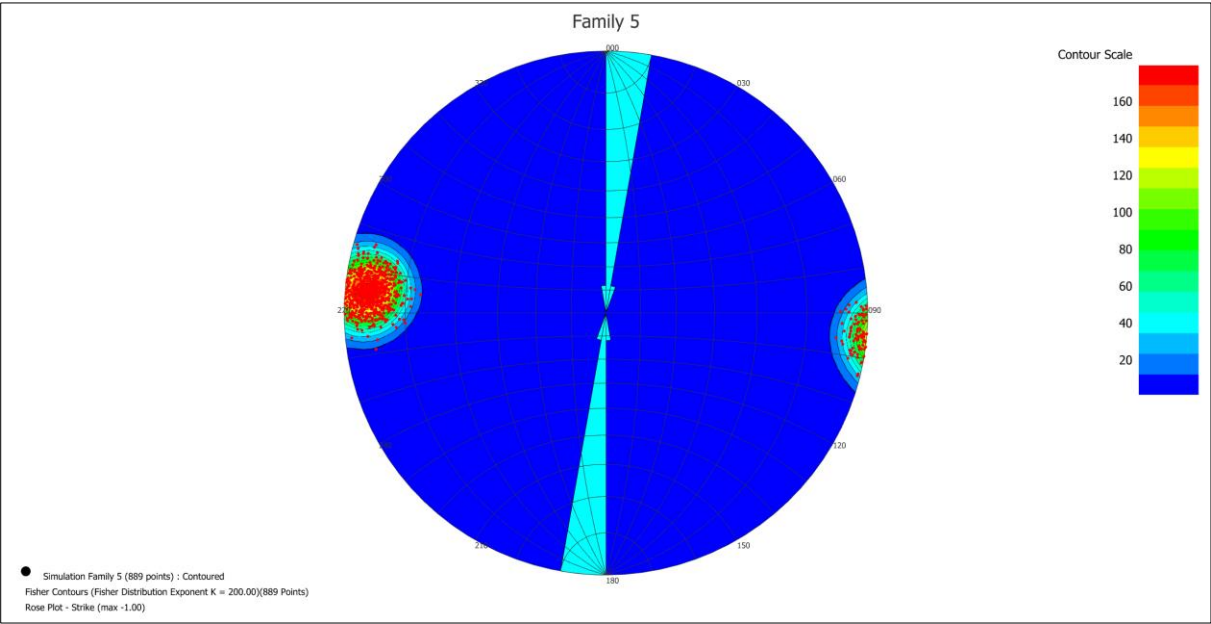


Figure 6.4.5. 4. Rose diagram and equatorial stereographic projection of simulated fractures of Family 5.

6.4.6. Total Simulated Fracture Model

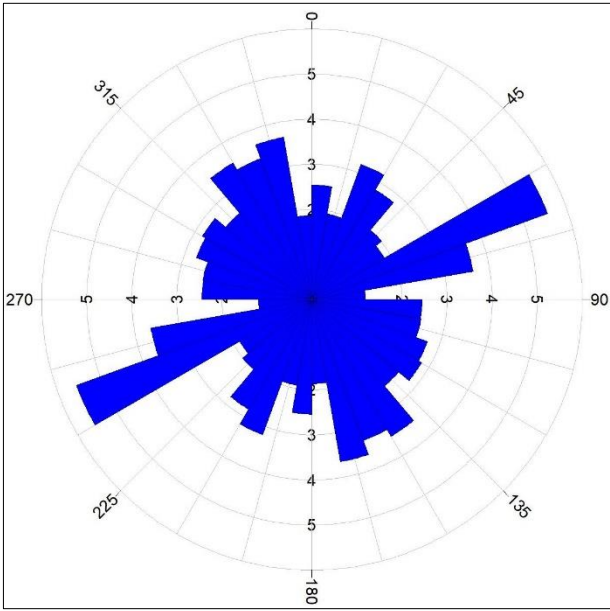


Figure 6.4.6. 3. Rose diagram of total real trace maps.

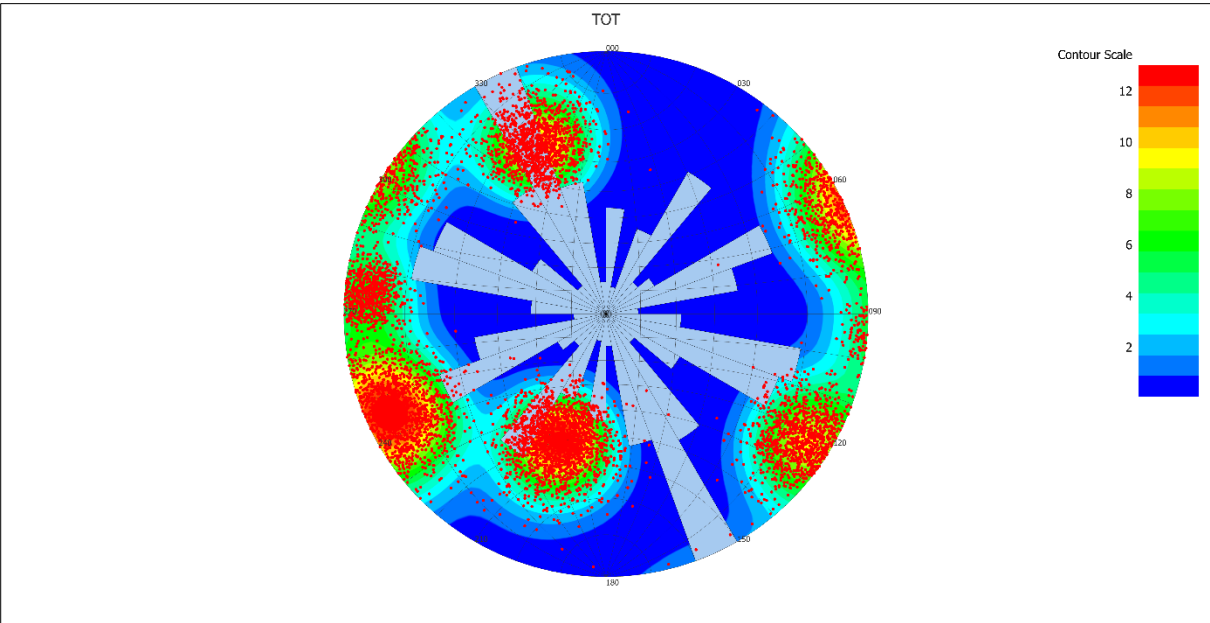


Figure 6.4.6. 4. Rose diagram and equatorial stereographic projection of total simulated fractures. of Family

This last verification useful to validate the 3D Discrete Fracture Model was carried out by first comparing the real rose diagrams of single families with those of the simulations. In a second step, the stereographic projections of the fractures obtained from the model were compared with those, that depend on the parameters of the Fisher distribution, included in the model (chapter 4). Finally, the total real rose diagram (Figure 6.3.6.1) was analysed with that of the complete model (Figure 6.3.6.2).

This analysis led to a good approximation of reality, but some inconsistencies were noted in this case too. For families 2 and 4, where the distribution of real orientations turns out to be more homogeneous within the chosen range, a change has been noted in the rose diagram. This change is due to the fact that, by choosing a Fisher distribution, the model has created fracture families with a much higher frequency in the median value of the chosen range. To have a series of values more dispersed in the range, the parameter k of the Fisher distribution can be decreased. This factor did not result in any problems in families 1, 3 and 5, because the distribution lobes were much more pronounced than in other cases. This change in the simulation can also be seen in the simulated total rose diagram (Figure 6.3.6.2), where the most important family appears to be Family 2 and no longer Family 1, as in reality. Also Family 4 is very accentuated in the simulation with respect to the rose diagram of the real fractures.

7. Caves and springs for hydrogeological validation

For the hydrogeological validation of the 3D Discrete Fracture Model caves and springs mapped by IGME (Instituto Geológico y Minero de España) were included in the study area of Sierra de las Nieves park.

In the following figure caves are shown in brown and springs in blue.

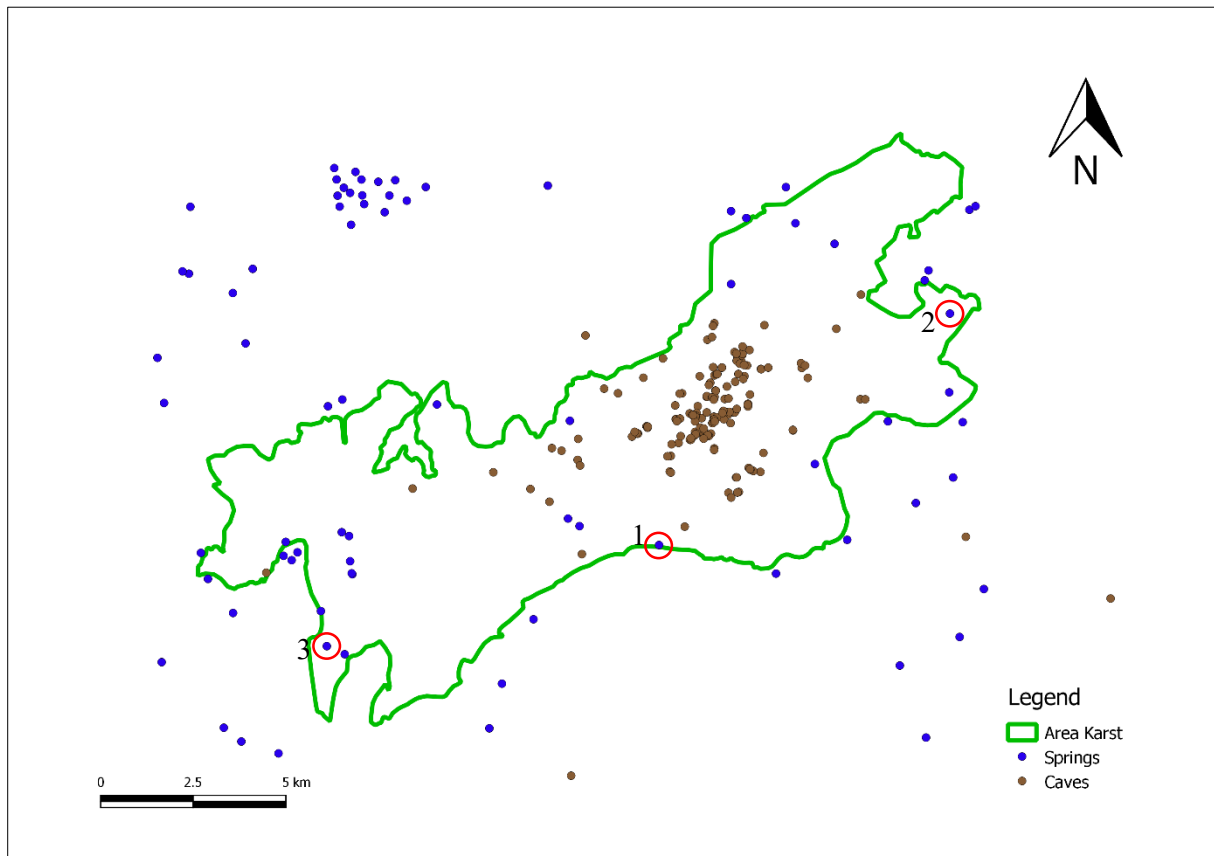


Figure 7. 1 – Location of caves (in brown) and springs(in blue). Mayor springs: Río Verde (1), Río Grande/Zarzalones (2) and Río Genal (3).

The number of caves that fall within the study area examined in this thesis work is 166, while the number of springs is 20. Each single point was inserted in FracMan with the respective coordinates x, y and z. Caves and springs are considered by the software as wells with a depth chosen by the author of 2000 m from ground level.

Figure 7.2 shows caves (in white) and springs (in blue) in three dimensions in FracMan.

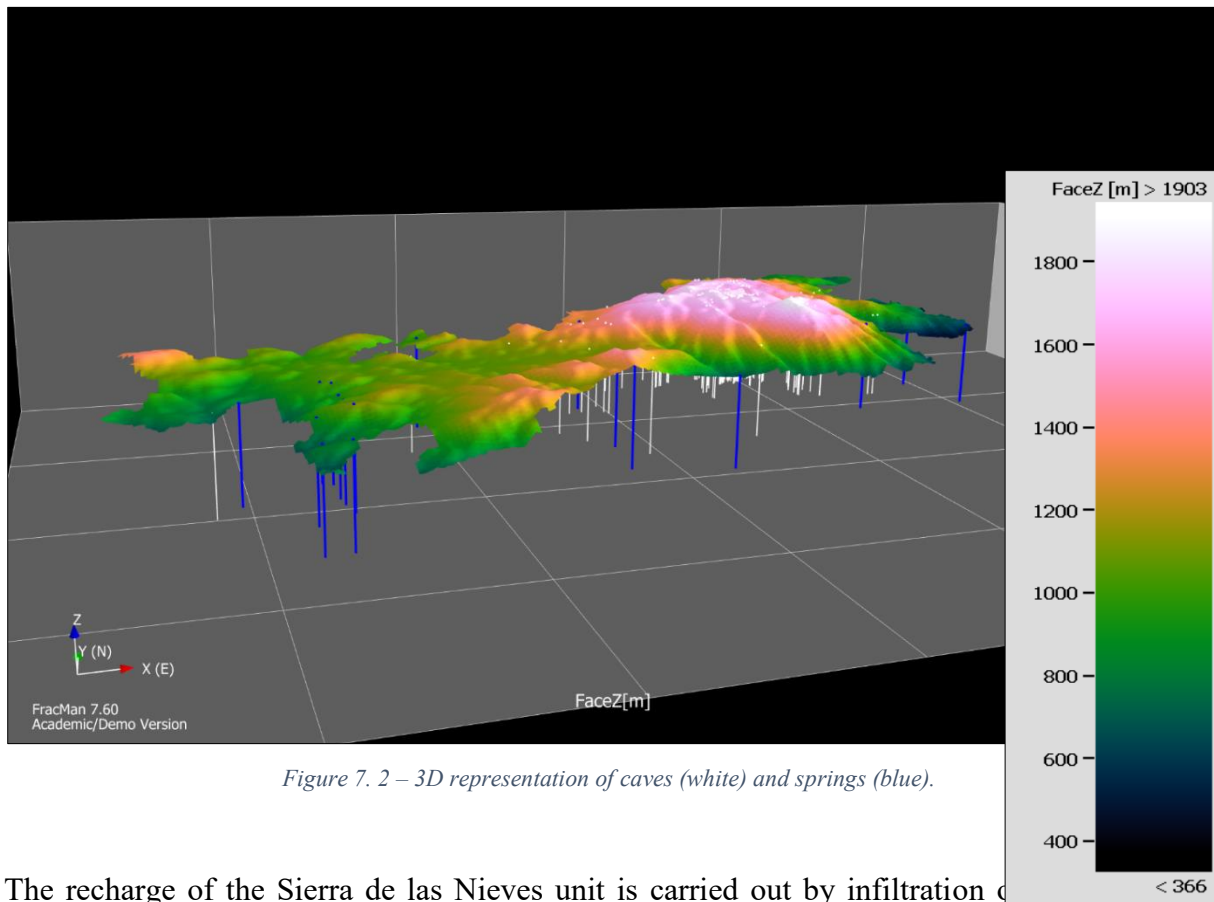


Figure 7. 2 – 3D representation of caves (white) and springs (blue).

The recharge of the Sierra de las Nieves unit is carried out by infiltration of snowmelt, while discharge takes place, mainly, through springs located on the SE edge, outside the study area, since extractions through pumping are of small magnitude. From the previous reports of the IGME (1983), the Provincial Council of Malaga (1988) developed the "Hydrogeological Atlas of the province of Malaga", which refers to the most important springs, which have a typical karstic behaviour: Río Verde (with an average flow of 750 l/s), Río Grande or spring of Zarzalones (725 l/s) and the upwelling of Igualaja or birth of the Río Genal (230 l/s) (Liñan, 2005). These three springs are highlighted in figure 7.1 with the numbers 1, 2 and 3 respectively.

The discharge occurs, fundamentally, in natural regime through the springs and only in some exceptional cases there is influence of pumping. As of December 1995, significant rains were registered, and a clear hydrodynamic response was observed in the controlled springs (Liñan et al., 1996). The hydrographs of Río Grande and the Río Verde springs, obtained from limnigramas, show the rapid and spectacular increase in flow that occurs in response to rainfall. This hydrodynamic response, with very pointed floods and large differences in flow between the tip of the flood and the end of depletion, reveals the existence of functional karstification in the drainage sector of the aquifer.

8. Qualitative Analysis of Fracture Clusters

Before proceeding with the analysis of the possible trajectories within the geological formation examined (Chapter 9), a qualitative analysis was carried out of the possible groups of fractures (clusters) that could give rise to a flow of water in the karst aquifer.

In this analysis the groups of fractures considered, to hypothesize a possible connection, therefore the possibility of flow and leakage of water from the springs, are groupings of at least 20 intersecting fractures.

In the analysis carried out, the number of clusters obtained is 12, the smallest formed by the set of 20 fractures and the biggest (in figure 8.1 in blue) composed of 5411 fractures.

From the qualitative analysis of the realization of the clusters (Figures 8.1, 8.2 and 8.3), it can be analysed that there are small clusters and three main groups of fractures, shown in the figures in light blue, yellow and blue color. The yellow group is located in the west part of the study area, the blue covers a small part in the central area and finally, the largest group (light blue) and more interesting from the geological point of view of the karst covers a very large area of the study area. The last group of fractures could describe the behaviour of the complexity of the karst. As can be seen from Figure 8.1 this cluster has a significant narrowing in the central area of the area, in correspondence to the Turquillas fault.

The study by Liñan (2005) shows that the slight differences in the isotopic content and in the levels of upwelling between the Río Grande spring (450 m above sea level) and the springs of Río Verde (675 m a.s.l.) and Río Genal (700 m a.s.l.) suggest a possible subdivision due to the fault of the Turquillas: a western one (from the aforementioned fault to the West), whose recharge area corresponds to the Llanos de la Nava, drained by Río Verde, which is very close to the fault, and Río Genal, and another eastern (from the Turquillas fault to the East), with its recharge area located in the Torrecilla area, drained mainly by the Río Grande spring. As Liñan explains, however, there are no geological or hydrogeological arguments that support this hypothesis.

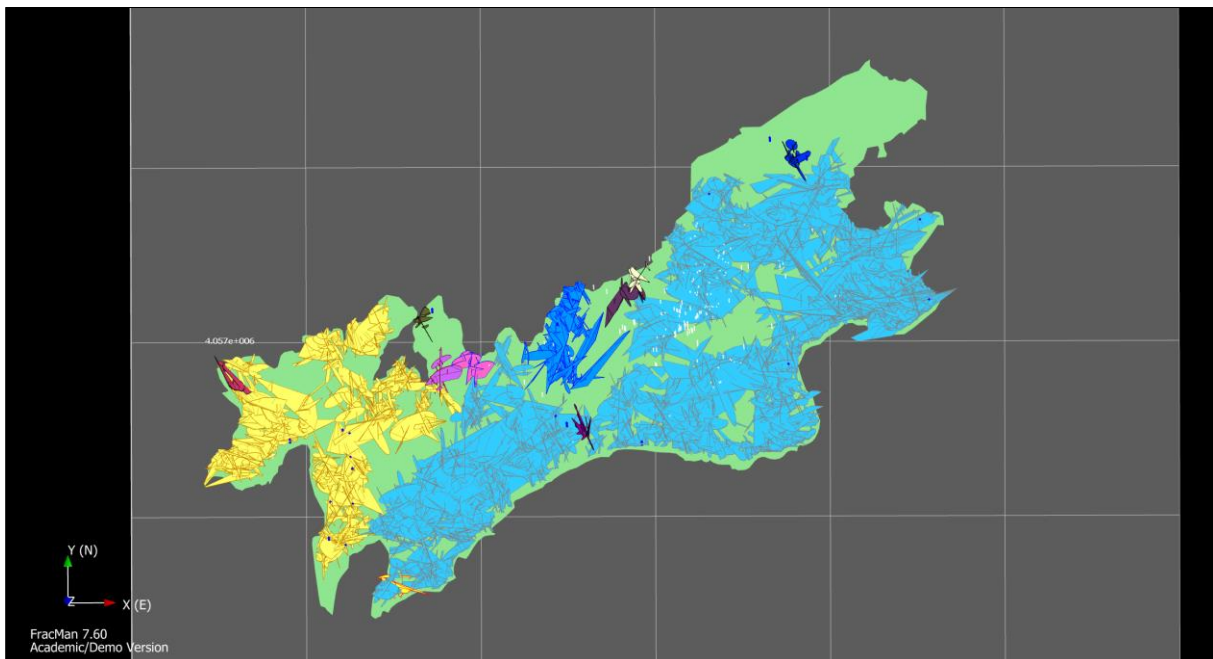


Figure 8. 1. 2D representation of clusters.

The study of Liñan argues that the continuity of the geological structure throughout the sector and the great thickness of the aquifer materials in this area (a powerful carbonated series that in turn is folded), suggest that the Turquillas accident it must not constitute a hydrogeological barrier proper, but it can allow the flow to the East (The directions of the flow are studied in the next chapter).

Although the karstic drainage has been organized preferably towards the spring of Río Grande, the heterogeneity inherent to the karstic environment implies, in this case, the existence of different levels of karstification and between these levels there is no total hydraulic connection, as evidenced by the existence of springs permanent in time, located at different levels.

From the qualitative analysis of the clusters and from the analyses and hypotheses supported by Liñan, it can be seen that in the 3D Discrete Fracture Model we can see an important influence of the Turquillas fault, with a substantial narrowing of the light blue cluster, without constituting a hydrogeological barrier. The narrowing, as explained by Liñan, could give rise to an influence on the main flow direction in the study area.

Another important factor that is dealt with by Liñan is the heterogeneity of the karst and the non-existence of a total hydraulic connection. This factor is represented by the 3D model with the presence of different clusters without connections between them.

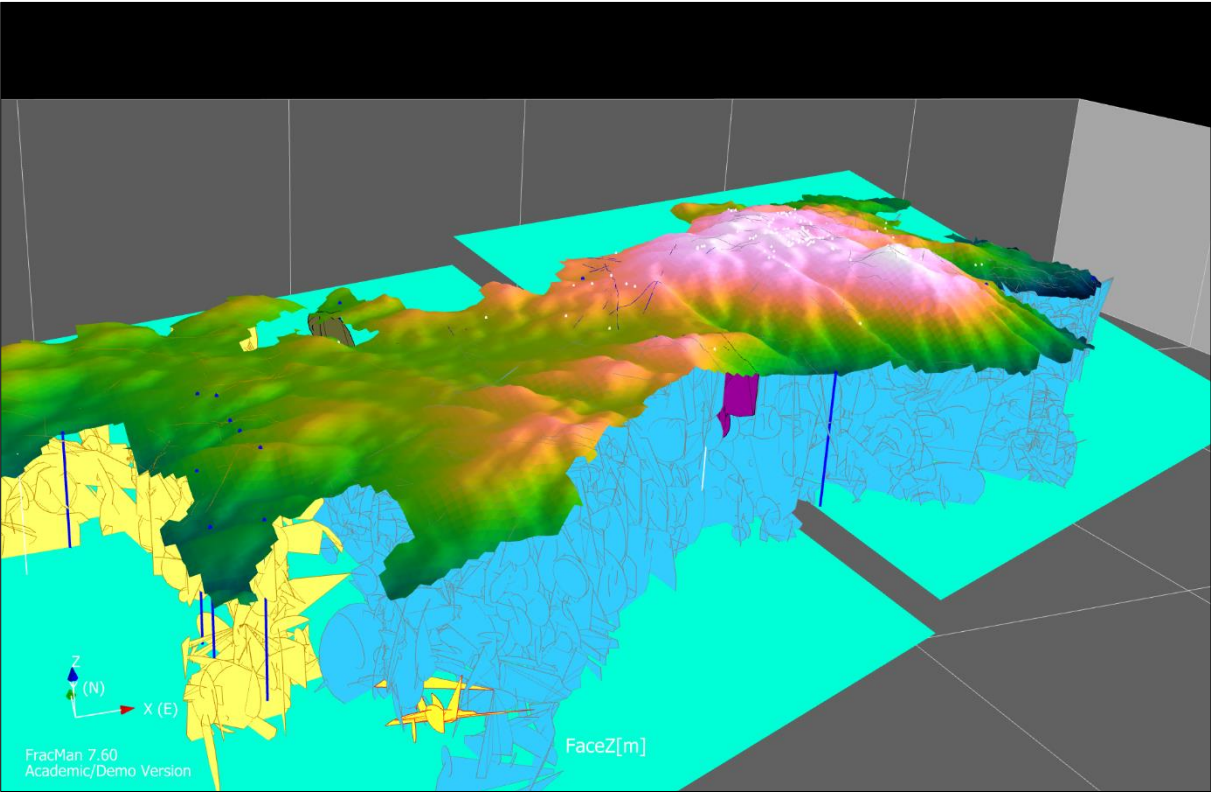


Figure 8. 2. 3D south-view of clusters.

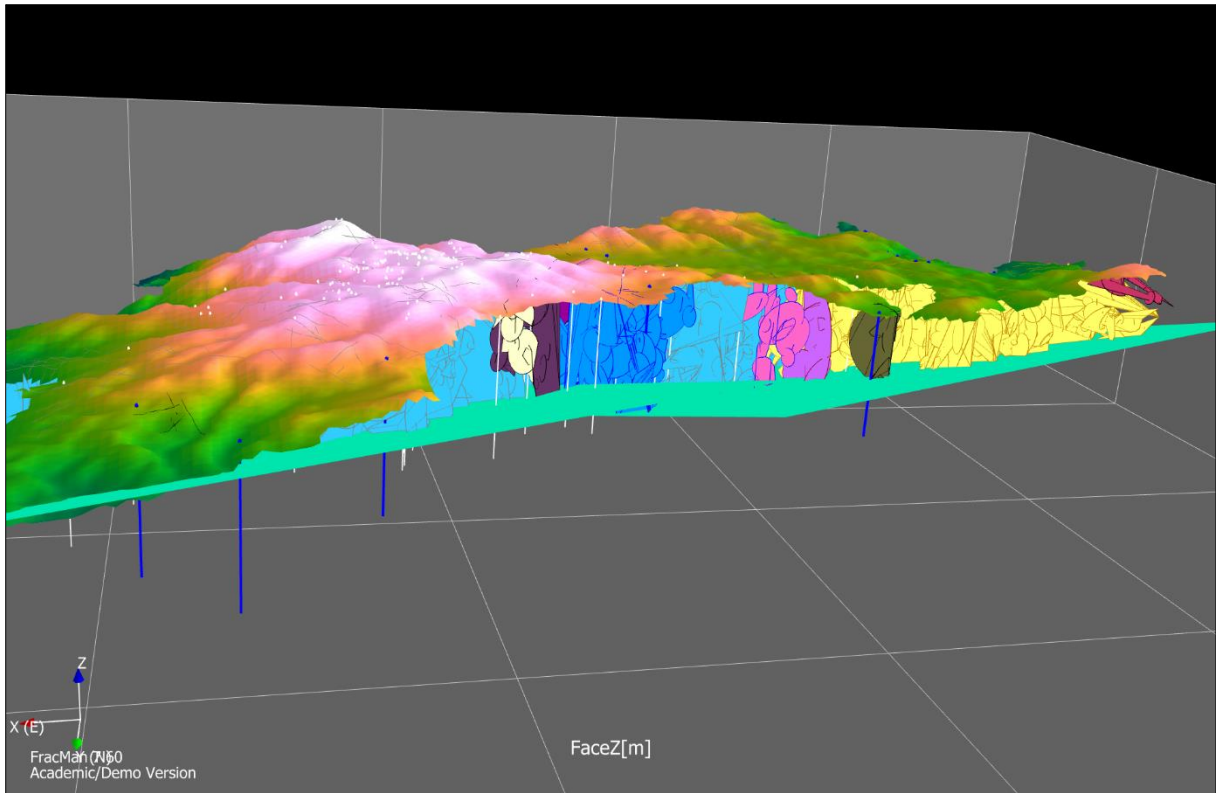


Figure 8. 3. 3D north-view of clusters.

9. Pathway Analysis (3D Discrete Fracture Network Model)

Through the Pathway function of Static Analysis, FracMan is able to analyse all the possible trajectories that reach each spring from each cave.

Of the 166 caves mapped in the study area, there are 39 that are not used by the software to create possible water passages in the subsoil. As for the wellsprings, there are 3, out of a total of 20, which are not connected with any cave.

The caves not used by the Pathway function could correspond to old openings created by the paleo-karst process that currently do not contribute to the water supply in the aquifer. The 4 springs not used by the software, three of these located in the NE of the study area, correspond to a result obviously not conforming to reality, because they are determined *in situ*.

The analysis shows that there are 742 possible connections between caves and springs. The sources with more connections are Zarzalones, Río Verde and other four. All these are located in the central part (Río Verde) or in the eastern area (Zarzalones). The origin of these trajectories corresponds to the area with the highest concentration of caves, i.e. in the upper part of the Sierra de las Nieves (Pico de Torrecilla). Río Genal spring has few connections and only originates from the caves of Llanos de la Nava, the area west of the fault of Turquillas.

As can be seen from the results obtained, the three-dimensional model shows substantially two distinct zones: the first in the east of the study area, corresponding to the yellow cluster shown in the previous chapter, corresponding to a part of Llanos de la Nava and the second drainage area it is related to the central and eastern part of the study area, corresponding with the Pico Torrecilla (Blue Cluster). This behaviour, depending on the clusters of fractures (Chapter 8), can be related, as analysed by Liñan and highlighted in the previous chapter, to the Turquillas fault. Turquillas fault does not constitute a hydrogeological barrier proper, but it can allow the flow to the East (Liñan, 2005).

Durán and López Martínez (1992) published the results of a tracer test conducted in Sierra de las Nieves. The test consisted of the pouring of fluorescein in the siphon of the Sima G.E.S.M. chasm, with the aim of establishing the direction of the underground flow. As a starting hypothesis, it was considered that fluorescein would be detected fundamentally in the Río Verde spring, for reasons of proximity. However, the result of the experimental showed that most of the tracer appeared in the Río Grande spring (Zarzalones), while in the fluocollectors located in the upwellings of Río Horcajos and Río Verde, the tracer amount was much minor (Durán, 1996). This indicates that the underground flow in this sector is directed, mainly, towards the NE.

In our study the result obtained with respect to the underground flow, with a slight difference with the study of Durán, results to have a direction SE and not NE. From the study mentioned above, however, it appears that there is a flow towards the southern area of the study area, having found the tracer also in the Río Verde spring, but with a smaller quantity. However, this implies a connection between the mountainous area of Sierra de las Nieves and the sources south of the study area.

In the following figures (Figures 9.1 and 9.2) two- and three-dimensional fractures used by the software for Pathway Analysis are shown. In the following ones (9.3 and 9.4), in 2D and 3D, only the representation of some of the conduits.



Figure 9. 1. Some examples of 2D representation of fractures used by the Model for Pathway Analysis.

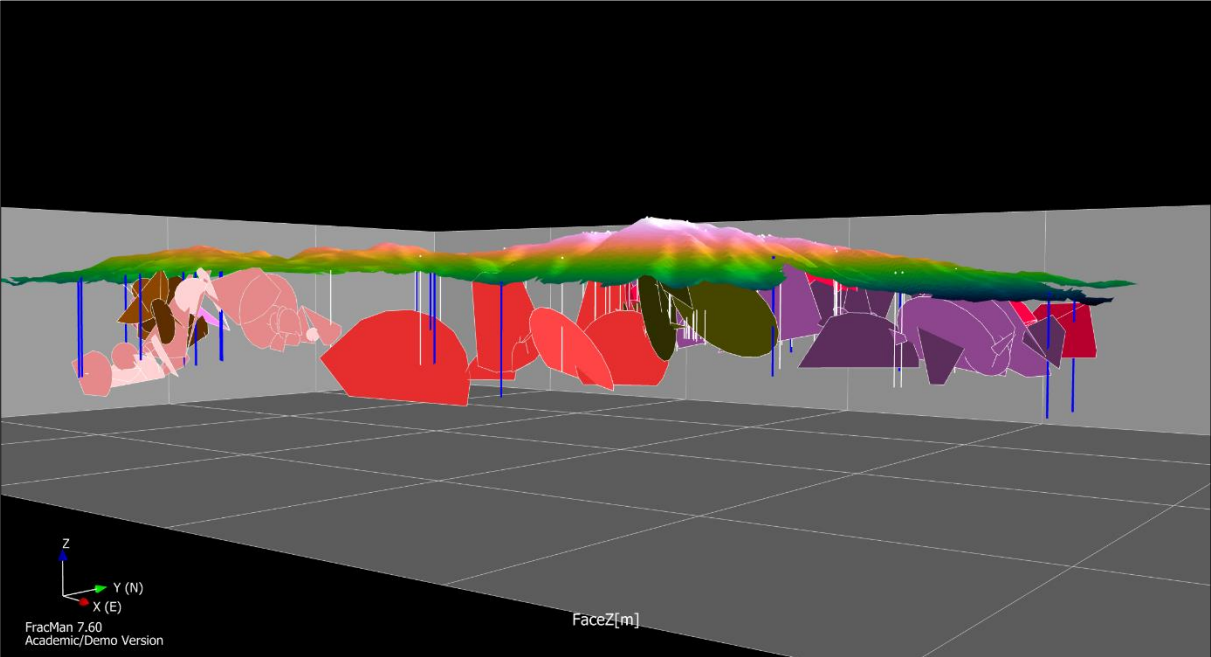


Figure 9. 2. Some examples of 3D representation of fractures used by the Model for Pathway Analysis.

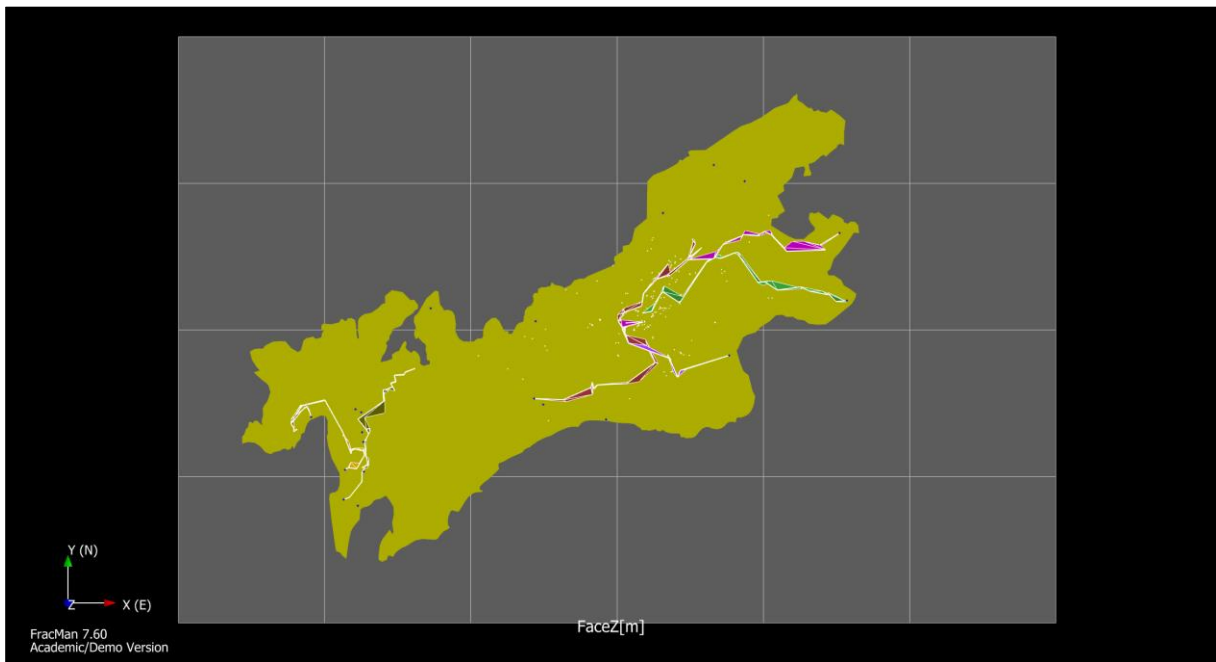


Figure 9. 3. Some examples of 2D representation of conduits used by the Model for Pathway Analysis.

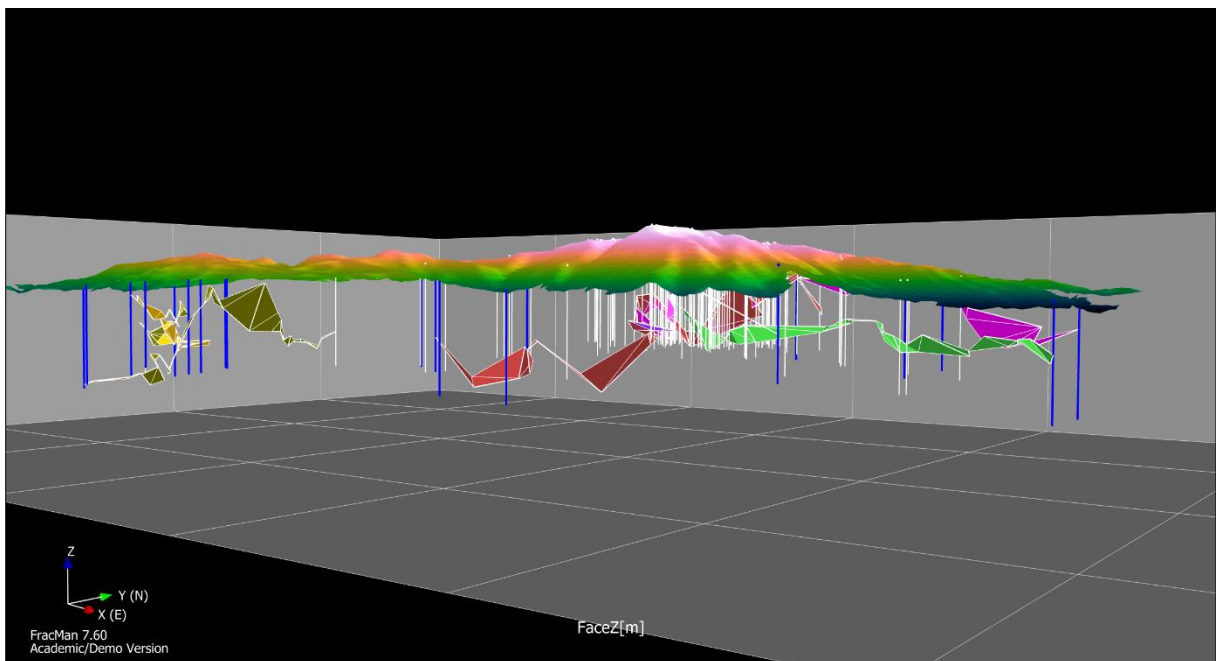


Figure 9. 4. Some examples of 3D representation of conduits used by the Model for Pathway Analysis.

From the comparison of the 3D Discrete Fracture Network Model with the flow direction studies of Liñan (2005), Durán (1996) and López Martínez (1992), it is clear that the model is more than satisfactory.

Comparing some parameters (average) of the Río Verde source with those of Zarzalones (Table 9.1), it can be seen that the contribution to the Río Verde, Path Volume = 155 m³, is much lower than that of the Zarzalones spring with 232 m³. This shows that even for the model there is a preference for flow towards the east rather than the south.

<i>Spring</i>	<i>Number of Fractures</i>	<i>Path Length [m]</i>	<i>Min Conductance [m³/sec]</i>	<i>Path Area [m²]</i>	<i>Path Volume [m³]</i>
Río Verde	17.83	8200	$6.62 \cdot 10^{-5}$	2059020	155
Zarzalones	22.24	8928	$8.08 \cdot 10^{-5}$	3293430	232

Table 9. 1. Average of parameters referred to the springs Río Verde and Río Grande (Zarzalones)

Subsequently, the springs present in the west part of the study area were analysed. The information held is only relative to the Río Genal spring, which is one of the largest measured by previous studies. With this analysis we want to determine which of the eight sources is the most important from the hydrogeological point of view and to check if it corresponds to Río Genal spring. The parameters evaluated are shown in Table 9.2, and Figure 9.5 shows their location in the Sierra de la Nieves.

<i>Spring</i>	<i>Number of Fractures</i>	<i>Path Length [m]</i>	<i>Min Conductance [m³/sec]</i>	<i>Path Area [m²]</i>	<i>Path Volume [m³]</i>
Río Genal	25	8696	$2.86 \cdot 10^{-5}$	1524401	120
Spring 14	22.5	6759	$4.26 \cdot 10^{-5}$	1491741	106
Spring 17	20.5	6487	$5.16 \cdot 10^{-5}$	1643677	110
Spring 19	15	5024	$4.87 \cdot 10^{-5}$	1118351	104
Spring 20	14.5	5038	$5.08 \cdot 10^{-5}$	1307415	98
Spring 26	16	5568	$5.97 \cdot 10^{-5}$	822270	41
Spring 28	15	5316	$5.14 \cdot 10^{-5}$	1314968	100
Spring 29	15	5515	$5.11 \cdot 10^{-5}$	1147333	107

Table 9. 2. Average of some parameters referred to the springs present in the western area.

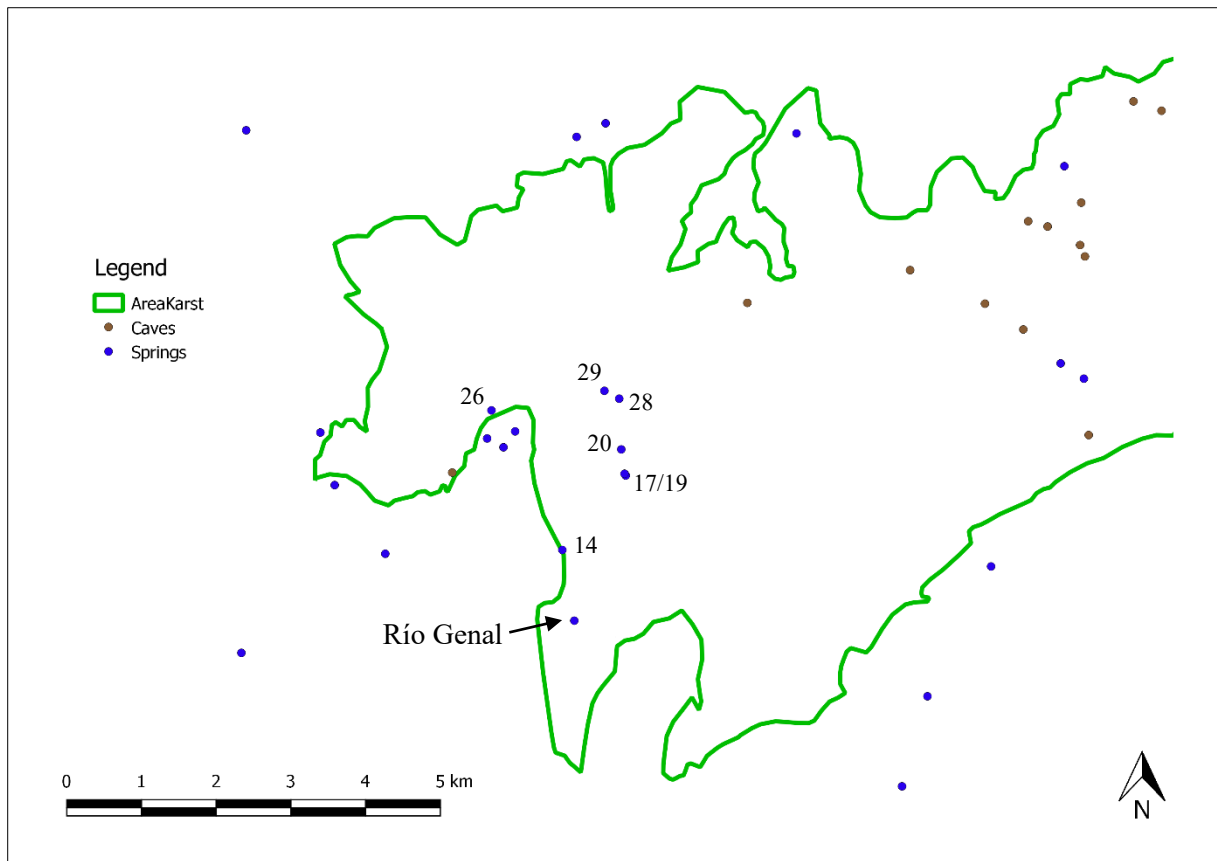


Figure 9. 5. Location of the springs present in the western area.

From the analysis carried out on the sources relating to the western part of the Sierra de las Nieves, it is clear that the Río Genal spring corresponds to the largest one according to the parameters of Number of Fractures (25), Path Length (8696 m), Min Conductance ($2.86 \cdot 10^{-5} \text{ m}^3/\text{sec}$) and Path Volume (120 m^3). The analysis shows how the model was able to best describe even the most western area of the study area.

A final analysis concerning the possible water paths in the karst aquifer of Sierra de Las Nieves has been carried out considering the directions of the fractures that are used by the 3D Discrete Fracture Network Model (Figure 9.6.a) and the directions relative only to the hypothetical conduits created by the model (Figure 9.6.b).

The rose diagrams presented in the following figures were compared with field analyses carried out by Liñan (2005) and by the speleologist study of the main caves of Torrecilla massif (Pedrera, 2015).

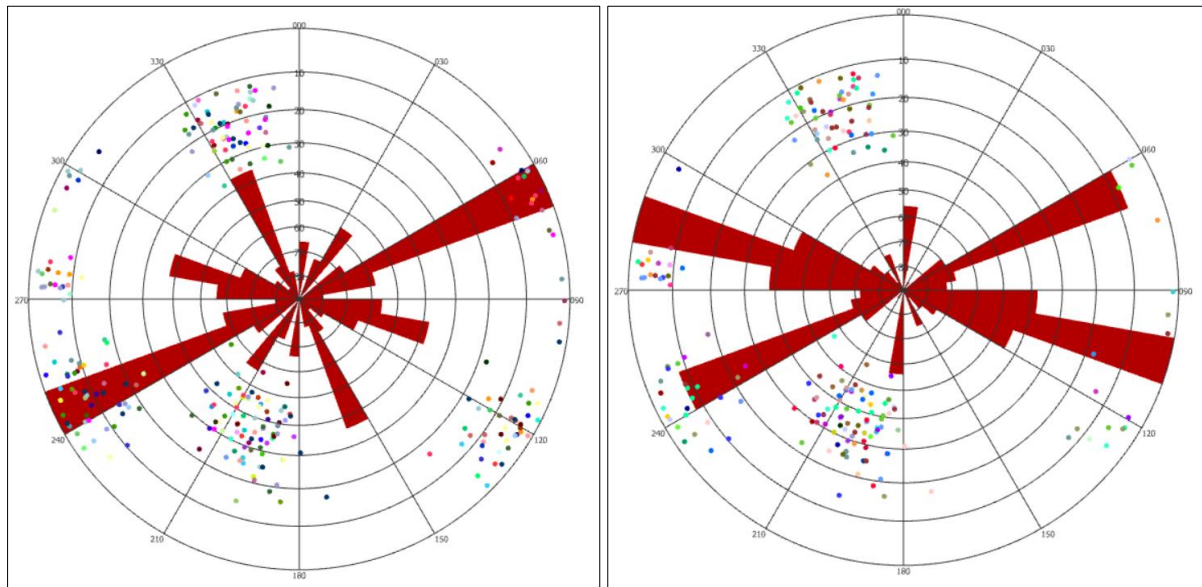


Figure 9. 6. a) Rose diagram of fractures that are used by the 3D Discrete Fracture Network Model. b) Rose Diagram of conduits that are used by the 3D Discrete Fracture Network Model.

From the directional analysis completed with the Pathway function, the main families of fractures used by karst are 1, 2, 4 and 3, while families that generate conduits, according to the model, are families 4, 1 and 5.

From the study carried out by Liñan (2005) it is clear that in the rose diagram (Figure 9.7), in which the karstification plans are represented, the most important families are N-S (Family 5), N150E (Family 2) and less significant N60E and N30E (Families 1 and 3).

Figure 9.8 shows the analyses reported in the article by Pedrera, *Structural controls on karstic conduits in a collisional orogen*, where the directions of the karstic conduits are highlighted in relation to the depth of the three main caves studied by speleologists: Sima GESM, Sima Prestá and Sima del Aire. The main directions of the Sima GESM are N120E and N50E (Families 4 and 1). The Sima Prestá results to have a development practically in all the directions with a greater percentage N-S (Family 5) and finally in the Sima del Aire the directions N15E and N30E (Families 5 and 3) appear more important.

From the comparison of this information, it can be deduced that the karst directions of the fractures result for Liñan are families 5, 2, 1 and 3, while in the model the family 5 is not so significant.

From the analysis of the main caves, however, the result is surprisingly good because the Sima GESM and Sima Prestá have a development in the directions N120E, N50E and N-S, which are perfectly correlated with the result obtained from the directions of the possible conduits in the 3D Discrete Fracture Network Model.

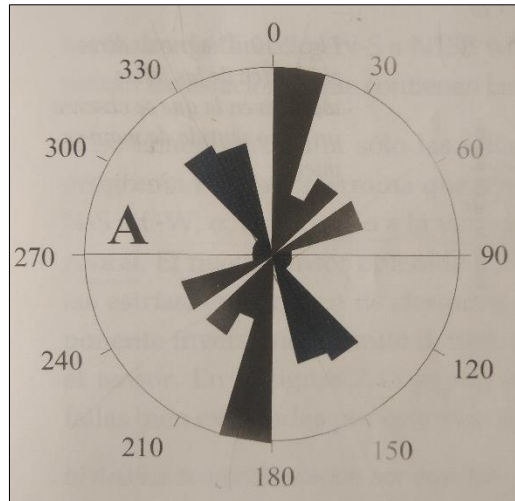


Figure 9. 7. Rose diagram of plans of kastification (Liñan, 2005).

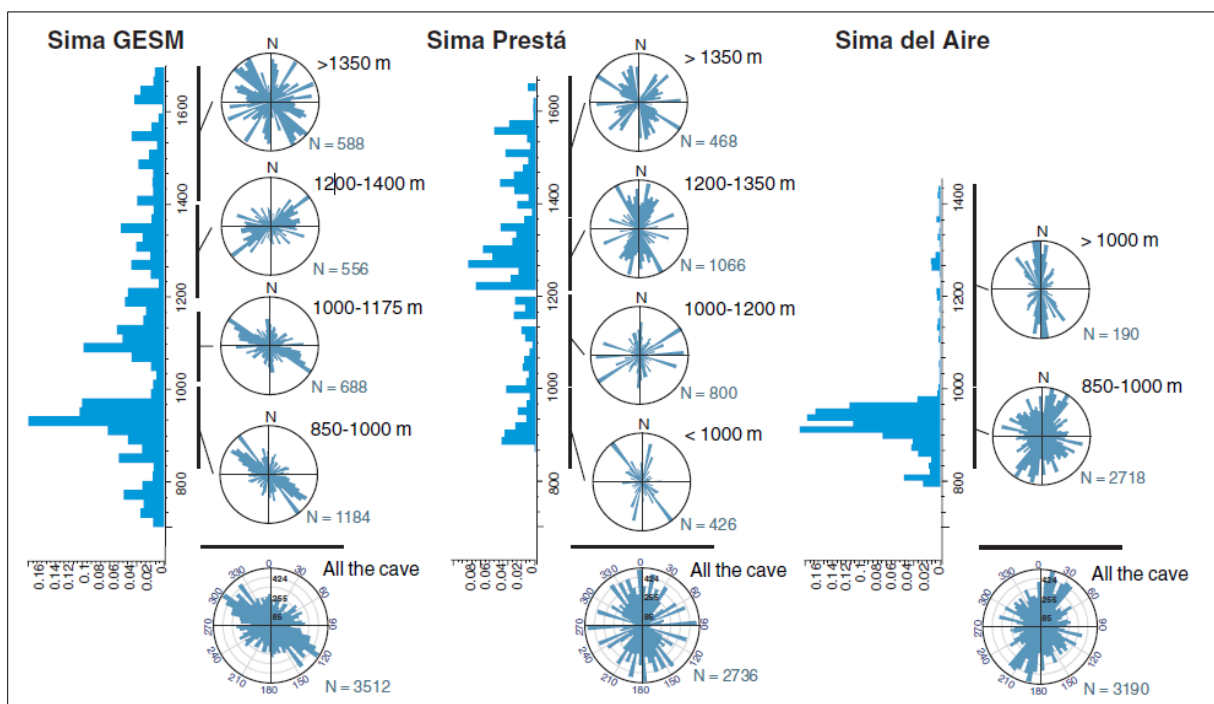


Figure 9. 8. Vertical distribution of the cave conduits and rose diagrams showing conduit direction at different depths. (Pedrera et al., 2015)

10. Critical Stress Analysis

FracMan can compute which fractures over a given region are critically stressed. The Mohr model assumes that the shear strength of a fracture is given by a function $f(\sigma)$, and shear failure occurs if

$$|\tau| \geq f(\sigma)$$

In other words, if the shear stress across the fracture exceeds its shear strength, the two opposing faces slip against one another. In this case, the fracture is said to be *critically stressed*, and its permeability may be enhanced.

FracMan supports two strength models, Mohr-Coulomb and Barton-Bandis. The first one was used for this analysis.

In the case of Mohr-Coulomb model, fracture shear strength is given by

$$f(\sigma) = S_0 + \sigma \tan(\theta_f)$$

Where S_0 is the *cohesion* of the fracture and θ_f is the *friction angle* in degrees.

In the study of Liñan, three tectonic phases are defined in chapter 3.1: Strike-slip phase (Lower Miocene), phase of strike-slip regime (Upper-Miocene) and extensive phase (Pliocene and Ancient Quaternary).

The normal extensive phase seems to be the most marked in the massif and is the one that has played an essential role in the acquisition of the hydrodynamic properties of the aquifer, as well as in karstogenesis. This extensive phase caused the opening of fractures with N-S and NNW-SSE directions (Families 5 and 2), such as the important N130E fractures (Family 4) that cross the study area, favouring the development of karstification according to these directions. However, groundwater flow is not only conditioned by fracturing, but stratification and geological structure exert a great influence (Liñan, 2005).

For this reason, the critical stress analysis was made only for the extensive phase, the most recent of the paleo-efforts analysed and also the most influential for the development of the karst aquifer.

The data used for this analysis are as follows:

$$\sigma_1 = 0.8;$$

$$\sigma_2 = 0.4;$$

$$\sigma_3 = 0.2;$$

$$\text{Trend}_1 = 230;$$

$$\text{Plunge}_1 = 85;$$

$$\text{Trend}_3 = 40;$$

$$\text{Plunge}_3 = 5;$$

$$\text{Friction Angle} = 30^\circ.$$

The result obtained is highlighted in the following table, which shows the percentages of critical fractures subject to this tectonic phase.

Family	Family 1	Family 2	Family 3	Family 4	Family 5
Critically Stressed Fractures [%]	0.1	27	0	62	0

Table 10. 1. Percentage critically stressed fractures.

The families that result under stress are 3 and 5. Figures 10.1 and 10.2 show the Mohr diagrams relating to these families of fractures.

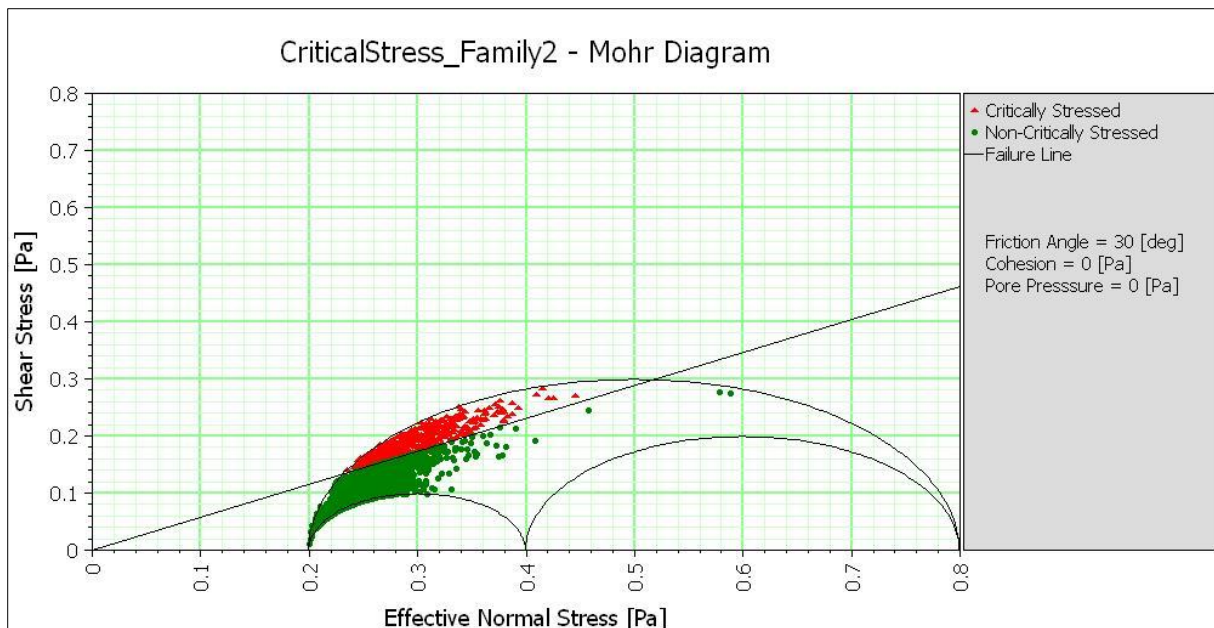


Figure 10. 1. Mohr diagram of Family 2.

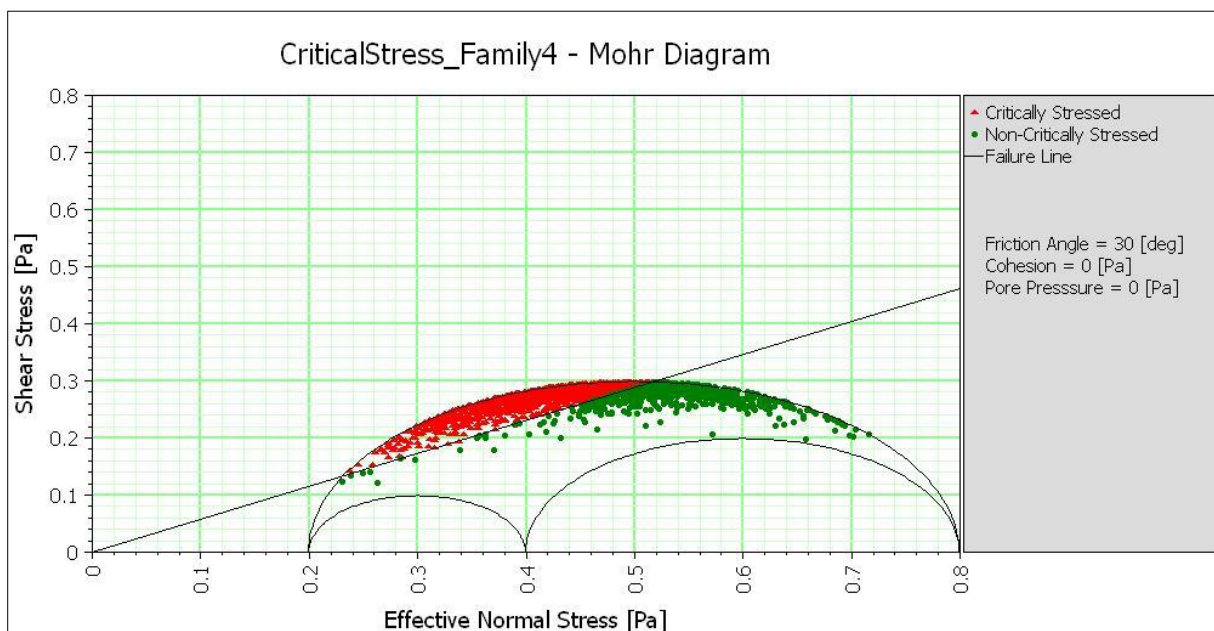


Figure 10. 2. Mohr diagram of Family 4.

Figures 10.3 and 10.4 show in 3D-view Critically Stressed Fractures.

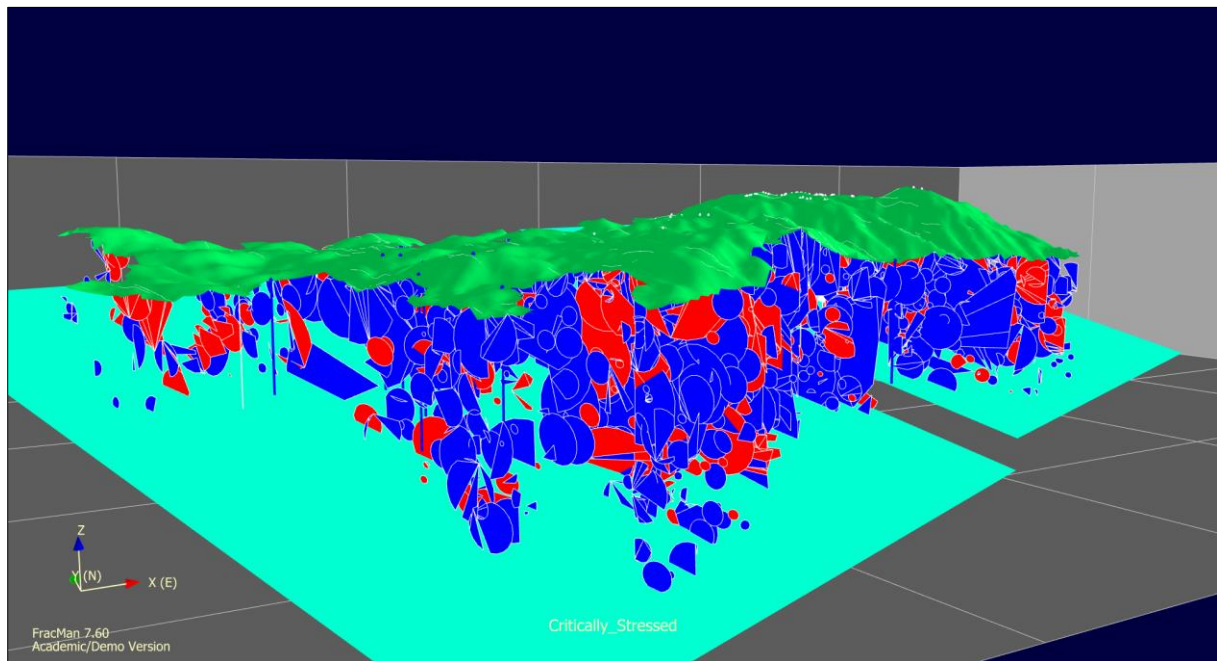


Figure 10. 3. Critically stressed fractures in red of Family 2.

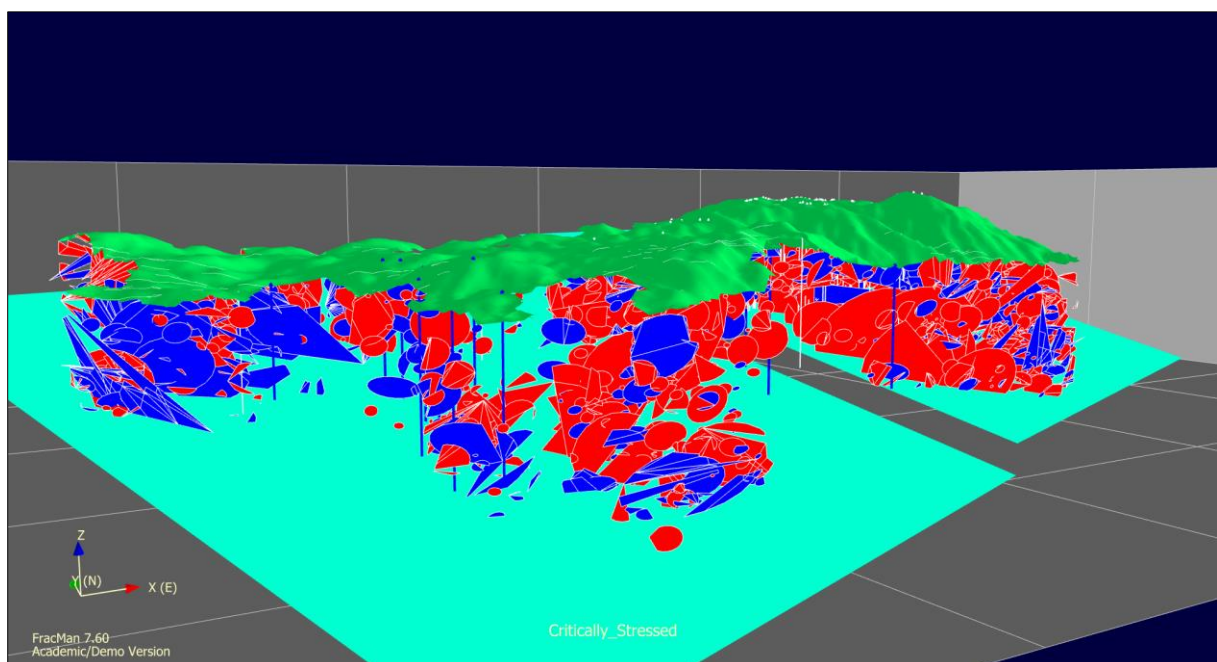


Figure 10. 4. Critically stressed fractures in red of Family 4.

From the analysis carried out we deduce that families 2 and 4 are put under critical stress, this implies a possible opening of stressed fractures that the karst could use for its development. With reference to the Liñan study it does not appear that the family 5 keeps stressed fractures. From figure 9.6.b the family 5 is influential for the possible passage of water in the karst aquifer.

11. Conclusions

The work carried out for this project was implemented to analyse and improve a methodology that qualitatively establishes tectonic influence in the development of the karst through the creation of a 3D Discrete Fracture Network Model.

This method has been divided into two parts: realization of the 3D Discrete Fracture Model and finally its validation from both the statistical and hydrogeological point (3D Discrete Fracture Network Model) of the karst area of Sierra de las Nieves.

The methodology used for the realization of the model was composed using substantially superficial discontinuity information (faults, joints, fractures and foliations). Their study was carried out through spatial, directional, intensity, orientation and length analyses. To obtain these analyses, it was necessary to realize a bibliographic research of some three-dimensional information (orientation and inclination of fractures, etc.) of the study area.

The process used is satisfactory for the complex structure of a karst, in which, in addition to the clear influence of tectonics and therefore fracturing, the flow of underground water is also conditioned by other factors, such as stratification and geological structure, which in this work were not taken into consideration.

Another factor that influenced the creation of the model was, without a doubt, the origin of the discontinuity information used. For the realization of the map of discontinuity (Figure 3.9), different geological maps and lineaments maps have been adopted by various researchers over the last 50 years. As often happens in the research work the information and data are not sufficient for an in-depth analysis, while in the case of this thesis the data of superficial discontinuities were more than adequate, the problem however was the discrepancy of this information. The maps used refer to different authors from the '70s to today, and as is clear, the differences in the type of work done by different groups of geologists and researchers have been substantially an important factor that has affected the results obtained by the 3D Discrete Fracture Network Model. An obvious example is the geological map MAGNA50 (Figure 3.4.a): the area of the Sierra de las Nieves is part of two geological sheets made by two different research groups, made in different years, 1972 and 1981, which produced a map in the discontinuity analysis (Figure 3.4.b) with a clear division of behaviour between the southern and northern zone of the study area.

For this reason, it would have been useful to realize some exits and measurements in situ with a group of scientific experts to verify and expand the information used.

The last part of the work, which includes the analysis of Fracture Clusters, Pathway Analysis and Critical Stress Analysis, was surprisingly good compared to previous studies related to the Sierra de las Nieves karst, in particular the studies of Liñan (2005) and Pedrera (2015).

Therefore, the results obtained show how the presence of the Turquillas fault affects both the formation of clusters and the directionality of the flow of water. Most of the conduits created by the model have a preferential direction from the Pico di Torrecilla towards SE, where there are the largest springs in the park. Another outcome consistent with the influence of fracturing with the development of the karst is to demonstrate, through the Pathway and Critical Stress analysis, that the evolution of the karst appears to favour some families of fractures, NS, NEE-SWW and NNW-SSE, rather than the others.

The model turns out to have some behaviours that are dissociated from the real composition of the karst of Sierra de la Nieves. This factor is probably due, as explained above, by the type of accuracy of the data entered in the model and the lack of data diversity.

The realization of this model can be taken as a starting point for the creation of something more complex taking into consideration caving speleological studies, geophysical analyses and hydrogeological studies in order to improve the representation and geological behaviour of fractures and conduits according to the exit flow from the karst springs.

The proposed study addresses key aspects for the socio-economic development of countries that have to cope with necessities related to the management of water resources. This work examines, according to the relationship between the Karst spatial arrangement and the tectonic system, the spatial position of a number of water resources that can directly or indirectly influence the quality of life of a population, for example the Río Verde, Zarzalones and Río Genal springs. This indirect form of study translates into a better understanding of the great complexity of karst systems.

References

- Alghalandis, Y.F. 2017. *ADFNE: Open source software for discrete fracture network engineering, two and three dimensional applications*. Computers & Geosciences 102: 1-11.
- Ballesteros, D.; Jiménez-Sánchez, M.; García-Sansegundo, J.; Borreguero, M. 2014. *SpeleoDisc: A 3-D quantitative approach to define the structural control of endokarst. An application to deep cave system from the Picos de Europa, Spain*. Geomorphology 216: 141-156.
- Bologa, S.M.; Glaze, L.S.; Bruno, B.C. 2007. *Nearest-neighbor analysis of small features on Mars: Applications to tumuli and rootless cones*. Journal of Geophysical Research 112: 1-17.
- Borradaile, G. 2003. *Statistic of Earth Science Data. Their Distribution in Time, Space and Orientation*. Springer-Verlag Berlin Heidelberg New York.
- Chen-Chang, L.; Cheng-Haw, L.; Hsin-Fu, Y.; Hung-I, L. 2010. *Modeling spatial fracture intensity as a control on flow in fractured rock*. Springer-Verlag. Environ Earth Sci.
- Clark, P.J.; Evans F.C. 1954. Distance to Nearest Neighbor as a Measure of Spatial Relationship in Populations. Ecology, Vol. 35, Issue 4: 445-453.
- Cristina Liñán Baena, 2005. *Hidrogeología de acuíferos carbonatados en la unidad Yunquera-Nieves (Málaga)*. Instituto Geológico y Minero de España.
- Dershowitz, W.S.; Fidelibus, C. 1999. *Derivation of equivalent pipe network analogues for three-dimensional discrete fracture networks by the boundary element method*. Water Resources Research, Vol. 35, No 9: 2685-2691.
- Durán Valsero, J.J. 1996. *Los sistemas kársticos de la provincia de Málaga y su evolución: contribución al conocimiento paleoclimático del cuaternario en el Mediterráneo Occidental*. PhD Thesis. Madrid, Universidad Autónoma de Madrid.
- Elmo, D.; Stead, D. 2010. *An Integrated Numerical Modelling–Discrete Fracture Network Approach Applied to the Characterisation of Rock Mass Strength of Naturally Fractured Pillars*. Rock Mech Rock Eng 43: 3-19.
- Ford, D.; Williams, P. 2007. *Karst Hydrogeology and Geomorphology*. John Wiley & Sons, Ltd.
- Genthon, P.; Maurizot, P.; Vende-Leclerc, M.; Iseppi, M. 2016. *Morphology and distribution of dolines on ultramafic rocks from airborne LIDAR data: the case of southern Grande Terre in New Caledonia (SW Pacific)*. ResearchGate 41 (13).
- Guardiola-Albert, C.; Martos-Rosillo, S.; Pardo-Igúzquiza, E.; Durán, J.J.; Pedrera, A.; Jiménez-Gavilán, P.; Liñán Baena, C. 2015. *Comparison of Recharge Estimation Methods During a Wet Period in a Karst Aquifer*. Groundwater vol.53, No. 6: 885-895.
- Gutiérrez Elorza, M. 2008. *Geomorfología*. Prentice Hall. Pearson Educación, S.A.
- Hammer, Ø. 2009. New statistical methods for detecting point alignments. Computers & Geosciences 35: 659-666.
- Juan José Durán Valsero, 1996. PhD thesis, *Los sistemas Kársticos de la provincia de Málaga y su evolución: contribución al conocimiento paleoclimático del cuaternario en el mediterráneo occidental*, Universidad Autónoma de Madrid.
- Judson Wynne, J.; Titus, Timothy N.; Chong Diaz, G. 2008. *On developing thermal cave detection techniques for earth, the moon and mars*. Earth and Planetary Science Letters 272: 240-250.
- Lutz, T.M. 1986. An analysis of the orientations of large-scale structures: a statistical approach based on areal distributions of pointlike features. Journal of Geophysical Research 91: 421-434.

- Lutz, T.M.; Gutmann, J.T. 1995. *An improved method for determining and characterizing alignments of pointlike features and its implications for the Pinacate volcanic field, Sonora, Mexico*. Journal of Geophysical Research 100: 659-670.
- Martín-Algarra, A.; Mazzoli, S.; Perrone, V.; Rodríguez-Cañero, R.; Navas-Parejo, P. 2009. *Variscan Tectonics in the Malaguide Complex (Betic Cordillera, Southern Spain): Stratigraphic and Structural Alpine versus Pre-Alpine Constraints from the Ardales Area (Province of Malaga). I. Stratigraphy*. The Journal of Geology 117: 241-262.
- Martín-Algarra, A.; Mazzoli, S.; Perrone, V.; Rodríguez-Cañero, R. 2009. *Variscan Tectonics in the Malaguide Complex (Betic Cordillera, Southern Spain): Stratigraphic and Structural Alpine versus Pre-Alpine Constraints from the Ardales Area (Province of Malaga). II. Structure*. The Journal of Geology 117: 263-284.
- Muñoz-Martín, A.; De Vicente, G. 2006. *Análisis del estado de esfuerzos en la corteza*. ResearchGate.
- Pandolfi, O.; Berlinghieri, M.; Oreste, P. *Utilizzo della fotogrammetria digitale tridimensionale per lo studio della stabilità delle cave di marmo nelle Alpi Apuane*.
- Pardo-Igúzquiza, E.; Durán, J.J.; Robledo-Ardila, P.; Luque-Espinar, J.A.; Martos-Rosillo, S.; Guardiola-Albert, C.; Pedrera, A. 2016. *The karst network system of the Sierra de las Nieves (Málaga, Spain). An example of a high relief Mediterranean Karst*. Boletín Geológico y Minero 127 (1): 193-204.
- Pardo-Igúzquiza, E.; Durán, J.J.; Robledo-Ardila, P.; Luque-Espinar, J.A.; Martos-Rosillo, S. 2014. *Analysis of karst terrains using the digital elevation model. Application to the Sierra de las Nieves (province of Málaga)*. Boletín Geológico y Minero 125 (3): 381-389.
- Pedrera, A.; Luque-Espinar, J.A.; Martos-Rosillo, S.; Pardo-Igúzquiza, E.; Durán-Valsero, J.J.; Martínez-Moreno, F.; Guardiola-Albert, C. 2015. *Structural control on karstic conduits in a collisional orogen (Sierra de las Nieves, Betic Cordillera, S Spain)*. Geomorphology 238: 15-26.
- Pulido Bosch, A. 2014. *Principios de hidrogeología kárstica*. Universidad de Almeria. Editorial Universidad de Almeria.
- Radulovic, M. 2013. *A new view on karst genesis. Carbonates and Evaporites*.
- Tinkler, K.J. 1971. *Statistical Analysis of Tectonic Patterns in Areal Volcanism: The Bunyaruguru Volcaic Field in West Uganda*. Mathematical Geology, Vol. 3, No 4: 335-355.
- <http://pnoa.ign.es/ortofotos> (saw 30/06/2018)
- <http://info.igme.es/cartografiadigital/geologica/Magna50.aspx> (saw 30/06/2018)